Design and preparation of influenza vaccines using gold nanoparticles

Taiyu Tazaki

Doctor of Science

Hokkaido University

2019

Contents

Chapter 1

General Introduction

1-1 Nanoscale medical science

1-1-1 Nanomedicine

Nanotechnology have referred to a technology to manipulate substances on a nanometer scale. Especially, the application of nanotechnology for medicines such as therapeutics, diagnosis, imaging and tissue engineering have been referred to as “nanomedicine”. Up to now, various particle-based nanomedicines have been studied including liposomes, polymeric particles, virus-like particles and metal particles (Figure 1-1).[12]

Liposomes have been most studied and are highly practical materials as drug delivery agents. Liposomes were proposed in the 1960’s and the most studied nanoparticle-based nanomedicine.[3–5] Liposome is a capsule formed by assemble of phospholipids and has high biocompatibility. Although liposomes are easily trapped by reticuloendothelial systems, have been practically used through overcoming such problem by surface modification of liposomes such as PEGylation.[6] In the 1970s, the controlled release system using polymer was reported.[7,8] So far, majority of drug delivery products approved by Food Drug Administration (FDA) are composed of liposomes and polymers.

On the other hand, inorganic nanoparticles have unique benefits and have been applied not only drug delivery,[9] but also diagnostics and phototherapies.[10,11] Superparamagnetic iron oxide nanoparticles are useful as magnetic resonance imaging contrast agents[12,13] and magnetic targeting.[14,15] Novel metal nanoparticles have unique optical features such as localized surface plasmon resonance (LSPR)[16] and have been used for sensor and hyperthermia.[17–19] Especially, gold nanoparticles (AuNPs) can be easily controlled their size, shape and surface chemical properties, so that are applied for drug delivery carrier, vaccine scaffolds and other nanomedicines.

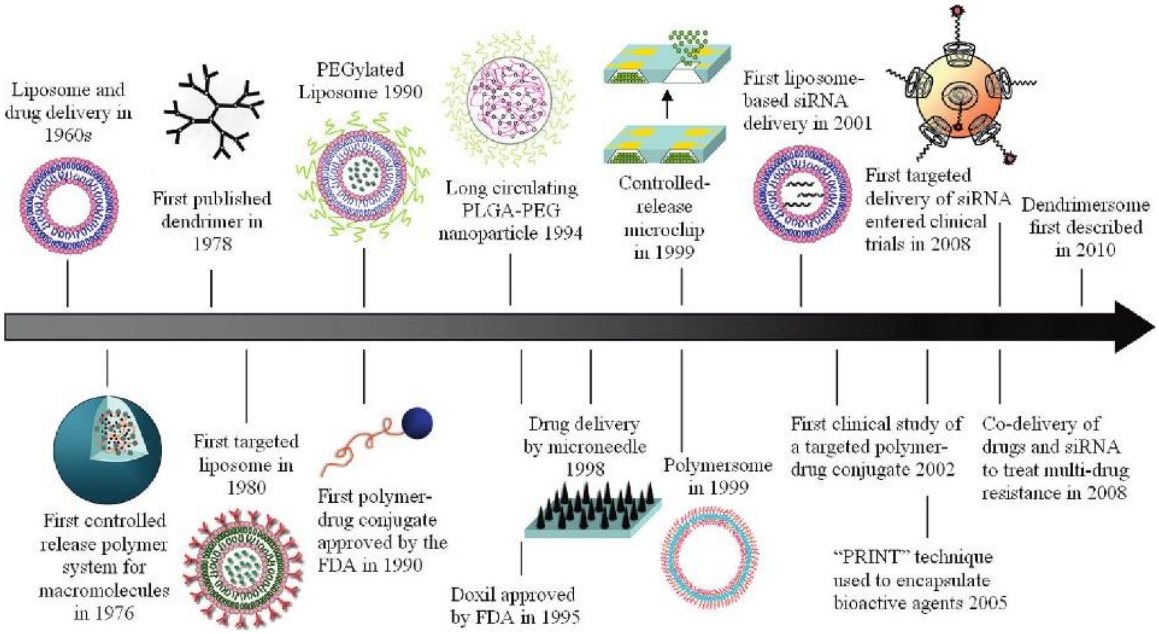

Figure 1-1 Historical timeline of nanotechnology-based drug delivery.[2]

1-1-2 Gold nanoparticles in nanomedicine

Historically, gold colloidal particles are found from fifth and fourth centuries B.C. in China, Arabia and India. In middle age in Europe, colloidal gold had been studied by alchemists. Paracelsus regarded colloidal gold obtained by reduction of auric chloride as therapeutic agent for mental disorder and syphilis. In twentieth century, using colloidal gold was proposed for treatment of cancer.

Today, various synthetic methods of AuNPs have been proposed. AuNPs are synthesized by the reduction of Au ion in the presence of capping agents. J. Turkevich reported synthetic method of spherical gold nanoparticles (Turkevich method) by using citric acid as reducing agent in 1951.[20,21] M. Brust and D. J. Schmitt reported the method of gold nanoparticle synthesis (Brust-Schmitt method) into the organic solvent. They use alkanethiol, sodium borohydride and tetraoctylammonium bromide as a surface capping agent, reductant agent and phase-transfer reagent, respectively.[22,23] Gold nanoparticles are easily synthesized to various size and shape. (Figure 1-2) The size of gold nanoparticles can be controlled by synthesis conditions such as seed or gold amount. N. G. Bastús reported the synthetic method of monodispersed citrate-stabilized gold nanoparticles in the range of 8-180 nm.[24] The shape of gold nanoparticles can be controlled by silver ion, halide ions and the concentration of capping agent.[25,26] J. Murphy initially reported shape-controlled gold nanoparticle synthesis using surfactant template in 2001.[27] This led to a vast synthetic method of various shaped gold nanoparticles including rod,[28–33] cube,[34] plates[35–37] , octahedra[38,39] and more complex structures.[40,41] The surface of gold nanoparticles is easily modified with various compound by gold-thiol binding and layer-by-layer methods and this surface modification affects gold nanoparticle physicochemical properties.[42] Especially, formation of self-assembled monolayers of thiol molecules on the gold nanoparticle surface has been common technique (Figure 1-3).[43–45] Gold nanoparticles are chemically stable than other metal nanoparticles. Therefore, gold ions not released so much even in an acidic

environment while other metal nanoparticles such as silver, CdSe/ZnS and Fe_3O_4 nanoparticles release much amount of metal ions in acidic condition.[46]

To date, various application of gold nanoparticles for medicine have been established (Figure 1-4).[47,48] Gold nanoparticles have unique optical properties originated from LSPR. This feature has been used for diagnostics such as immunoassay[49,50] and biosensors[51,52]. Further, since it is easy to control physicochemical properties, AuNPs are suitable for investigating the influence of nanomaterial physicochemical properties on medical potency.

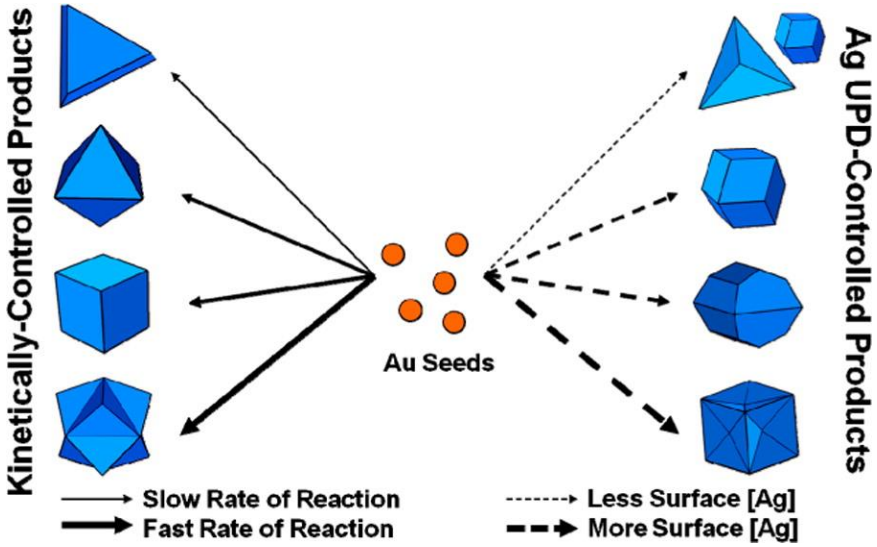

Figure 1-2 versatile strategies to synthesis various shaped AuNPs.[25]

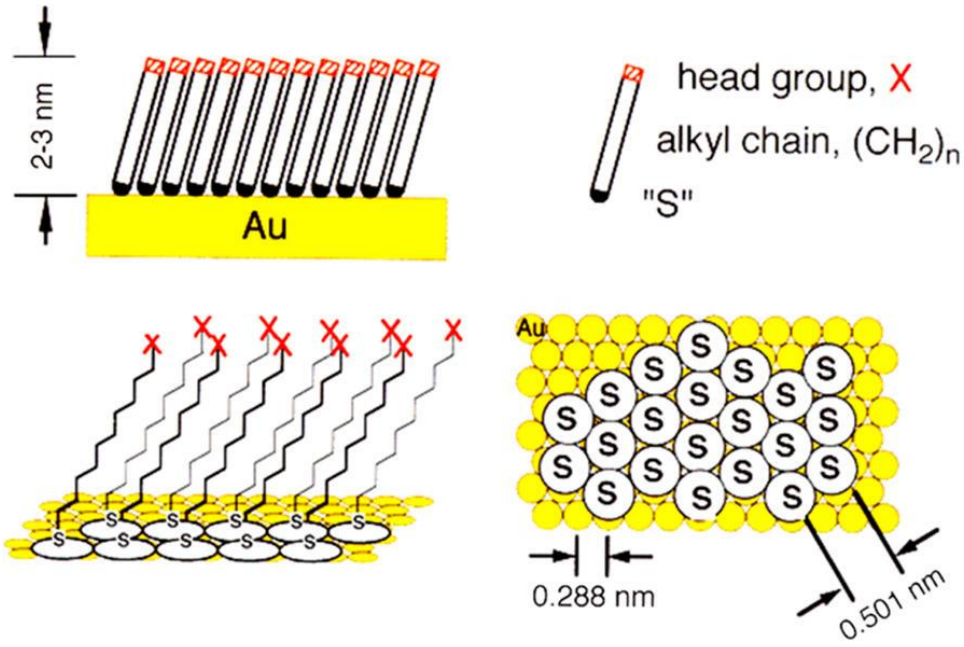

Figure 1-3 formation of self-assembled monolayer of thiolate compounds on gold surface.[43,48]

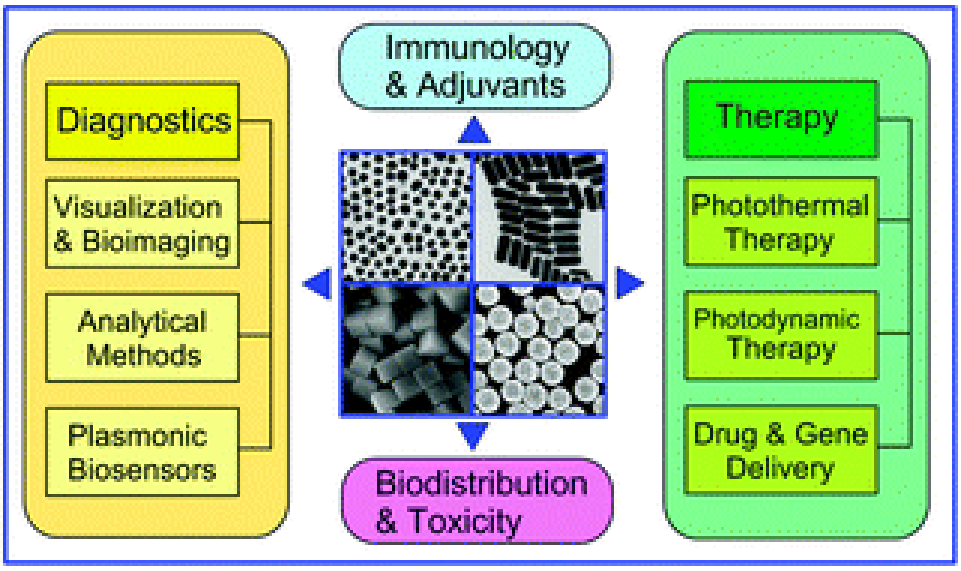

Figure 1-4 Application of various shaped AuNPs for nanomedicine.[47]

1-1-3 Effect of nanoparticle physicochemical properties on interaction between nanoparticle and biological milieu

The gold nanoparticles can be synthesized into various size and shape. Furthermore, the chemical properties of gold nanoparticle surface can be controlled by gold-thiol bond utilizing molecular functionalization. These physicochemical properties can affect interaction between gold nanoparticles and biological milieu.

The nanoparticle uptake is affected by nanoparticle size, shape, surface electric charge and surface chemical composition. W. C. W. Chan reported that 50 nm in diameter of gold nanoparticles have higher cellular uptake efficient in the range of 14–100 nm in diameter (Figure 1-5A).[53] In term of shape, complicated results were reported. It was reported that the cellular uptake efficiency of spherical gold nanoparticles is higher than that of rod-shaped gold nanoparticles (Figure 1-5B).[53–55] W. C. W. Chan speculated that the higher curvature of rod-shaped gold nanoparticles can have larger contact area with cellular membrane receptors. As a result, available receptors per rod-shaped gold nanoparticle and cellular uptake could reduce. On the other hand, higher aspect ratio micro particles[56] and protein coated rod-shaped gold nanoparticles[57] were internalized in cell at a higher rate compared to spherical particles (Figure 1-5C). The theoretical literature reported different results that spherical nanoparticle[58] or rod-shaped nanoparticle[59] had fastest internalized rate. These reports imply that the shape of nanoparticles affects cellular uptake efficient, but do not unambiguously determined. Nanoparticle shape also affects skin penetration. R. Fernades reported rod-shaped gold nanoparticles efficiently internalized in human and mouse skin than spherical gold nanoparticles.[60] Surface charge of nanoparticles also affects uptake efficiency.[61] Generally, positively charged nanoparticles efficiently internalized into cells. This have been thought due to negative cell membrane charge. Utilizing this property, nanoparticles are modified with cationic cell penetrating peptides (CPP) to enhance cellular uptake.[62,63]

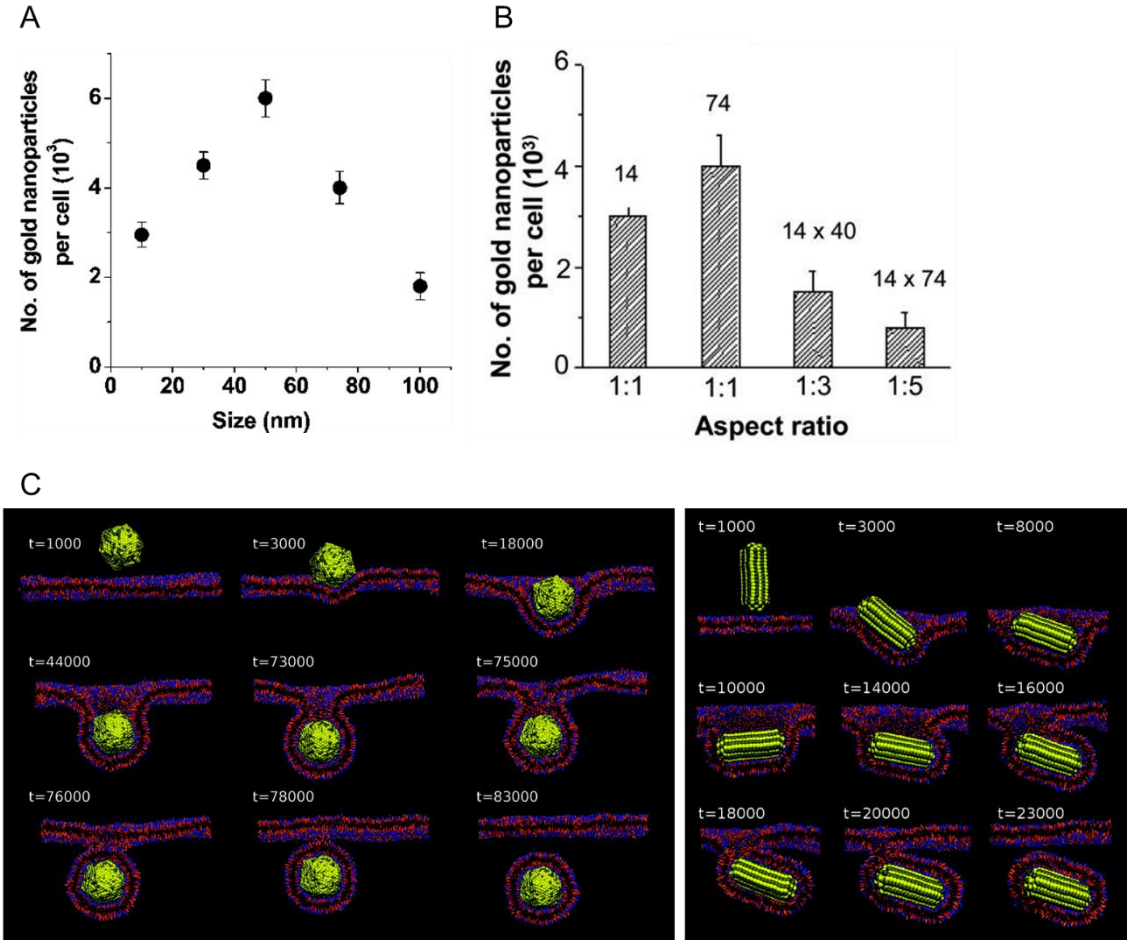

Figure 1-5 the effect of nanoparticle geometry on cellular uptake efficiency. (A) size-dependent cellular uptake efficiency of nanoparticles.[53] (B) effect of nanoparticle shape on cellular uptake efficiency.[53] (C) MD simulation of passive uptake of different shaped nanoparticles.[59]

These nanoparticle geometry and surface properties also affect nanoparticle biodistribution (Figure 1-6).[64–66] Nanoparticle size affects clearance from bloodstream by reticulo-endothelial system organs such as liver, kidney and spleen. Smaller nanoparticle (less than 5 nm) are cleared through renal glomeruli pore. Larger nanoparticle than 100 nm are filtered by spleen and trapped by liver. Therefore, nanoparticles, which have the size of 5 to 100 nm, are regarded to have longer circulation times.[67] The circulation of nanoparticles is also affected by nanoparticle shape.[67–69] K. C. L. Black *et al.* demonstrated the different *in vivo* distribution of four kind shaped AuNPs (sphere, disk, rod and cage). They found spherical AuNP showed good blood circulation and higher tumor uptake (Figure 1-7).[69] The effect of nanoparticle surface charge on distribution have been also investigated. S. G Elci *et al*. reported that positively charged AuNPs concentrated in the glomeruli and liver hepatocytes, whereas the neutral and negatively charged AuNPs did not and negatively charged AuNPs are cleared slowly than positively charged AuNPs. Neutral AuNPs tend to interact with immune systems evidenced by greater accumulation in marginal zone and white pulp in spleen and the Kupffer cells (Figure 1-8).[70] Surface chemistry of nanoparticle also influences interaction between nanoparticle and biological milieu and subsequent biodistribution. Typically, modification of nanoparticles with polyethylene glycol or zwitterionic compound gives stealth effect *in vivo* and longer circulation time by suppressing opsonization and formation of protein coronas.[65,71,72]

The nanoparticle behavior in biological milieu depends on their physicochemical properties. Therefore, it is essential to control nanoparticle physicochemical properties to apply for nanomedicine.

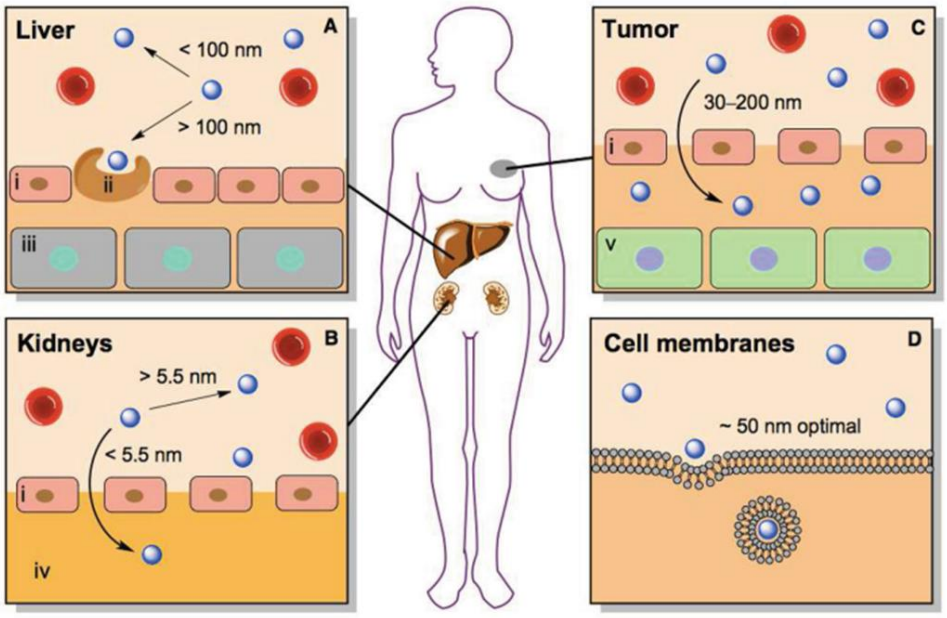

(i) endothelial cell; (ii) Kupffer cell; (iii) hepatocyte;
(iv) glomerular basement membrane; (v) tumor cell.

Figure 1-6 Size-dependent biodistribution of blood-circulating nanoparticles. (A) removal of larger nanoparticles by Kupffer cells in liver. (B) excretion of smaller nanoparticles through glomerular filtration in kidney. (C) passive accumulation of nanoparticle to the tumor cells. (D) internalization of nanoparticles into cells.[71]

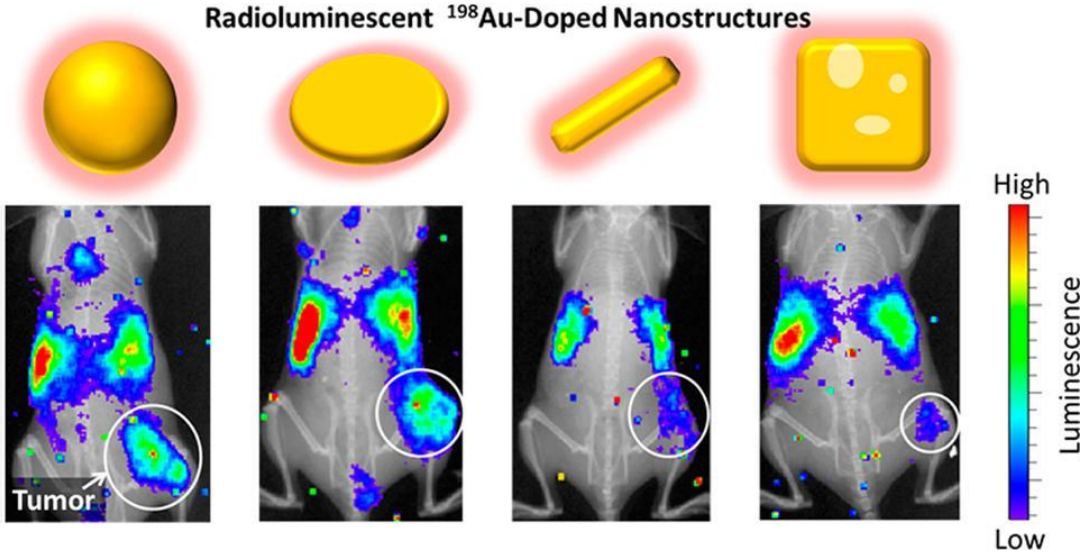

Figure 1-7 Shape-dependent biodistribution and tumor uptake of PEGylated AuNPs. Spherical AuNPs showed good circulation time and tumor accumulation.[69]

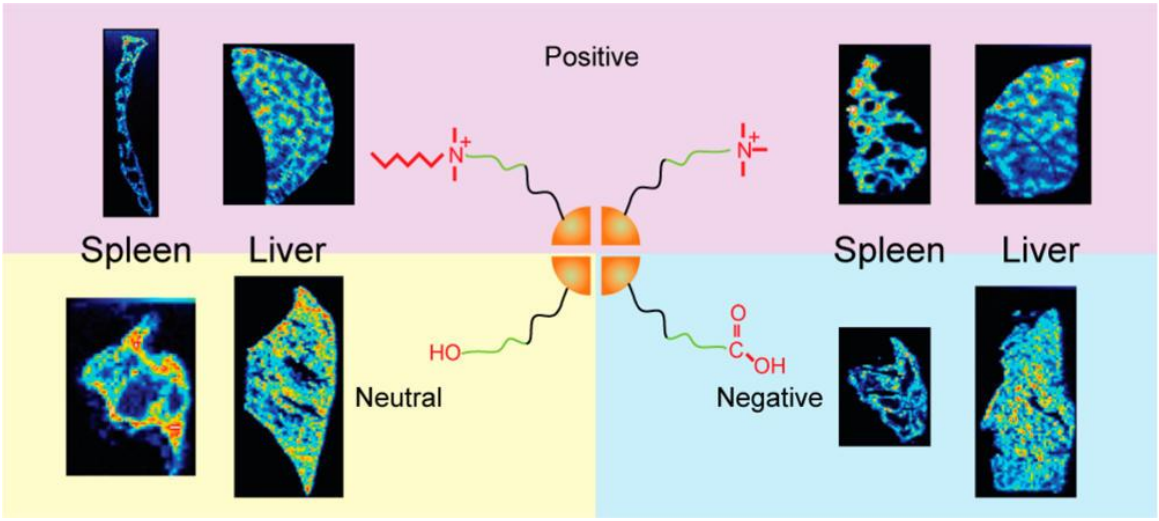

Figure 1-8 Effect of nanoparticle surface charge and chemical properties on suborgan biodistribution.[70]

1-2 Nanoparticle-based vaccine

1-2-1 Infectious disease and influenza virus

Infectious diseases are disorder caused by pathogenic microorganisms such as viruses, bacteria, parasites and fungi. The history of infectious disease has been long. It is considered that smallpox has existed since 1300 BC. Infectious diseases still have remained in a major cause of death worldwide. In the report by World Health Organization, lower respiratory infection was most deadly infectious disease causing 3.0 million deaths worldwide in 2016.

Influenza viruses are classified to the Orthomyxoviridae and have single-stranded RNA genome (Figure 1-9A). There are four types of viruses, influenza A, B, C and D based on antigenicity of nucleoprotein and matrix protein. Influenza virus A is further classified based on antigenicity of hemagglutinin and neuraminidase. Influenza virus A infects mammals and Aves (Figure 1-9B). Influenza viruses infect host cells in upper respiratory tract by recognition of cell surface sialic acids by hemagglutinins. After proliferation in the host cells, influenza viruses are released from cell surface by degradation of sialic acids by neuraminidase (Figure 1-9C). Influenza viruses avoids host immunity by antigenic drift. Thus, annual update of influenza vaccines has been required. Moreover, major changes in antigen, antigenic shift, has been rarely occurred by reassortment of the influenza virus A genomes (Figure 1-9D).[73] Therefore, development of universal influenza vaccines which protect against various strain and newly emerging influenza strains as well as have safety and induce long-term immunity have been required.[74,75]

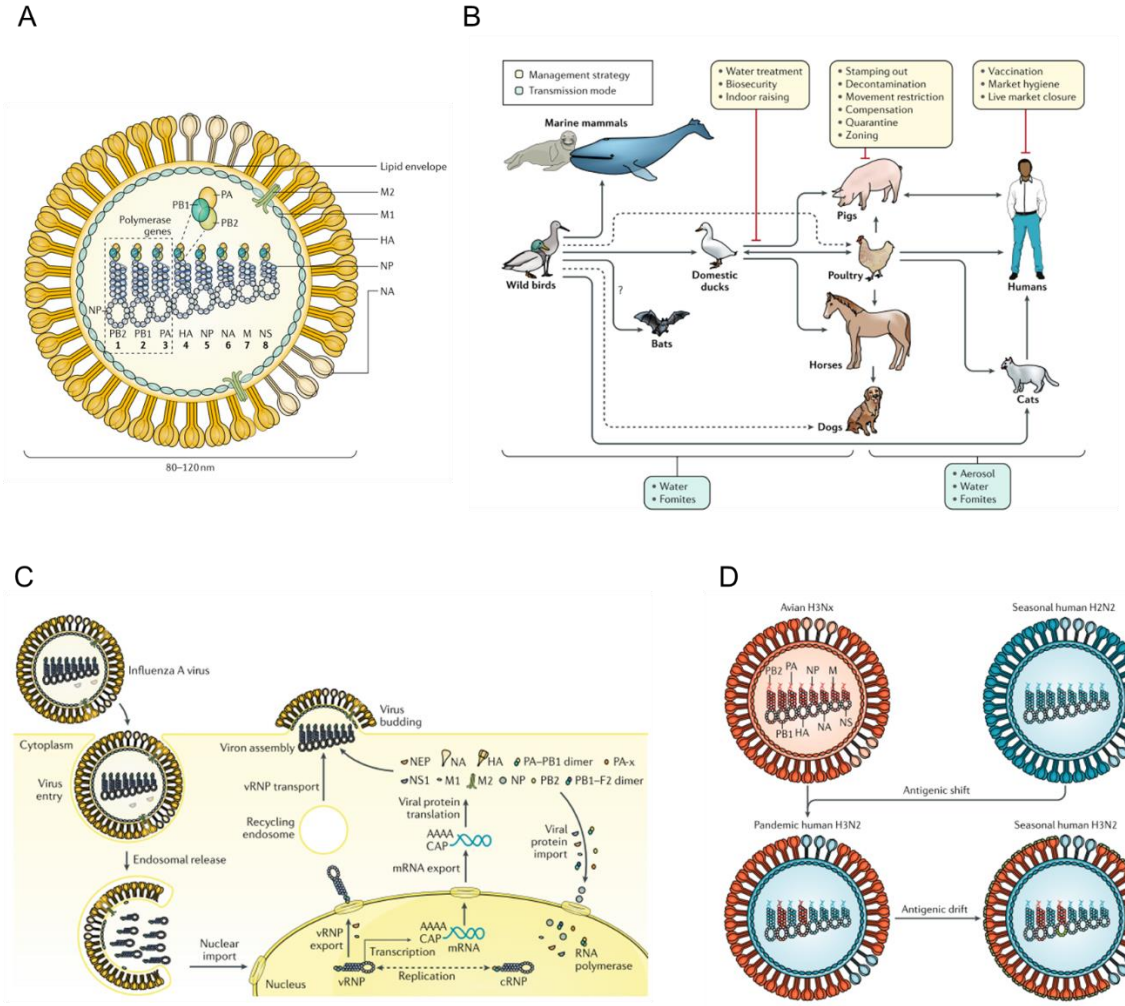

Figure 1-8 (A) typical structural image of influenza virus. (B) emergence of influenza virus from bird host. (C) life cycle of influenza virus in cell. (D) schematic illustration of influenza antigenic shift and antigenic drift.[70]

1-2-2 Vaccine development

The first counterpart against infectious diseases was smallpox vaccine using cowpox developed in 1796 by Edward Jenner. Nowadays, several types of vaccines have been developed. Live attenuated vaccine uses weakened whole viruses by cold-adaptation or proliferation in cultured cells. Live attenuated vaccines elicit strong and long-lasting immune responses including cellular immunity and humoral immunity by just once immunization. However, because live-attenuated vaccines contain living virus which have infectivity, they have risks of infection and side reactions to children and the elderly. Inactivated vaccines use split virus components obtained by ether treatments. Subunit vaccines contain only antigenic parts. Inactivate vaccine and subunit vaccine do not have live component, so that are considered as more safety vaccine. Because inactivated vaccines and subunit vaccines have lower immunogenicity, these vaccines need multiple immunization or addition of immunostimulator called as adjuvant.

Currently, various influenza vaccines are applied. Inactivated influenza vaccine is standard and immunized subcutaneously or intramuscularly. These administration methods elicit mainly IgG antibody responses. On the contrast, intranasal immunization of influenza vaccine can induce a mucosal IgA antibody response in the upper respiratory tract, promoting protection from influenza virus infection.[75] Elicited IgA antibody have potential to protect against different strain in same subtypes.[76] Live attenuated intranasal influenza vaccines have been approved for clinical use only to limited age groups due to risk of side reaction. Inactivated intranasal influenza vaccines do not have sufficient activity, so that require adjuvants. Cross protection against different subtype influenza viruses and newly emerging viruses has been also required. The hemagglutinin stem domain, which has been highly conserved than head domain of hemagglutinin, is a main candidate antigen towards broadly protective influenza vaccines.[77–82]

1-2-3 Use of adjuvant for vaccine

Adjuvant has originated in the Latin “adjuvare” and administrated with antigen to enhance immunogenicity of vaccines. In the 1920’s, A. T. Glenny discovered that aluminum salts enhance vaccine potency of diphtheria toxoid.[83] From this, adjuvants have been received much attention and actively studied. Currently, various adjuvants are known such as nucleic acids and their analogues[84–87], alum[88,89], emulsions[90], liposomes[91] and constitutes of bacteria[92,93]. Action mechanisms of adjuvants had been unclear while it had been thought that adjuvants worked through promotion of antigen uptake to immune cells and prevention of antigen degradation. Recently, Jules A. Hoffmann, Bruce A. Beutler and Ralph M. Steinman, who got novel prize, and other researchers revealed the action mechanisms of adjuvant. Today, it is widely known that adjuvants activate antigen presenting cells such as dendritic cells through pattern recognition receptors (PRRs) recognition of adjuvants and endogenous PRR ligands induced by adjuvants.

Alum is aluminum salts and a one of typical adjuvant. Alum causes cell death and subsequent DNA release of host cell and released DNA acts as endogenous immunostimulator.[89] The adjuvanticity of Alum can be tuned by fining shape of Alum particles.[88] Exogeneous nucleic acids also work as adjuvant.[86] Unmethylated CpG DNA double-stranded RNA analogues such as poly(I:C) stimulate toll-like receptor (TLR) 9 and 3, respectively.

Nowadays, adjuvants have been essential for the development of effective vaccines.

1-2-4 Use of nanoparticles for vaccines

Nanoparticles are good candidate for scaffold of vaccines. The immobilization of antigen onto gold nanoparticles and enhancement of immunogenicity was initially reported in the 1980s.[94] To date, various nanoparticles such as liposomes, emulsion, micelles, virus-like particles and metal nanoparticles have been applied to vaccines and immunotherapies.[95] These nanoparticles have benefits to improve antigen delivery, stimulation of innate immunity and antigen recognition by B cell receptor (Figure 1-10).

Self-assembled influenza hemagglutinin ferritin-presenting nanoparticles improved vaccine potency and induced broadly neutralizing antibody against H1N1 influenza viruses.[96] Regarding the targeting of the nasal cavity, antigen delivery using nanogels[97] and polymer nanoparticles[98] has been shown to be effective. Conjugation of adjuvant onto nanoparticles and subsequent application have been also demonstrated. Radovic-Moreno *et al*. reported that the conjugation of CpG oligonucleotides onto AuNPs enabled the adjuvant dose to be decreased while enhancing vaccine potency in systemically immunized mice.[99] Zhang *et al*. reported an enhanced antigen-specific T cell response in mice intradermally immunized with multilayered co-assemblies of antigen and poly(I:C) on AuNPs.[100]

Nanoparticles themselves have immunogenicity and it depends on physicochemical properties of nanoparticles. Nanoparticle size affects inflammatory responses in vitro. T. Kusaka reported that 30-1000 nm diameter silica particles induced interleukin-1β production (Figure 1-11A).[101] Nanoparticle shape and surface charge also affects inflammatory responses. Higher aspect ratio particles[88,102,103] and positively charged nanoparticles[104] induce interleukin-1β production *via* lysosome destabilization and subsequent NLRP3 inflammasome activation (Figure 1-11B, C).

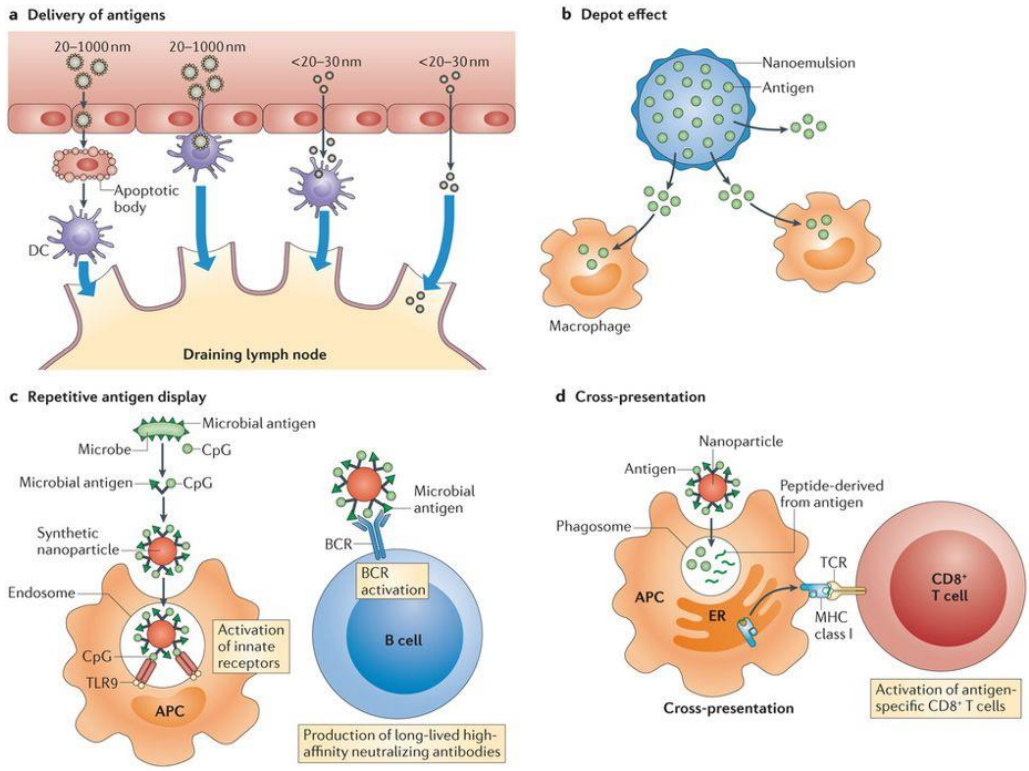

Figure 1-10 Application of nanoparticles and its various benefits.[95]

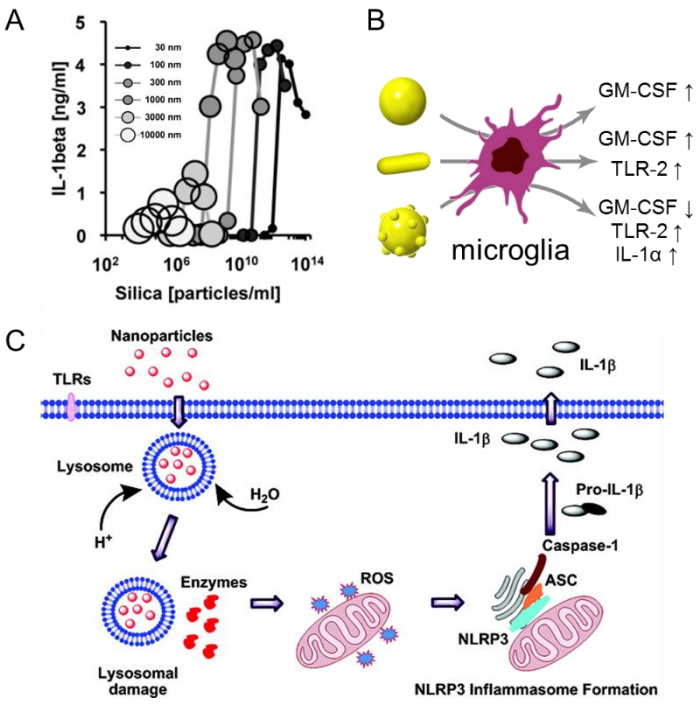

Figure 1-11 The effect of nanoparticle size (A)[101] and shape (B)[102] on innate immune responses.
(C) The mechanism of IL-1β secretion by stimulation with amino-functionalized nanoparticles.[104]

Physical properties such as size and shape of nanoparticle scaffolds affect vaccine potency.[105–108] Plebanski *et al*. reported that the size of the antigen carrier influenced the immune response pathway in vivo after intradermal immunization.[105] They reported that 40-50 nm nanoparticles enhanced cellular immunity responses and 90-125 nm nanoparticles enhanced humoral immunity responses. Niikura *et al*. reported the effect of nanoparticle shape on vaccine potency and cytokine production.[107] They found cytokine production from immune cells depended nanoparticle shape and spherical nanoparticle enhanced vaccine potency than rod-shaped nanoparticles as West Nile virus antigen scaffold. Size and shape are important factor to use nanoparticles as adjuvant scaffold. Zhou *et al*. demonstrated that there was an optimal size for AuNPs used as an antigen or adjuvant carrier to enhance cellular immunity both in vitro and in vivo.[109] Y. Liu *et al*. reported shape dependent adjuvanticity of polyvinylpyrrolidone and polyethylene glycol modified silver nanoparticles.[110]

As shown above, nanoparticles are useful tool to enhance vaccine potency. Furthermore, desired biological responses can be elicited by controlling nanoparticle size, shape and surface properties.

1-3 Objective

Since AuNPs can easily prepared with controlled size, shape and surface properties, AuNPs have benefits for use in nanomedicine. Especially, AuNPs elicit immunological responses depending on these physicochemical properties, and can induce the desired immune responses, so that AuNPs are expected to increase vaccine potency.

Inactivated and subunit vaccines consists of antigen and/or adjuvant. For the stable vaccine supply and safety assessment, it is necessary to reduce dose of antigens and to reduce the toxicity of adjuvants while remaining vaccine potency. It is also required to broadly protect against specific viruses which have various subtypes. Since antigens and adjuvants are recognized and processed by different processes, it is important to design and prepare appropriate nanoparticle scaffolds. In this study, I targeted on influenza vaccines to improve vaccine potency because there are various problems have been remained such as the development of safe and effective adjuvants for intranasal vaccination and the rational antigen design to protect against various influenza subtypes.

In chapter 2, I aimed to develop the safe and effective adjuvant for intranasal influenza vaccine. I focused on nanoparticle shape to enhance adjuvanticity. Different shaped AuNPs were conjugated with RNA adjuvant and their adjuvanticity was evaluated *in vivo*. The effect of administration route was investigated. Further, inflammatory cytokine response was evaluated to investigate toxicity and side reaction possibility of prepared adjuvants.

In chapter 3, I aimed to develop universal influenza vaccine which can protect against various strains of influenza viruses through induction of stalk domain specific antibody production. I designed stalk domain presenting nanoparticle hemagglutinin-AuNP conjugate to enhance stalk domain recognition by antibody production cells: B cell. I prepared sialic acid mimic peptides functionalized AuNPs to immobilize HA directing stalk domain outside. The immobilization of HA was evaluated by dot blot assay comparing reference sequence peptide functionalized AuNPs.

In chapter 4, I summarize the thesis and afford the significance and prospects.

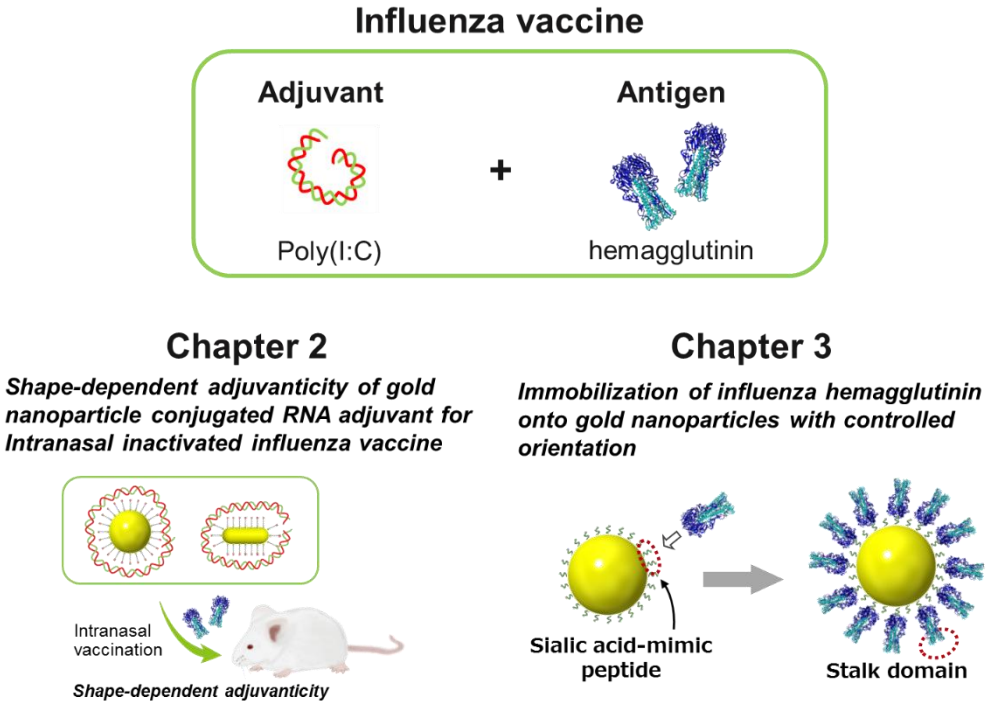

Figure 1-12 Schematic illustration of my doctoral thesis.

1-4 References

(1) Zhang, L.; Gu, F.; Chan, J.; Wang, A.; Langer, R.; Farokhzad, O. Nanoparticles in Medicine: Therapeutic Applications and Developments. *Clin. Pharmacol. Ther.* **2008**, *83* (5), 761–769.

(2) Shi, J.; Votruba, A. R.; Farokhzad, O. C.; Langer, R. Nanotechnology in Drug Delivery and Tissue Engineering: From Discovery to Applications. *Nano Lett.* **2010**, *10* (9), 3223–3230.

(3) Bangham, A. D.; Horne, R. W. Negative Staining of Phospholipids and Their Structural Modification by Surface-Active Agents as Observed in the Electron Microscope. *J. Mol. Biol.* **1964**, *8* (5), 660.

(4) Torchilin, V. P. Recent Advances with Liposomes as Pharmaceutical Carriers. *Nat. Rev. Drug Discov.* **2005**, *4* (2), 145–160.

(5) Allen, T. M.; Cullis, P. R. Liposomal Drug Delivery Systems: From Concept to Clinical Applications. *Adv. Drug Deliv. Rev.* **2013**, *65* (1), 36–48.

(6) Klibanov, A. L.; Maruyama, K.; Torchilin, V. P.; Huang, L. Amphipathic Polyethyleneglycols Effectively Prolong the Circulation Time of Liposomes. *FEBS Lett.* **1990**, *268* (1), 235–237.

(7) Mason, N.; Thies, C.; Cicero, T. J. In Vivo and in Vitro Evaluation of a Microencapsulated Narcotic Antagonist. *J. Pharm. Sci.* **1976**, *65* (6), 847–850.

(8) Freiberg, S.; Zhu, X. X. Polymer Microspheres for Controlled Drug Release. *Int. J. Pharm.* **2004**, *282* (1–2), 1–18.

(9) Xu, Z. P.; Zeng, Q. H.; Lu, G. Q.; Yu, A. B. Inorganic Nanoparticles as Carriers for Efficient Cellular Delivery. *Chem. Eng. Sci.* **2006**, *61* (3), 1027–1040.

(10) Jain, P. K.; Huang, X.; El-sayed, I. H.; El-sayed, M. A. Noble Metals on the Nanoscale : Optical and Photothermal Properties and Some Applications. *Acc. Chem. Res.* **2008**, *41* (12), 7–9.

(11) de Dios, A. S.; Díaz-García, M. E. Multifunctional Nanoparticles: Analytical Prospects. *Anal. Chim. Acta* **2010**, *666* (1–2), 1–22.

(12) Na, H. Bin; Song, I. C.; Hyeon, T. Inorganic Nanoparticles for MRI Contrast Agents. *Adv. Mater.* **2009**, *21* (21), 2133–2148.

(13) Lee, N.; Hyeon, T. Designed Synthesis of Uniformly Sized Iron Oxide Nanoparticles for Efficient Magnetic Resonance Imaging Contrast Agents. *Chem. Soc. Rev.* **2012**, *41* (7), 2575–2589.

(14) Yiu, H. H. P.; Bouffier, L.; Boldrin, P.; Long, J.; Claridge, J. B.; Rosseinsky, M. J. Comprehensive Study of DNA Binding on Iron(II,III) Oxide Nanoparticles with a Positively Charged Polyamine Three-Dimensional Coating. *Langmuir* **2013**, *29* (36), 11354–11365.

(15) Arruebo, M.; Fernández-Pacheco, R.; Ibarra, M. R.; Santamaría, J. Magnetic Nanoparticles for Drug Delivery. *Nano Today* **2007**, *2* (3), 22–32.

(16) Kelly, K. L.; Coronado, E.; Zhao, L. L.; Schatz, G. C. The Optical Properties of Metal Nanoparticles: The Influence of Size, Shape, and Dielectric Environment. *J. Phys. Chem. B* **2003**, *107* (3), 668–677.

(17) Hirsch, L. R.; Stafford, R. J.; Bankson, J. A.; Sershen, S. R.; Rivera, B.; Price, R. E.; Hazle, J. D.; Halas, N. J.; West, J. L. Nanoshell-Mediated near-Infrared Thermal Therapy of Tumors under Magnetic Resonance Guidance. *Proc. Natl. Acad. Sci.* **2003**, *100* (23), 13549–13554.

(18) Huang, X.; El-Sayed, I. H.; Qian, W.; El-Sayed, M. A. Cancer Cell Imaging and Photothermal Therapy in the Near-Infrared Region by Using Gold Nanorods. *J. Am. Chem. Soc.* **2006**, *128* (6), 2115–2120.

(19) Du, J.; Zhu, B.; Chen, X. Urine for Plasmonic Nanoparticle-Based Colorimetric Detection of Mercury Ion. *Small* **2013**, *9* (24), 4104–4111.

(20) Turkevich, J.; Stevenson, P. C.; Hillier, J. A Study of the Nucleation and Growth

Processes in the Synthesis of Colloidal Gold. *Discuss. Faraday Soc.* **1951**, *11* (c), 55.

(21) Wuithschick, M.; Birnbaum, A.; Witte, S.; Sztucki, M.; Vainio, U.; Pinna, N.; Rademann, K.; Emmerling, F.; Kraehnert, R.; Polte, J. Turkevich in New Robes: Key Questions Answered for the Most Common Gold Nanoparticle Synthesis. *ACS Nano* **2015**, *9* (7), 7052–7071.

(22) Brust, M.; Walker, M.; Bethell, D.; Schiffrin, D. J.; Whyman, R. Synthesis of Thiol-Derivatised Gold Nanoparticles In. *J. Chem. Soc. Chem. Commun.* **1994**, No. 7, 801–802.

(23) Perala, S. R. K.; Kumar, S. On the Mechanism of Metal Nanoparticle Synthesis in the Brust–Schiffrin Method. *Langmuir* **2013**, *29* (31), 9863–9873.

(24) Bastús, N. G.; Comenge, J.; Puntes, V. Kinetically Controlled Seeded Growth Synthesis of Citrate - Stabilized Gold Nanoparticles up to 200 Nm : Size Focusing versus . Ostwald Ripening. **2011**, 1–9.

(25) Grzelczak, M.; Pérez-Juste, J.; Mulvaney, P.; Liz-Marzán, L. M. Shape Control in Gold Nanoparticle Synthesis. *Chem. Soc. Rev.* **2008**, *37* (9), 1783–1791.

(26) Langille, M. R.; Personick, M. L.; Zhang, J.; Mirkin, C. A. Defining Rules for the Shape Evolution of Gold Nanoparticles. *J. Am. Chem. Soc.* **2012**, *134* (35), 14542–14554.

(27) Nikhil R. Jana, Latha Gearheart, and C. J. M. Seed-Mediated Growth Approach for Shape- Controlled Synthesis of Spheroidal and Rod-like Gold Nanoparticles Using a Surfactant Template. *Adv. Mater.* **2001**, No. 18, 1389–1393.

(28) Nikoobakht, B.; El-Sayed, M. A. Preparation and Growth Mechanism of Gold Nanorods (NRs) Using Seed-Mediated Growth Method. *Chem. Mater.* **2003**, *15* (10), 1957–1962.

(29) Gole, A.; Murphy, C. J. Seed-Mediated Synthesis of Gold Nanorods : Role of the

Size and Nature of the Seed Seed-Mediated Synthesis of Gold Nanorods : Role of the Size and Nature of the Seed. *Chem. Mater.* **2004**, *16* (21), 3633–3640.

(30) Murphy, C. J.; Sau, T. K.; Gole, A. M.; Orendorff, C. J.; Gao, J.; Gou, L.; Hunyadi, S. E.; Li, T.; April, R. V; Final, I.; et al. Anisotropic Metal Nanoparticles : Synthesis , Assembly , and Optical Applications. **2005**, 13857–13870.

(31) Takenaka, Y.; Kawabata, Y.; Kitahata, H.; Yoshida, M.; Matsuzawa, Y.; Ohzono, T. Effects of Surfactant Concentration on Formation of High-Aspect-Ratio Gold Nanorods. *J. Colloid Interface Sci.* **2013**, *407*, 265–272.

(32) Lohse, S. E.; Murphy, C. J. The Quest for Shape Control: A History of Gold Nanorod Synthesis. *Chem. Mater.* **2013**, *25* (8), 1250–1261.

(33) Su, G.; Yang, C.; Zhu, J. J. Fabrication of Gold Nanorods with Tunable Longitudinal Surface Plasmon Resonance Peaks by Reductive Dopamine. *Langmuir* **2015**, *31* (2), 817–823.

(34) Sau, T. K.; Murphy, C. J. Room Temperature, High-Yield Synthesis of Multiple Shapes of Gold Nanoparticles in Aqueous Solution. *J. Am. Chem. Soc.* **2004**, *126* (28), 8648–8649.

(35) Millstone, J. E.; Park, S.; Shuford, K. L.; Qin, L.; Schatz, G. C.; Mirkin, C. A. Observation of a Quadrupole Plasmon Mode for a Colloidal Solution of Gold Nanoprisms. *J. Am. Chem. Soc.* **2005**, *127* (15), 5312–5313.

(36) Millstone, J. E.; Hurst, S. J.; Métraux, G. S.; Cutler, J. I.; Mirkin, C. A. Colloidal Gold and Silver Triangular Nanoprisms. *Small* **2009**, *5* (6), 646–664.

(37) O'Brien, M. N.; Jones, M. R.; Kohlstedt, K. L.; Schatz, G. C.; Mirkin, C. A. Uniform Circular Disks with Synthetically Tailorable Diameters: Two-Dimensional Nanoparticles for Plasmonics. *Nano Lett.* **2015**, *15* (2), 1012–1017.

(38) Kim, D.; Heo, J.; Kim, M.; Lee, Y. W.; Han, S. W. Size-Controlled Synthesis of

Monodisperse Gold Nanooctahedrons and Their Surface-Enhanced Raman Scattering Properties. *Chem. Phys. Lett.* **2009**, *468* (4–6), 245–248.

(39) Sohn, K.; Kim, F.; Pradel, K. C.; Wu, J.; Peng, Y.; Zhou, F.; Huang, J. Construction of Evolutionary Tree for Morphological Engineering of Nanoparticles. *ACS Nano* **2009**, *3* (8), 2191–2198.

(40) Yu, Y.; Zhang, Q.; Lu, X.; Lee, J. Y. Seed-Mediated Synthesis of Monodisperse Concave Trisoctahedral Gold Nanocrystals with Controllable Sizes. *J. Phys. Chem. C* **2010**, *114* (25), 11119–11126.

(41) Personick, M. L.; Langille, M. R.; Wu, J.; Mirkin, C. A. Synthesis of Gold Hexagonal Bipyramids Directed by Planar-Twinned Silver Triangular Nanoprisms. *J. Am. Chem. Soc.* **2013**, *135* (10), 3800–3803.

(42) Sapsford, K. E.; Algar, W. R.; Berti, L.; Gemmill, K. B.; Casey, B. J.; Oh, E.; Stewart, M. H.; Medintz, I. L. Functionalizing Nanoparticles with Biological Molecules: Developing Chemistries That Facilitate Nanotechnology. *Chem. Rev.* **2013**, *113* (3), 1904–2074.

(43) Whitesides, G. M.; Laibinis, P. E. Wet Chemical Approaches to The Characterization of Organic Surfaces: Self-Assembled Monolayers, Wetting, and The Physical-Organic Chemistry of The Solid-Liquid Interface. *Langmuir* **1990**, *6* (1), 87–96.

(44) Badia, A.; Singh, S.; Demers, L.; Cuccia, L.; Brown, G. R.; Lennox, R. B. Self-Assembled Monolayers on Gold Nanoparticles **. *Chem. Eur. J* **1996**, *2* (3), 359–363.

(45) Love, J. C.; Estroff, L. A.; Kriebel, J. K.; Nuzzo, R. G.; Whitesides, G. M. Self-Assembled Monolayers of Thiolates on Metals as a Form of Nanotechnology. *Chem. Rev.* **2005**, *105* (4), 1103–1170.

(46) Sabella, S.; Carney, R. P.; Brunetti, V.; Malvindi, M. A.; Al-Juffali, N.; Vecchio,

G.; Janes, S. M.; Bakr, O. M.; Cingolani, R.; Stellacci, F.; et al. A General Mechanism for Intracellular Toxicity of Metal-Containing Nanoparticles. *Nanoscale* **2014**, *6* (12), 7052–7061.

(47) Dykman, L.; Khlebtsov, N. Gold Nanoparticles in Biomedical Applications: Recent Advances and Perspectives. *Chem. Soc. Rev.* **2012**, *41* (6), 2256–2282.

(48) Yang, X.; Yang, M.; Pang, B.; Vara, M.; Xia, Y. Gold Nanomaterials at Work in Biomedicine. *Chem. Rev.* **2015**, *115* (19), 10410–10488.

(49) Peng, D.; Hu, S.; Hua, Y.; Xiao, Y.; Li, Z.; Wang, X.; Bi, D. Comparison of a New Gold-Immunochromatographic Assay for the Detection of Antibodies against Avian Influenza Virus with Hemagglutination Inhibition and Agar Gel Immunodiffusion Assays. *Vet. Immunol. Immunopathol.* **2007**, *117* (1–2), 17–25.

(50) Zhang, L.; Huang, Y.; Wang, J.; Rong, Y.; Lai, W.; Zhang, J.; Chen, T. Hierarchical Flowerlike Gold Nanoparticles Labeled Immunochromatography Test Strip for Highly Sensitive Detection of Escherichia Coli O157:H7. *Langmuir* **2015**, *31* (19), 5537–5544.

(51) Mirkin, C. A.; Letsinger, R. L.; Mucic, R. C.; Storhoff, J. J. A DNA-Based Method for Rationally Assembling Nanoparticles into Macroscopic Materials. *Nature* **1996**, *382* (6592), 607–609.

(52) Bao, P.; Frutos, A. G.; Greef, C.; Lahiri, J.; Muller, U.; Peterson, T. C.; Warden, L.; Xie, X. High-Sensitivity Detection of DNA Hybridization on Microarrays Using Resonance Light Scattering. *Anal. Chem.* **2002**, *74* (8), 1792–1797.

(53) Chithrani, B. D.; Ghazani, A. A.; Chan, W. C. W. Determining the Size and Shape Dependence of Gold Nanoparticle Uptake into Mammalian Cells. *Nano Lett.* **2006**, *6* (4), 662–668.

(54) Chithrani, B. D.; Chan, W. C. W. Elucidating the Mechanism of Cellular Uptake and Removal of Protein-Coated Gold Nanoparticles of Different Sizes and Shapes.

Nano Lett. **2007**, *7* (6), 1542–1550.

(55) Arnida; Jan??t-Amsbury, M. M.; Ray, A.; Peterson, C. M.; Ghandehari, H. Geometry and Surface Characteristics of Gold Nanoparticles Influence Their Biodistribution and Uptake by Macrophages. *Eur. J. Pharm. Biopharm.* **2011**, *77* (3), 417–423.

(56) Gratton, S. E. A.; Ropp, P. A.; Pohlhaus, P. D.; Luft, J. C.; Madden, V. J.; Napier, M. E.; DeSimone, J. M. The Effect of Particle Design on Cellular Internalization Pathways. *Proc. Natl. Acad. Sci.* **2008**, *105* (33), 11613–11618.

(57) Niikura, K.; Matsunaga, T.; Suzuki, T.; Kobayashi, S.; Yamaguchi, H.; Orba, Y.; Kawaguchi, A.; Hasegawa, H.; Kajino, K.; Ninomiya, T.; et al. Gold Nanoparticles as a Vaccine Platform: Influence of Size and Shape on Immunological Responses in Vitro and in Vivo. *ACS Nano* **2013**, *7* (5), 3926–3938.

(58) Ying Li, Martin Kröger, W. K. L. Shape Effect in Cellular Uptake of PEGylated Nanoparticles: Comparison between Sphere, Rod, Cube and Disk. *Nanoscale* **2015**, *7*, 16631.

(59) Vácha, R.; Martinez-Veracoechea, F. J.; Frenkel, D. Receptor-Mediated Endocytosis of Nanoparticles of Various Shapes. *Nano Lett.* **2011**, *11* (12), 5391–5395.

(60) Fernandes, R.; Smyth, N. R.; Muskens, O. L.; Nitti, S.; Heuer-Jungemann, A.; Ardern-Jones, M. R.; Kanaras, A. G. Interactions of Skin with Gold Nanoparticles of Different Surface Charge, Shape, and Functionality. *Small* **2015**, *11* (6), 713–721.

(61) Jiang, Y.; Huo, S.; Mizuhara, T.; Das, R.; Lee, Y.; Hou, S.; Moyano, D. F.; Duncan, B.; Liang, X.; Rotello, V. M. The Interplay of Size and Surface Functionality on the Cellular Uptake. *ACS Nano* **2015**, *9* (10), 9986–9993.

(62) Vivès, E.; Schmidt, J.; Pèlegrin, A. Cell-Penetrating and Cell-Targeting Peptides in

Drug Delivery. *Biochim. Biophys. Acta - Rev. Cancer* **2008**, *1786* (2), 126–138.

(63) Oh, E.; Delehanty, J. B.; Sapsford, K. E.; Susumu, K.; Goswami, R.; Blanco-Canosa, J. B.; Dawson, P. E.; Granek, J.; Shoff, M.; Zhang, Q.; et al. Cellular Uptake and Fate of PEGylated Gold Nanoparticles Is Dependent on Both Cell-Penetration Peptides and Particle Size. *ACS Nano* **2011**, *5* (8), 6434–6448.

(64) Khlebtsov, N.; Dykman, L. Biodistribution and Toxicity of Engineered Gold Nanoparticles: A Review of in Vitro and in Vivo Studies. *Chem. Soc. Rev.* **2011**, *40* (3), 1647–1671.

(65) Ernsting, M. J.; Murakami, M.; Roy, A.; Li, S. D. Factors Controlling the Pharmacokinetics, Biodistribution and Intratumoral Penetration of Nanoparticles. *J. Control. Release* **2013**, *172* (3), 782–794.

(66) Blanco, E.; Shen, H.; Ferrari, M. Principles of Nanoparticle Design for Overcoming Biological Barriers to Drug Delivery. *Nat. Biotechnol.* **2015**, *33* (9), 941–951.

(67) Decuzzi, P.; Godin, B.; Tanaka, T.; Lee, S. Y.; Chiappini, C.; Liu, X.; Ferrari, M. Size and Shape Effects in the Biodistribution of Intravascularly Injected Particles. *J. Control. Release* **2010**, *141* (3), 320–327.

(68) Tan, J.; Shah, S.; Thomas, A.; Ou-Yang, H. D.; Liu, Y. The Influence of Size, Shape and Vessel Geometry on Nanoparticle Distribution. *Microfluid. Nanofluidics* **2013**, *14* (1–2), 77–87.

(69) Black, K. C. L.; Wang, Y.; Luehmann, H. P.; Cai, X.; Xing, W.; Pang, B.; Zhao, Y.; Cutler, C. S.; Wang, L. V.; Liu, Y.; et al. Radioactive198Au-Doped Nanostructures with Different Shapes for in Vivo Analyses of Their Biodistribution, Tumor Uptake, and Intratumoral Distribution. *ACS Nano* **2014**, *8* (5), 4385–4394.

(70) Elci, S. G.; Jiang, Y.; Yan, B.; Kim, S. T.; Saha, K.; Moyano, D. F.; Yesilbag

Tonga, G.; Jackson, L. C.; Rotello, V. M.; Vachet, R. W. Surface Charge Controls the Suborgan Biodistributions of Gold Nanoparticles. *ACS Nano* **2016**, *10* (5), 5536–5542.

(71) García, K. P.; Zarschler, K.; Barbaro, L.; Barreto, J. A.; O'Malley, W.; Spiccia, L.; Stephan, H.; Graham, B. Zwitterionic-Coated "Stealth" Nanoparticles for Biomedical Applications: Recent Advances in Countering Biomolecular Corona Formation and Uptake by the Mononuclear Phagocyte System. *Small* **2014**, *10* (13), 2516–2529.

(72) Schöttler, S.; Becker, G.; Winzen, S.; Steinbach, T.; Mohr, K.; Landfester, K.; Mailänder, V.; Wurm, F. R. Protein Adsorption Is Required for Stealth Effect of Poly(Ethylene Glycol)- and Poly(Phosphoester)-Coated Nanocarriers. *Nat. Nanotechnol.* **2016**, *11* (4), 372–377.

(73) Krammer, F.; Smith, G. J. D.; Fouchier, R. A. M.; Peiris, M.; Kedzierska, K.; Doherty, P. C.; Palese, P.; Shaw, M. L.; Treanor, J.; Webster, R. G.; et al. Influenza. *Nat. Rev. Dis. Prim.* **2018**, *4* (1), 1–21.

(74) Sano, K.; Ainai, A.; Suzuki, T.; Hasegawa, H. The Road to a More Effective Influenza Vaccine: Up to Date Studies and Future Prospects. *Vaccine* **2017**, *35* (40), 5388–5395.

(75) Asanuma, H.; Ohori, J.; McGhee, J.; Fujihashi, K. Past Efforts and Future Prospects for a Nasal Influenza Vaccine. *Clin. Immunol. Endocr. Metab. Drugs* **2015**, *2* (1), 13–26.

(76) Ichinohe, T.; Watanabe, I.; Ito, S.; Fujii, H.; Moriyama, M.; Tamura, S.; Takahashi, H.; Sawa, H.; Chiba, J.; Kurata, T.; et al. Synthetic Double-Stranded RNA Poly (I : C) Combined with Mucosal Vaccine Protects against Influenza Virus Infection. *J. Virol.* **2005**, *79* (5), 2910–2919.

(77) Ekiert, D. C.; Bhabha, G.; Elsliger, M.-A.; Friesen, R. H. E.; Jongeneelen, M.;

Throsby, M.; Goudsmit, J.; Wilson, I. A. Antibody Recognition of a Highly Conserved Influenza Virus Epitope. *Science (80-.).* **2009**, *324* (5924), 246–251.

(78) Sui, J.; Hwang, W. C.; Perez, S.; Wei, G.; Aird, D.; Chen, L.; Santelli, E.; Stec, B.; Cadwell, G.; Ali, M.; et al. Structural and Functional Bases for Broad-Spectrum Neutralization of Avian and Human Influenza A Viruses. *Nat. Struct. Mol. Biol.* **2009**, *16* (3), 265–273.

(79) Wei, C.-J.; Boyington, J. C.; McTamney, P. M.; Kong, W.-P.; Pearce, M. B.; Xu, L.; Andersen, H.; Rao, S.; Tumpey, T. M.; Yang, Z.-Y.; et al. Induction of Broadly Neutralizing H1N1 Influenza Antibodies by Vaccination. *Science (80-.).* **2010**, *329* (5995), 1060–1064.

(80) Whittle, J. R. R.; Zhang, R.; Khurana, S.; King, L. R.; Manischewitz, J.; Golding, H.; Dormitzer, P. R.; Haynes, B. F.; Walter, E. B.; Moody, M. A.; et al. Broadly Neutralizing Human Antibody That Recognizes the Receptor-Binding Pocket of Influenza Virus Hemagglutinin. *Proc. Natl. Acad. Sci.* **2011**, *108* (34), 14216–14221.

(81) Mallajosyula, V. V. A.; Citron, M.; Ferrara, F.; Lu, X.; Callahan, C.; Heidecker, G. J.; Sarma, S. P.; Flynn, J. A.; Temperton, N. J.; Liang, X.; et al. Influenza Hemagglutinin Stem-Fragment Immunogen Elicits Broadly Neutralizing Antibodies and Confers Heterologous Protection. *Proc. Natl. Acad. Sci.* **2014**, *111* (25), E2514–E2523.

(82) Lu, Y.; Welsh, J. P.; Swartz, J. R. Production and Stabilization of the Trimeric Influenza Hemagglutinin Stem Domain for Potentially Broadly Protective Influenza Vaccines. *Proc. Natl. Acad. Sci.* **2014**, *111* (1), 125–130.

(83) Gupta, R. K. Aluminum Compounds as Vaccine Adjuvants. *Adv. Drug Deliv. Rev.* **1998**, *32* (3), 155–172.

(84) Hemmi, H.; Takeuchi, O.; Kawai, T.; Kaisho, T.; Sato, S.; Sanjo, H.; Matsumoto,

M.; Hoshino, K.; Wagner, H.; Takeda, K.; et al. A Toll-like Receptor Recognizes Bacterial DNA. *Nature* **2000**, *408* (6813), 740–745.

(85) Alexopoulou, L.; Holt, A. C.; Medzhitov, R.; Flavell, R. A. Recognition of Double-Stranded RNA and Activation of NF-KB by Toll-like Receptor 3. *Nature* **2001**, *413* (6857), 732–738.

(86) Desmet, C. J.; Ishii, K. J. Nucleic Acid Sensing at the Interface between Innate and Adaptive Immunity in Vaccination. *Nat. Rev. Immunol.* **2012**, *12* (7), 479–491.

(87) Ohto, U.; Shibata, T.; Tanji, H.; Ishida, H.; Krayukhina, E.; Uchiyama, S.; Miyake, K.; Shimizu, T. Structural Basis of CpG and Inhibitory DNA Recognition by Toll-like Receptor 9. *Nature* **2015**, *520* (7549), 702–705.

(88) Sun, B.; Ji, Z.; Liao, Y. P.; Wang, M.; Wang, X.; Dong, J.; Chang, C. H.; Li, R.; Zhang, H.; Nel, A. E.; et al. Engineering an Effective Immune Adjuvant by Designed Control of Shape and Crystallinity of Aluminum Oxyhydroxide Nanoparticles. *ACS Nano* **2013**, *7* (12), 10834–10849.

(89) Marichal, T.; Ohata, K.; Bedoret, D.; Mesnil, C.; Sabatel, C.; Kobiyama, K.; Lekeux, P.; Coban, C.; Akira, S.; Ishii, K. J.; et al. DNA Released from Dying Host Cells Mediates Aluminum Adjuvant Activity. *Nat. Med.* **2011**, *17* (8), 996–1002.

(90) Guy, B. The Perfect Mix: Recent Progress in Adjuvant Research. *Nat. Rev. Microbiol.* **2007**, *5* (7), 505–517.

(91) Maraskovsky, E.; Schnurr, M.; Wilson, N. S.; Robson, N. C.; Boyle, J.; Drane, D. Development of Prophylactic and Therapeutic Vaccines Using the ISCOMATRIX Adjuvant. *Immunol. Cell Biol.* **2009**, *87* (5), 371–376.

(92) Skidmore, B. J.; Chiller, J. M.; Morrison, D. C.; Weigle, W. O. Immunologic Properties of Bacterial Lipopolysaccharide (LPS): Correlation between the Mitogenic , Adjuvant , and Immunogenic Activities. *J. Immunol.* **1975**, *114*, 770–

775.

(93) Eisenbarth, S. C.; Piggott, D. A.; Huleatt, J. W.; Visintin, I.; Herrick, C. A.; Bottomly, K. Lipopolysaccharide-Enhanced, Toll-like Receptor 4–dependent T Helper Cell Type 2 Responses to Inhaled Antigen. *J. Exp. Med.* **2002**, *196* (12), 1645–1651.

(94) Shiosaka, S.; Kiyama, H.; Wanaka, A.; Masaya, T. A New Method for Producing a Specific and High Titre Antibody against Glutamate Using Colloidal Gold as a Carrier. *Brain Res.* **1986**, *382* (2), 399–403.

(95) Smith, D. M.; Simon, J. K.; Baker, J. R. Applications of Nanotechnology for Immunology. *Nat. Rev. Immunol.* **2013**, *13* (8), 592–605.

(96) Kanekiyo, M.; Wei, C.-J.; Yassine, H. M.; McTamney, P. M.; Boyington, J. C.; Whittle, J. R. R.; Rao, S. S.; Kong, W.-P.; Wang, L.; Nabel, G. J. Self-Assembling Influenza Nanoparticle Vaccines Elicit Broadly Neutralizing H1N1 Antibodies. *Nature* **2013**, *499* (7456), 102–106.

(97) Nochi, T.; Yuki, Y.; Takahashi, H.; Sawada, S.; Mejima, M.; Kohda, T.; Harada, N.; Kong, I. G.; Sato, A.; Kataoka, N.; et al. Nanogel Antigenic Protein-Delivery System for Adjuvant-Free Intranasal Vaccines. *Nat. Mater.* **2010**, *9* (7), 572–578.

(98) Matsuo, K.; Koizumi, H.; Akashi, M.; Nakagawa, S.; Fujita, T.; Yamamoto, A.; Okada, N. Intranasal Immunization with Poly (γ -Glutamic Acid) Nanoparticles Entrapping Antigenic Proteins Can Induce Potent Tumor Immunity. *J. Control. Release* **2011**, *152* (2), 310–316.

(99) Radovic-Moreno, A. F.; Chernyak, N.; Mader, C. C.; Nallagatla, S.; Kang, R. S.; Hao, L.; Walker, D. A.; Halo, T. L.; Merkel, T. J.; Rische, C. H.; et al. Immunomodulatory Spherical Nucleic Acids. *Proc. Natl. Acad. Sci. U. S. A.* **2015**, *112* (13), 3892–3897.

(100) Zhang, P.; Chiu, Y.-C.; Tostanoski, L. H.; Jewell, C. M. Polyelectrolyte

Multilayers Assembled Entirely from Immune Signals on Gold Nanoparticle Templates Promote Antigen-Specific T Cell Response. *ACS Nano* **2015**, *9* (6), 6465–6477.

(101) Kusaka, T.; Nakayama, M.; Nakamura, K.; Ishimiya, M.; Furusawa, E.; Ogasawara, K. Effect of Silica Particle Size on Macrophage Inflammatory Responses. *PLoS One* **2014**, *9* (3), e92634.

(102) Hutter, E.; Boridy, S.; Labrecque, S.; Lalancette-Hébert, M.; Kriz, J.; Winnik, F. M.; Maysinger, D. Microglial Response to Gold Nanoparticles. *ACS Nano* **2010**, *4* (5), 2595–2606.

(103) Ji, Z.; Wang, X.; Zhang, H.; Lin, S.; Meng, H.; Sun, B.; George, S.; Xia, T.; Nel, A. E.; Zink, J. I. Designed Synthesis of CeO2 Nanorods and Nanowires for Studying Toxicological Effects of High Aspect Ratio Nanomaterials. *ACS Nano* **2012**, *6* (6), 5366–5380.

(104) Lunov, O.; Syrovets, T.; Loos, C.; Nienhaus, G. U.; Mailänder, V.; Landfester, K.; Rouis, M.; Simmet, T. Amino-Functionalized Polystyrene Nanoparticles Activate the NLRP3 Inflammasome in Human Macrophages. *ACS Nano* **2011**, *5* (12), 9648–9657.

(105) Mottram, P. L.; Leong, D.; Crimeen-Irwin, B.; Gloster, S.; Xiang, S. D.; Meanger, J.; Ghildyal, R.; Vardaxis, N.; Plebanski, M. Type 1 and 2 Immunity Following Vaccination Is Influenced by Nanoparticle Size: Formulation of a Model Vaccine for Respiratory Syncytial Virus. *Mol. Pharm.* **2007**, *4* (1), 73–84.

(106) Bachmann, M. F.; Jennings, G. T. Vaccine Delivery: A Matter of Size, Geometry, Kinetics and Molecular Patterns. *Nat. Rev. Immunol.* **2010**, *10* (11), 787–796.

(107) Niikura, K.; Matsunaga, T.; Suzuki, T.; Kobayashi, S.; Yamaguchi, H.; Orba, Y.; Kawaguchi, A.; Hasegawa, H.; Kajino, K.; Ninomiya, T.; et al. Gold Nanoparticles as a Vaccine Platform: Influence of Size and Shape on Immunological Responses

in Vitro and in Vivo. *ACS Nano* **2013**, *7* (5), 3926–3938.

(108) Kang, S.; Ahn, S.; Lee, J.; Kim, J. Y.; Choi, M.; Gujrati, V.; Kim, H.; Kim, J.; Shin, E. C.; Jon, S. Effects of Gold Nanoparticle-Based Vaccine Size on Lymph Node Delivery and Cytotoxic T-Lymphocyte Responses. *J. Control. Release* **2017**, *256* (March), 56–67.

(109) Zhou, Q.; Zhang, Y.; Du, J.; Li, Y.; Zhou, Y.; Fu, Q.; Zhang, J.; Wang, X.; Zhan, L. Different-Sized Gold Nanoparticle Activator/Antigen Increases Dendritic Cells Accumulation in Liver-Draining Lymph Nodes and CD8+ T Cell Responses. *ACS Nano* **2016**, *10* (2), 2678–2692.

(110) Liu, Y.; Balachandran, Y. L.; Li, D.; Shao, Y.; Jiang, X. Polyvinylpyrrolidone–Poly(Ethylene Glycol) Modified Silver Nanorods Can Be a Safe, Noncarrier Adjuvant for HIV Vaccine. *ACS Nano* **2016**, *10* (3), 3589–3596.

Chapter 2

Shape-dependent adjuvanticity of gold nanoparticle conjugated RNA adjuvants for intranasal inactivated influenza vaccine

2-1 Introduction

Currently, most vaccines are applied subcutaneously (SC) or intramuscularly (IM) and the preference for the administration route can vary depending on the infectious diseases. The current standard influenza vaccine is a SC or IM injection type. Intranasal influenza vaccination has various advantages over subcutaneous or intramuscular vaccination. First, intranasal vaccines can induce a mucosal IgA antibody response in the upper respiratory tract, promoting protection from influenza virus infection (Figure 2-1).[1] Second, intranasal vaccination is needle-free. This simplifies the vaccination process and reduces the risk of accidental needle-stick injury. Live attenuated intranasal influenza vaccines have been approved for clinical use; however, these intranasal vaccines can be inoculated to only limited age groups. To apply intranasal influenza vaccines to a wider range of patients, intranasal administration of inactivated influenza vaccines is considered to be a promising strategy in terms of efficacy and safety.[2] However, in general, intranasal inactivated influenza vaccines need adjuvants to induce an adequate immune response.

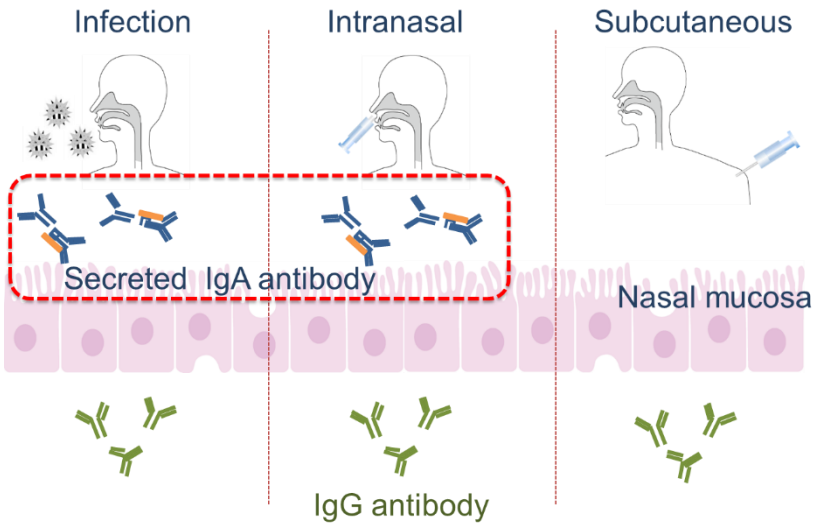

Figure 2-1 The effect of vaccine administration route on antibody response.

Synthetic RNA analogues [e.g., poly(I:C)] work as an adjuvant for intranasal inactivated influenza vaccines.[3] The poly(I:C) interacts with several receptors, such as toll-like receptor 3 (TLR3), to trigger innate immune responses (Figure 2-2).[4] Although it has been reported that only 40 – 50 base pairs are required for double-stranded RNA (dsRNA) to interact with TLR3(Figure 2-3 A)[5,6], the adjuvanticity of poly(I:C)s is strongly dependent on their molecular weight (Figure 2-3 B, Table 2-1). Poly(I:C)s with a higher molecular weight tend to show not only higher adjuvanticity but also higher toxicity.[7,8] Therefore, low-molecular-weight poly(I:C), which shows less toxicity, is required for clinical use as an adjuvant from the view point of safety. Recently, Nakano et al. reported a new synthetic approach to low-molecular-weight (~ 400 bp) poly(I:C) with a narrow size distribution. They found that the annealing of multiple 40-base polyI molecules with a single 400-base polyC molecule produces a double-stranded poly(I:C) with uniform molecular weight distribution. This combination prevents the elongation of dsRNA caused by their linking and enables the use of low-molecular weight poly(I:C) of stable length, reducing its toxicity (Figure 2-3 C).[9] This unevenly structured poly(I:C) was referred to as uPIC(40:400). Although this uPIC(40:400) is a promising adjuvant due to its low toxicity, its adjuvanticity remains inadequate.

Table 2-1 Affinity of TLR3 ectodomain binding to dsRNA.[6]

	$K_{d\_apparent}$, nM		
dsRNA length, bp	pH 6.5	pH 6.0	pH 5.5
39	2,250 ± 70	510 ± 23	72.6 ± 1.7
48	2,610 ± 80	156 ± 7	13.6 ± 0.3
139	487 ± 12	31.7 ± 0.6	9.19 ± 0.21
540	782 ± 15	28.2 ± 0.9	4.64 ± 0.11

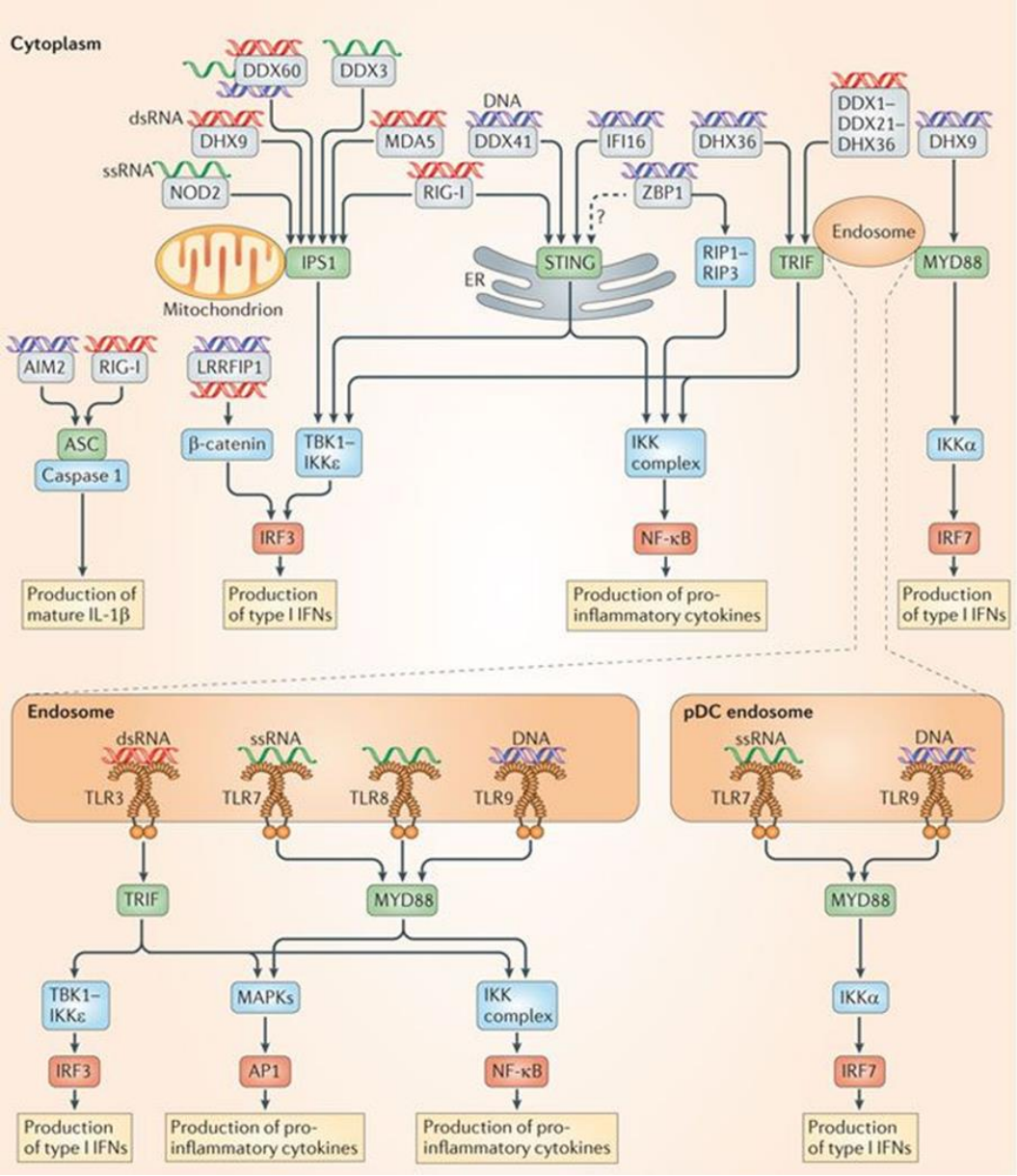

Figure 2-2 Overview of nucleic acid-sensing receptors and signaling pathway.[4]

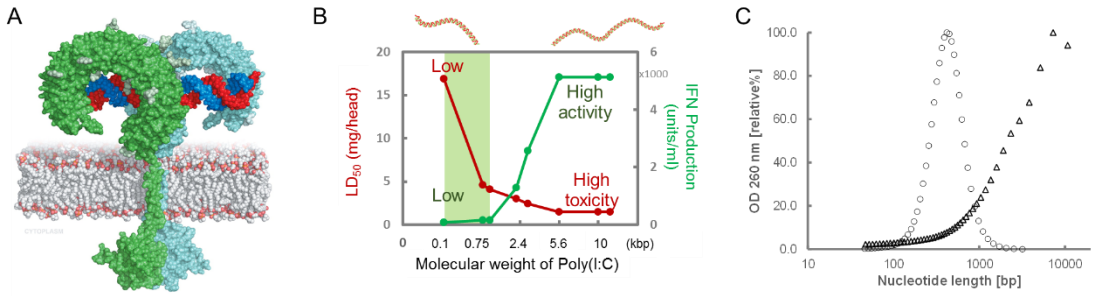

Figure 2-3 (A) Model of the dsRNA and TLR3 signaling complex.[5] (B) Relationship between the molecular weight of poly(I:C) and biological activity.[7] (C) Molecular weight distribution of uPIC(40:400) (circles) and commercially available high-molecular-weight poly(I:C) (uPIC(40:400), triangles) used as positive controls in this study.[9]

Nanoparticles are good candidates for use as uPIC(40:400) scaffolds to enhance adjuvanticity. Nanoparticles have already been widely used as vaccine carriers due to their ability to enhance cellular uptake of drugs[10–12] and activate immune systems.[13–20] The immobilization of antigens onto nanoparticles and resultant enhancement of immunogenicity were initially demonstrated in the 1980s.[13] Regarding the targeting of the nasal cavity, antigen delivery using nanogels[21] and polymer nanoparticles[22] has been shown to be effective. Recently, the effects of antigen carrier size and shape have also been investigated as the size and shape of nanoparticles affect both nanoparticle uptake[23–32] and immune responses.[33–39] Plebanski et al. reported that the size of the antigen carrier influenced the immune response pathway in vivo after intradermal immunization.[33] It was previously demonstrated that the shape of the antigen scaffold affected on vaccine efficacy and cytokine production in mice immunized intraperitoneally.[36] Recently, adjuvant conjugation onto AuNPs and subsequent application to vaccines has been demonstrated. Radovic-Moreno et al. reported that the conjugation of CpG oligonucleotides onto AuNPs enabled the adjuvant dose to be decreased while enhancing vaccine potency in systemically immunized mice.[40] Zhang et al. reported an enhanced antigen-specific T cell response in mice intradermally immunized with multilayered co-assemblies of antigen and poly(I:C) on AuNPs.[41] Zhou et al. demonstrated that there was an optimal size for AuNPs used as an antigen or adjuvant carrier to enhance cellular immunity both in vitro and in vivo.[38] However, for intranasal vaccines, the influence of the shape and size of the carrier nanomaterial on adjuvanticity has not been explored.

In this chapter, I aimed to clarify the shape- and size-related effects of AuNPs as scaffolds for uPIC(40:400) adjuvants for the intranasal influenza vaccine through a comparison with conventional subcutaneous vaccination. I chose AuNPs as scaffolds as they were easily synthesized to the desired shape and size compared to other materials. AuNP-uPIC(40:400) complexes (referred to as AuNP-PICs) were prepared by the electrostatic conjugation of uPIC(40:400) onto the AuNP surface. The AuNP-PICs were administrated subcutaneously or intranasally with influenza virus hemagglutinin (HA, 10 or 100 ng). The SC administration was chosen as a standard reference to IN administration in this study. The secreted levels of systemic IgG and mucosal IgA antibodies against influenza virus hemagglutinin (HA) in the serum or nasal wash were evaluated. The activities of the AuNP-PIC adjuvants were further investigated from the virus levels remaining in the nasal wash after challenge infection (Figure. 2-4). Further, immunological responses relating inflammation were also evaluated to investigate the risk of side reaction due to excess immune responses *in vitro*.

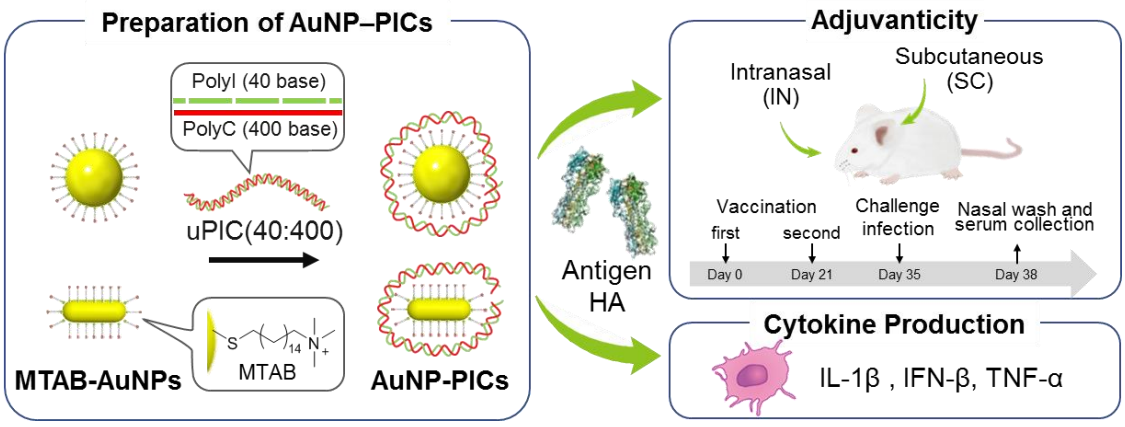

Figure 2-4 Preparation of AuNP/uPIC(40:400) conjugates and evaluation of the adjuvanticity and cytokine production.

2-2 Experimental section

2-2-1 General Information

All commercially available reagents were used without further purification. Cetyltrimethylammonium chloride (CTAC), cetyltrimethylammonium bromide (CTAB), hydrogen tetra- chloroaurate (III) tetrahydrate, silver nitrate and L(+)-ascorbic acid were purchased from Wako Pure Chemical Industries (Japan). Sodium borohydride was purchased from TOKYO Chemical Industry (Japan). uPIC(40:400) was supplied from Kyowa Hakko Bio (Japan). Poly(I:C) was purchased from GE Healthcare (USA). In this study, I used two different strains of H1N1. Ether-split vaccine of X-179A was kindly provided by the Research Foundation for Microbial Disease of Osaka University (BIKEN, Kanonji, Kagawa, Japan). X-179A is high-growth reassortant vaccine strains derived from A/California/7/09 (H1N1)pdm09 for vaccine production in embryonic eggs, and influenza vaccines in clinical use at the time of our animal experiment contained HA antigens of X-179. Mouse-adapted A/Narita/1/09 (H1N1)pdm09 virus, which is not a reassortant strain, was prepared according to the previous report.[42] This strain is derived from a H1N1 pandemic human isolate in 2009, which has the identical antigenicity to A/California/ 7/09 (H1N1)pdm09 virus. In general, human influenza virus cannot replicate efficiently in mice, requiring that mice-adaptation process for mice challenge experiment. The mouse-adapted A/ Narita/1/09 (H1N1)pdm09 virus was developed for a mice challenge experiment to test the efficacy of HA vaccines of a H1N1 pandemic virus.[42] Anti-Ms IgA (a)Ab HSA (Biotin) was purchased from KPL (SeraCare Life Sciences, USA). Biotin-SP (long spacer) AffiniPure Goat Anti-Mouse IgG (Fcg fragment specific) was purchased from Jackson ImmunoResearch (USA). Streptavidin-AP was purchased from Thermo Fisher Scientific (USA). Phosphatase substrate was purchased from Sigma-Aldrich (USA). BALB/c mice were purchased from Japan SLC (Japan). C3H/HeNJcl mice were purchased from Hokudo (Japan). Dulbecco's modified Eagle's medium (DMEM), RPMI-1640 and

lipopolysaccharides (LPS) were purchased from Sigma-Aldrich (USA). DMEM (no phenol red), fetal bovine serum (FBS) and penicillin–streptomycin were purchased from GIBCO (USA). Recombinant murine GM-CSF was purchased from PEPROTECH (USA). Cell Counting Kit-8 was purchased from DOJINDO (Japan). Interleukin-1β (IL-1β) and tumor necrosis factor-a (TNF-α) ELISA kits were purchased from R&D systems (USA). Interferon-β (IFN-β) ELISA kit was purchased from PBL Assay Science (USA). Statistical analysis was performed using the GraphPad Prism statistical software package (Version 7.01: Graph Pad Software Inc., USA). The threshold for statistical significance was set at 5% ($p < 0.05$).

2-2-2 Preparation of gold nanoparticle and RNA conjugates

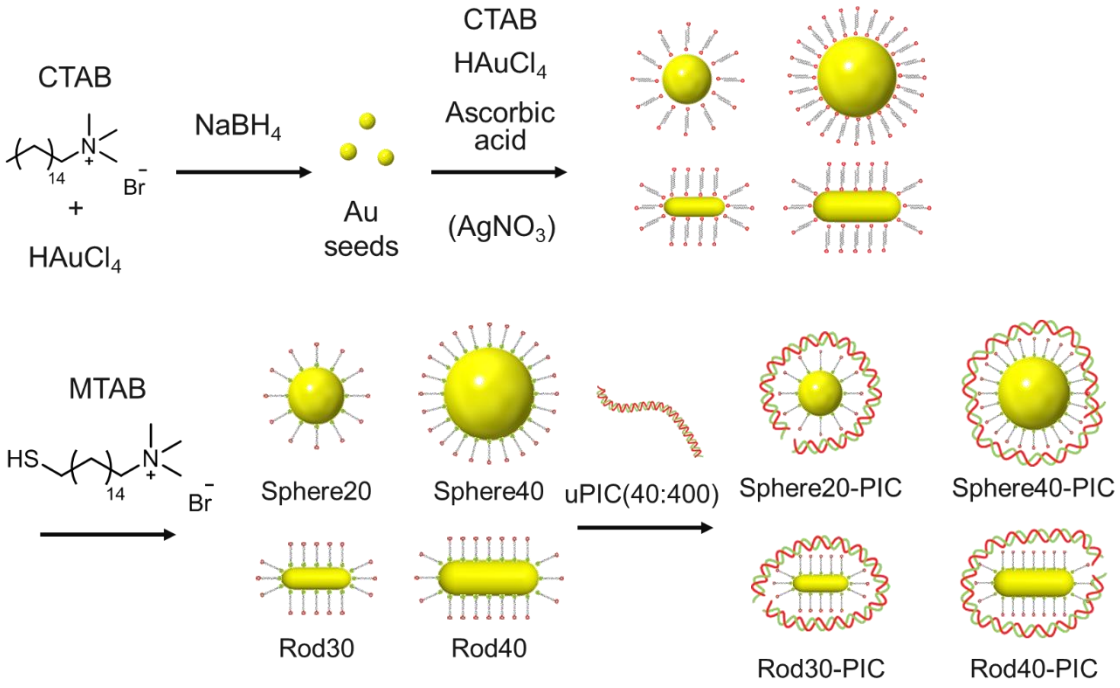

Figure 2-5 Schematic illustration of AuNP-PIC preparation.

2-2-2-1 Synthesis of 16-mercaptohexadecylammonium bromide (MTAB)[43]

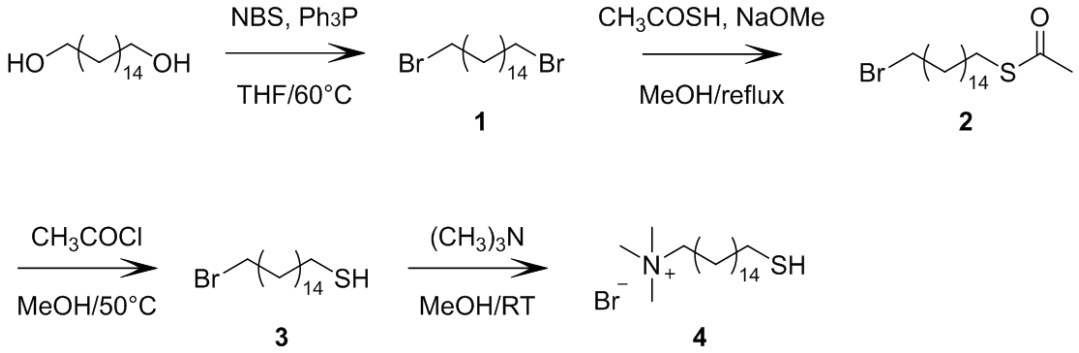

Figure 2-6 Synthetic scheme of MTAB.

1,16-dibromohexadecane, **1**

Triphenylphosphine (TPP, 3.9 mmol, 15 mmol) in 30 mL of THF was added to a stirred solution of *N*-bromosuccinamide (NBS, 2.7 g, 15 mmol) in 25 mL THF at 0°C. 1,16-hexadecandiol (1.0 g, 3.9 mmol) in 20 mL THF was slowly added to the solution under vigorous stirring. The resultant solution was heated at 60°C for 6 hours. THF was removed under the reduced pressure and the residue was recrystallized from ethanol in freezer to obtain 0.56 g of compound 1 (1.4 mmol, 37 %) as white powder.

^{1}HNMR ($CDCl_3$, 400 MHz): δ 1.19-1.42 (m, 24H), 1.83 (qn, 4H, J = 7 Hz), 3.39 (t, 4H, J = 7Hz)

16-bromo-1-hexadecanethioacetate, **2**

Compound **1** (0.45 g, 1.2 mmol) was dissolved 20 mL methanol in three-neck flask. Separately, sodium methoxide (NaOMe, 56 mg, 1.0 mmol) and thioacetic acid (86 μL, 1.2 mmol) were dissolved in 6 mL of methanol. This solution was added to the solution of compound 1 over the course of 4 hours by using drop-funnel. The solution heated at 85°C for totally 5 h. The solvent was removed under reduced pressure and the residue was purified flash chromatography on silica gel (Hexane: Ethyl acetate = 50: 1) to yield

compound **2** (0.27 g, 0.71 mmol, 61%).

^{1}HNMR ($CDCl_3$, 400 MHz): δ 1.22-1.40 (m, 24H), 1.4 (m, 2H), 1.83 (qn, 2H, J = 7.2 Hz), 2.3 (s, 3 H), 2.84 (t, 2H, J = 7.2 Hz), 3.39 (t, 2H, J = 6.8 Hz)

16-bromo-1-hexadecanethiol, **3**

To a stirred solution of compound **2** (0.25 g, 0.7 mmol) in 5 mL of methanol, 2.3 mL of acetyl chloride was added dropwise. The reaction mixture was heated at 50°C for 4 hours. After reaction, dichloromethane was added to the reaction solution and acids were removed by washing with water. The organic layer was dried over sodium sulfate. The solvent was removed under reduced pressure to obtain compound **3** (0.23 g, 0.7 mmol, 100 %).

^{1}HNMR ($CDCl_3$, 400 MHz): δ 1.24-1.40 (m, 24H), 1.59 (2H, qn, J = 7.3 Hz), 1.83 (2H, qn, J = 7 Hz), 2.5 (q, 2H, J = 7.3 Hz), 3.38 (t, 2H, J = 7 Hz)

16-mercaptohexadecyltrimethylammonium bromide (MTAB), **4**

To a solution of compound 3 (0.23 g, 0.65 mmol) in 6 mL of ethyl acetate, 7 mL of 4.2 M ethanolic solution of trimethyl amine was added and the mixture was stirred at room temperature for 5 days. The solvent was removed under reduced pressure and white powder was precipitated with ethyl acetate. The precipitate was collected by suction filtration. The residue was washed with ethyl acetate and dried to obtain 0.13 g of MTAB (0.32 mmol, 49 %, total yield: 8.2 %).

^{1}HNMR ($CDCl_3$, 400 MHz): δ 1.23- 1.35 (m, 24H), 1.65 (m, 2H), 1.70 (m, 2H), 2.67 (t, 2H, J = 7.4 Hz), 3.44 (s, 9H), 3.63-3.67 (m, 2H)

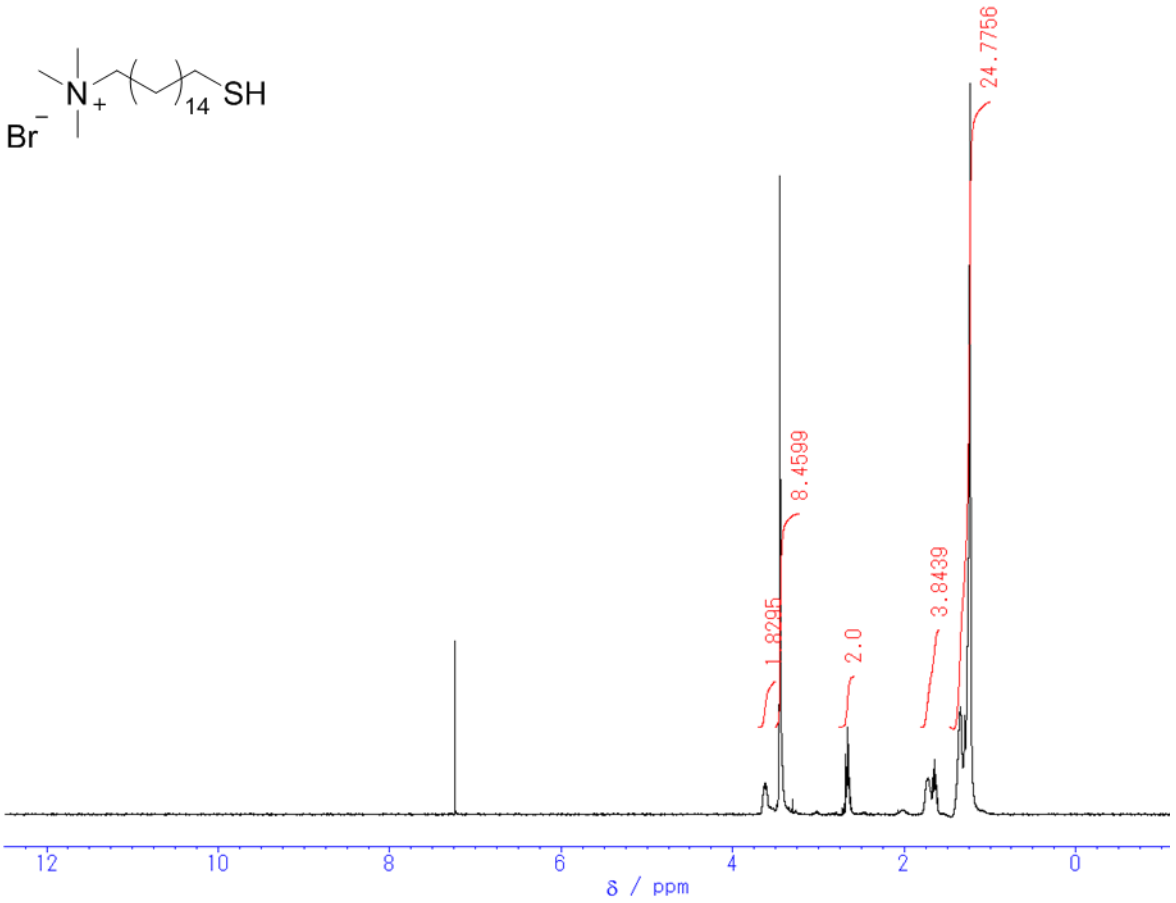

Figure 2-7 ^{1}H NMR spectrum of MTAB in $CDCl_3$.

2-2-2-2 Synthesis of spherical and rod-shaped gold nanoparticles

Cetyltrimethylammonium (CTA)-stabilized AuNPs were synthesized by a seeding growth method.[4445]

○Spherical AuNP (CTA-Sphere20 and CTA-Spehre40)

For the preparation of the seed solution, $HAuCl_4$ $4H_2O$ (10 mM, 250 μL) was added to the solution of cetyltrimethylammmonium chloride (CTAC) (0.1 M, 7.5 mL). Subsequently, fresh $NaBH_4$ (10 mM 600 μL) were added to the solution. Then the solution was undisturbed at 30°C for a 1 hour.

For the preparation of growth solution, cetyltrimethylammonium bromide (CTAB) (0.1 M, 3.75 mL), CTAC (0.1 M, 3.75 mL), milliQ water (37.5 mL), $HAuCl_4$ $4H_2O$ (10 mM, 925 μL) and L-ascorbic acid (0.1 M, 4.5 mL) were added to 50 mL plastic tube in this order. To synthesis spherical gold nanoparticles, 10-fold diluted seed solution (233 or 23.3 μL, for CTA-Sphere20 and CTA-Spehre40, respectively) was added. The mixtures were undisturbed at 30°C for 3 hours or more.

○Rod-shaped AuNP (CTA-Rod30 and CTA-Rod40)

For the preparation of the seed solution, $HAuCl_4$ $4H_2O$ (10 mM, 250 μL) was added to the solution of CTAB (0.1 M, 7.5 mL). Subsequently, fresh $NaBH_4$ (10 mM 600 μL) were added to the solution. Then the solution was undisturbed at 30°C for a 1 hour.

For the preparation of growth solution, CTAB (0.1 M, 38 mL), $HAuCl_4$ $4H_2O$ (10 mM, 1.6 mL), $AgNO_3$ (10 mM, 240 μL) and L-ascorbic acid (0.1 M, 260 μL) were added to 50 mL plastic tube in this order. To the solution, seed solution (800 or 260 μL for CTA-Rod30 and CTA-Rod40, respectively) was added. The mixtures were undisturbed at 30°C for 3 hours or more.

2-2-2-3 Preparation of gold nanoparticle and RNA conjugates (AuNP-PIC)

After 48 mL of CTA-Sphere20, CTA-Sphere40, CTA-Rod30 and CTA-Rod40 solutions were centrifuged twice and concentrated to c.a. 2 mL, 5 mg of MTAB was added to the AuNP solutions. Solutions were incubated overnight at 42°C. Excess MTAB molecules were removed by centrifugation 4 times to produce MTAB-functionalized AuNPs (MTAB-AuNPs). The concentrations of AuNPs were determined by extinction spectrometry.[46,47]

Scanning transmission electron microscopic (STEM) images were obtained using a STEM HD-2000 system (Hitachi High-Tech Manufacturing & Service Co., Ltd., Japan) with 200 kV accelerating voltage. Extinction spectra were measured with a UV-vis spectrometer (UV-2600; Shimadzu Corporation, Japan). Zeta potentials were measured using a Delsa Nano HC Particle Analyzer (Beckman Coulter, USA). Hydrodynamic diameters were measured using ELSZ-2000 (Otsuka Electronics Co., Ltd., Japan).

MTAB-AuNPs were added to a uPIC(40:400) solution reconstituted in distilled water ($V_{MTAB\text{-}AuNPs}/V_{uPIC(40:400)}$ = 1:1) and mixed gently. The concentration varied according to the experiment. As a typical example, a MTAB-AuNP aqueous solution (particle conc. 8.0 nM) was added to the uPIC(40:400) solution (200 μg/mL) for preparation of AuNP-PICs (Final sample conc.: 4.0 nM MTAB-AuNPs and 100 μg/mL uPIC(40:400)). Mixtures were incubated overnight at 4°C. Prepared solutions were used for characterization, vaccination and cell studies without purification. Zeta potential measurements were carried out in MilliQ water at concentrations of 0.4 nM for MTAB-AuNPs and 10 μg/mL for uPIC(40:400). For the calculation of the number of uPIC(40:400) molecules immobilized on a single AuNP, AuNP-PICs solutions were centrifuged (14,100g, 50 min) to precipitate AuNPs completely and the concentration of unbound uPIC(40:400) in the supernatant was determine by UV-Vis absorption at 250 nm.

2-2-3 Evaluation of conjugates adjuvanticity

2-2-3-1 Vaccination to mice

Six- to eight-week-old female BALB/c mice (n = 5–6 per group) were immunized intranasally or subcutaneously twice at a 3-week interval with 100 or 10 ng of ether-split influenza vaccine made from vaccine strain X-179A, derived from A/California/7/09 (H1N1)pdm09, in the presence of AuNPs alone, AuNP–PICs or uPIC(40:400). Intranasal vacci- nation was performed by instillation of 5 mL of vaccine solution into each nostril (total 10 mL per mouse). Subcutaneous vaccination was performed by injection of 100 mL of vaccine solution into the dorsal part of the cervical region.[48,49] All mice were challenged with mouse-adapted A/Narita/1/09 (H1N1)pdm09 virus (A/NRT), 2 weeks after the last vaccination. Infection was performed by inserting 2 mL of a suspension containing A/NRT in each nostril (total 4 mL, 40 000 plaque-forming units [PFUs] per mouse). At 3 days post-infection, all mice were sacrificed to collect serum and nasal wash samples for determination of antibody levels and virus titers as previously described. Nasal wash specimens were obtained from mice by washing the nasal cavity of the isolated upper head with 1 mL of PBS(-) containing 0.1% bovine serum albumin and antibiotics.[50] In the experiments on intranasal immunization, I also checked the virus titers as well as antibody responses, which correspond to the levels of virus replication in the nasal mucosal tissues in the vaccinated animals after virus challenge infection. All immunizations and infections were performed under anesthesia. These animal experiments were conducted in strict compliance with animal husbandry and welfare regulations in handled in biosafety level two animal facilities according to the guidelines of the Animal Care and Use Committee of the National Institute of Infectious Diseases, and were approved by this Committee.

2-2-3-2 Evaluation of antibody responses

Hemagglutinin (HA)-specific IgG and IgA antibodies in serum or nasal wash samples were quantified by enzyme-linked immunosorbent assay (ELISA). Recombinant trimeric HA, produced by the method of Stevens et al.,[51] was used as the coating antigen. HA-specific IgA antibodies were detected using biotin-conjugated goat anti-mouse IgA antibodies (Kirkegaard & Perry Laboratories, USA) and alkaline phosphatase-conjugated streptavidin (Thermo Fisher Scientific, USA). The detection reaction was initiated by the addition of p-nitrophenylphosphate (Sigma- Aldrich, USA) in 10 mM diethanolamine (pH: 9.8) containing 0.5 mM $MgCl_2$. Absorbance at 405 nm was measured using an iMark Microplate Reader (BIO-RAD, Hercules, USA). Pooled nasal wash samples collected from hyperimmune mice was used as a standard for the quantification of nasal IgA. ELISA was performed using serial two-fold dilutions of standard serum and nasal wash (NW) (from 1 : 100 and 1 : 1, respectively) as described above. The reciprocal of highest dilution rate of sample showing positive reaction was defined as ELISA unit. The threshold value for positive reaction was defined as mean $\pm$3SD of serially diluted serum or NW samples collected from a non-vaccinated BALB/c mouse.

2-2-3-3 Measurement of virus titer

Virus titers in the nasal wash specimens were measured according to a previously described method.[52] Briefly, 200 mL aliquots of serial 10-fold dilutions of the nasal wash were inoculated into Madin–Darby canine kidney (MDCK) cells in a six-well plate. After allowing the plates to incubate for 1 h, each well was overlaid with 2 mL of agar medium. The number of plaques was counted following crystal violet staining at 2 days after inoculation.

2-2-3-4 Preparation of nasal tissue for TEM observation

Sphere40-PICs or Rod40-PICs containing 2.0 nM AuNPs and 1.0 mg/mL uPIC(40:400) in 10 μL were administrated intranasally to mice. The mice were sacrificed by exposure to excess isoflurane and exsanguinated (via the heart) 6 h after inoculation. After perfusion fixation, the heads of the mice were harvested and immersed in a formalin solution for 2 or 3 days. After fixation, the tissues were decalcified in a buffered EDTA 2Na solution for several days in a refrigerator. After decalcification, heads were transferred into 0.1 M phosphate buffer (PB) (pH: 7.4) containing 2.5% glutaraldehyde (TAAB Laboratories Equipment Ltd, UK).

Nasal tissues were sliced and postfixed with an aqueous solution of 1 w/w% OsO_4 and 1.5 w/w% $K_3[Fe(CN)_6]$ at room temperature for 2 hours. The fixed tissues were washed with PB three times, then dehydrated by sequential soaking in 50, 70, 90, 95 and 100% ethanol. The half volume of the soaking solution was gradually replaced by propylene oxide. Finally, the half volume of the solution was replaced by epoxy resin. After mixing, the tissues in the propylene oxide/epoxy resin were incubated at 4 °C for 1 hour. This resin-replacement procedure was repeated four times and the tissues were incubated in epoxy resin at 4 °C overnight. As epoxy resin, we used the mixture of epon812, DDSA, MNA and DMP-30 (TAAB, England) at a volume ratio of 23:13:14:1. After de-gassing under a vacuum, tissues were embedded in epoxy resin in a mold and the resin was cured by incubation at 37°C for 1 day and 60°C for 3 days. Ultrathin sections were then cut on a Leica Ultramicrotome. The sections were stained with uranyl acetate followed by lead citrate and examined at 80 kV with a JEM transmission electron microscope (JEOL, Japan).

2-2-4 Evaluation of cytotoxicity and cytokine productions

2-2-4-1 Evaluation of AuNP-PIC uptake by macrophage cell line

RAW264.7 cells were cultured in DMEM supplemented with 10% FBS, 100 U/mL penicillin, 100 μg/mL streptomycin at 37°C in 5 % CO_2. RAW 264.7 cells were seeded 1.0 × 10^5 cells per well in a 6-well plate and incubated. After 24 hours, DMEM was removed and fresh DMEM containing AuNP-PICs (0.4 nM AuNPs and 10 μg/mL uPIC(40:400) at final concentration) were added then incubated for 24 hours. Then, medium was removed and cells were washed with 3 mL of PBS(-) three times and fresh DMEM was added. Cells were collected and centrifugated. The pellet of cells was treated with 1 mL of aqua regia and gold nanoparticles containing cells were completely decomposed by incubation at 80°C for 10 hours. The resultant solution was diluted with 9 mL water and filtrated to quantify Au atom by inductively coupled plasma optical emission spectroscopy.

2-2-4-2 Preparation of murine bone marrow derived dendritic cells

Murine bone marrow-derived dendritic cells (BMDCs) were prepared according to a previously reported method.[53] BMDCs were generated from C3H/HeNJcl (female, 6 weeks old) mice. In brief, bone marrow cells were collected from the femur and tibia. Culture medium containing 2×10^6 cells in 10 mL were seeded to TC-treated 100 mm dishes. Cells were cultured in RPMI-1640 supplemented with 10% FBS, 100 U/mL penicillin, 100 μg/mL streptomycin, 25 mM HEPES-KOH (pH: 7.4), 50 μM 2-mercaptethanol and 10 ng/mL GM-CSF for 11 days. Ten mL of culture medium was added on day 3, and one half of the medium was changed for fresh medium on day 6, 8 and 10. After cultivation, floating cells were collected. These animal procedures were performed in accordance with the Guidelines for Care and Use of Laboratory Animals of Hokkaido University and approved by the Animal Ethics Committee of Hokkaido University.

Obtained BMDCs were analyzed by flow cytometer. BMDCs were suspended to 7.5 mL

of PBS(-) containing 5% FBS to be 10^6 cells/mL. To this suspension, 4 μg of rat anti-mouse CD16/32 antibody was added and incubated at room temperature for 30 min to block Fc receptor. Subsequently, 0.9 μg of PE conjugated anti-mouse CD11c was added and incubated at room temperature for a 1 hour in the dark. PE conjugated American hamster IgG isotype was used instead of anti-CD11c antibody for the isotype control. After incubation, excess antibodies were removed by twice centrifugation and cells were suspended in PBS(-) to analyze by flow cytometer.

2-2-4-3 Evaluation of cytotoxicity and cytokine production from BMDC

For the evaluation of IL-1β production, the collected BMDCs were primed with 50 ng/mL LPS for 3 h, and then used without purification. BMDCs were mixed with the adjuvant in RPMI-1640 supplemented with 10% FBS, 100 U/mL penicillin, 100 mg/mL streptomycin, 25 mM HEPES-KOH (pH: 7.4) and 50 mM 2-mercaptoethanol. The BMDCs were adjuvants. After incubation for 24 h, culture supernatants were then seeded at 1.0×10^5 cells per well in a 96-well plate with collected to measure cytokine concentration and cells were washed twice with culture medium supplemented with 10% FBS, 100 U/mL penicillin, 100 mg/mL streptomycin and 25 mM HEPES-KOH. Cellular viabilities were evaluated using a Cell Counting Kit-8 (CCK-8). After incubation with CCK-8, the absorbance at 450 nm was measured using a microplate reader (infinite 200 PRO, Tecan, Switzerland). The concentrations of IL-1β, IFN-β and TNF-a in the culture supernatant were deter- mined by ELISA following the manufacturer's protocols.

2-3 Results and Discussion

2-3-1 Preparation of gold nanoparticle and RNA conjugates

Spherical and rod-shaped gold nanoparticles were synthesized via conventional seeding growth methods.[44,54] Synthesized cetyltrimethylammonium (CTA)-stabilized AuNPs were functionalized with (16-mercaptohexadecyl)trimethylammonium bromide (MTAB) as MTAB functionalization provides a cationic surface with lower cytotoxicity compared to CTA-stabilized AuNPs due to the removal of excess surfactant.[43] The average size of the MTAB-functionalized AuNPs (MTAB-AuNPs) was determined from transmission electron microscope (TEM) images by counting at least 100 particles (Figure 2-8). The mean diameters of the spherical AuNPs were 20 ± 0.9 and 41 ± 2.2 nm. The mean lengths and diameters of the rod-shaped AuNPs were 28 ± 3.2 × 7.9 ± 0.9 and 41 ± 4.8 × 12 ± 1.6 (core size in Table 2-2). Here, these MTAB-functionalized spherical AuNPs are referred to as Sphere20 and Sphere40, and the MTAB-functionalized rod-shaped AuNPs are referred to as Rod30 and Rod40 in accordance with their shape and size.

MTAB-AuNPs were added to uPIC(40:400) solutions, affording the AuNP-uPIC(40:400) complexes (referred to as Sphere20-PIC, Sphere40-PIC, Rod30-PIC and Rod40-PIC, respectively). To standardize the uPIC(40:400) dose, the resultant AuNP-PICs were used without purification. Conjugation of uPIC(40:400) onto the AuNPs was confirmed by changes in zeta-potentials from positive (39 ~ 64 mV) to negative (-47 ~ -53 mV). For example, the zeta potential of Sphere20 was changed from 39 mV to -53 mV after addition to the uPIC(40:400) solution (Table 2-2). The colloidal dispersibilitiy in solution of the various AuNP-PICs was examined by extinction spectra. The extinction spectra of the AuNPs did not change after mixing with uPIC(40:400) in water (Figure 2-9), indicating that the AuNPs did not aggregate after coating with uPIC(40:400) molecules. The number of immobilized uPIC(40:400) molecules on a single AuNP was quantified from the concentration of unbound uPIC(40:400) in the supernatant after centrifugation. The average

number of uPIC(40:400) molecules attached on a single particle ranged from 5.2 to 20 molecules (Table 2-2). For the vaccination, the AuNP-PICs were mixed with hemagglutinin. We, therefore, investigated whether HA was attached onto the AuNP-PICs using dynamic light scattering (DLS). The hydrodynamic diameter of the AuNP-PICs after mixing with HA did not change (Figure 2-10), whereas positively charged MTAB-AuNPs showed a large shift in the DLS peak after mixing with HA (Figure 2-11). This difference suggests that the interaction of HA with the AuNP-PICs is so weak that it can be ignored and that the AuNP-PICs do not work as a delivery carrier of antigen HA. For the in vitro study, the AuNP-PICs were applied to the culture media. Thus, we investigated their colloidal dispersibility in the culture media. All AuNP-PICs, except Rod30-PIC, showed good dispersibility in the culture media (Figure 2-12).

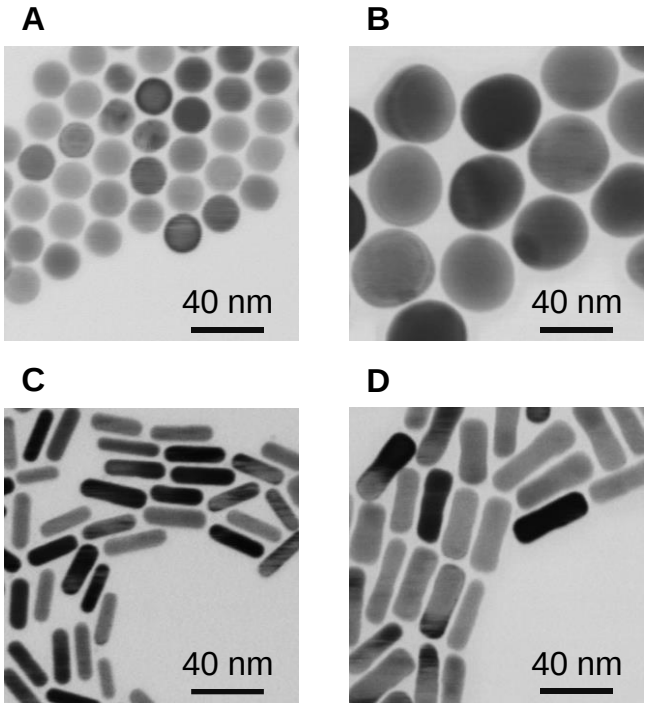

Figure 2-8 TEM images of MTAB-AuNPs (A) Sphere20, (B) Sphere40, (C) Rod30 and (D) Rod40.

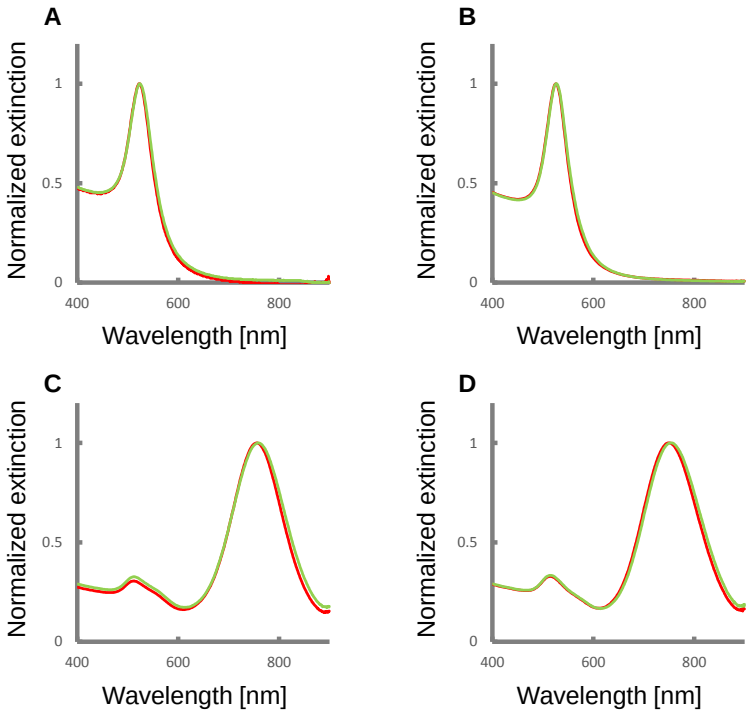

Figure 2-9 Extinction spectra of MTAB-AuNPs (red) and AuNP-PICs (green) in MilliQ water. Maximum extinction was normalized as 1. (A) Sphere20s, (B) Sphere40s, (C) Rod30s and (D) Rod40s.

Table 2-2 Physicochemical properties of the AuNP-PICs (means ± SD)

	Size of core [nm] [a)]	Zeta potential [mV] [b)]	Surface area of core [nm^2]	Number of uPIC(40:400) / particle [b)]
Sphere20-PIC	20 ± 0.9	-53 ± 6.7	1300	5.2 ± 0.2
Sphere40-PIC	41 ± 2.2	-48 ± 4.8	5000	12 ± 0.1
Rod30-PIC	28 ± 3.2 × 7.9 ± 0.9	-47 ± 5.3	770	20 ± 1.1
Rod40-PIC	41 ± 4.8 × 12 ± 1.6	-49 ± 2.1	1800	10 ± 1.0

a) Nanoparticle sizes were determined from at least 100 particles in TEM images; b) Zeta potentials of the AuNP-PICs and the number of immobilized uPIC(40:400) molecules were determined from at least 3 independent experiments.

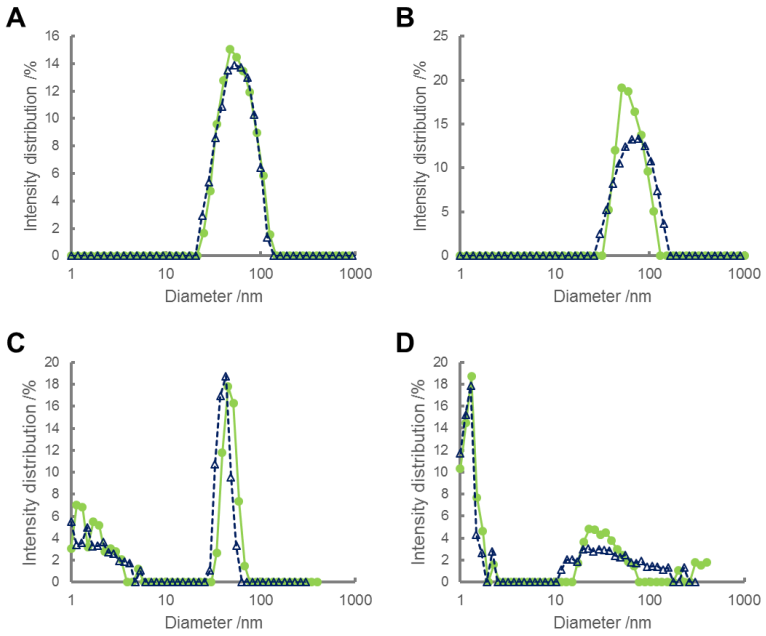

Figure 2-10 Size distribution of (A) Sphere20-PICs, (B) Sphere40-PICs, (C) Rod30-PICs and (D) Rod40-PICs determined from DLS. Green and blue plots indicate AuNP-PICs and AuNP-PICs mixed with HA, respectively. Final concentration: [AuNP] = 0.4 nM, [uPIC(40:400)] = 10 μ/mL, [HA] = 1 μg/mL.

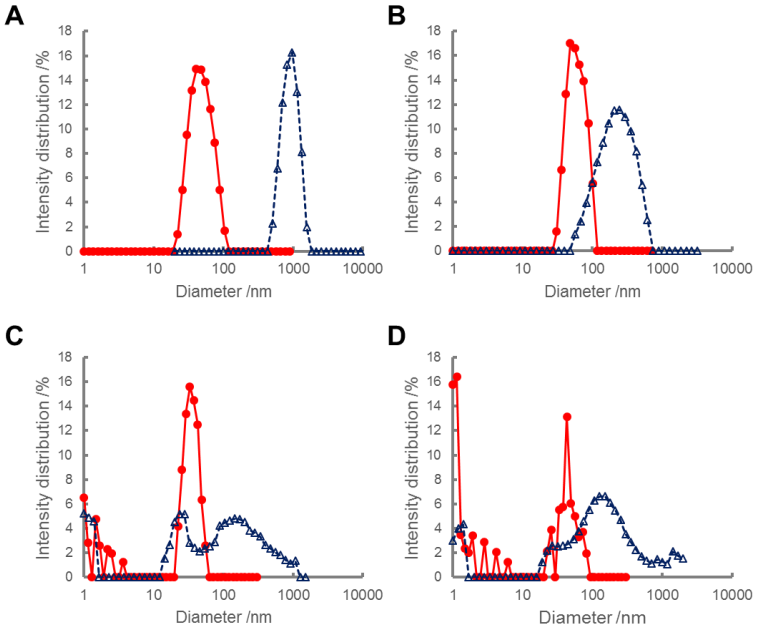

Figure 2-11 Size distribution of (A) Sphere20s, (B) Sphere40s, (C) Rod30s and (D) Rod40s determined from DLS. Red and blue plots indicate MTAB-functionalized AuNPs and AuNPs mixed with HA, respectively. Final concentration: [AuNP] = 0.4 nM, [HA] = 1 μg/mL.

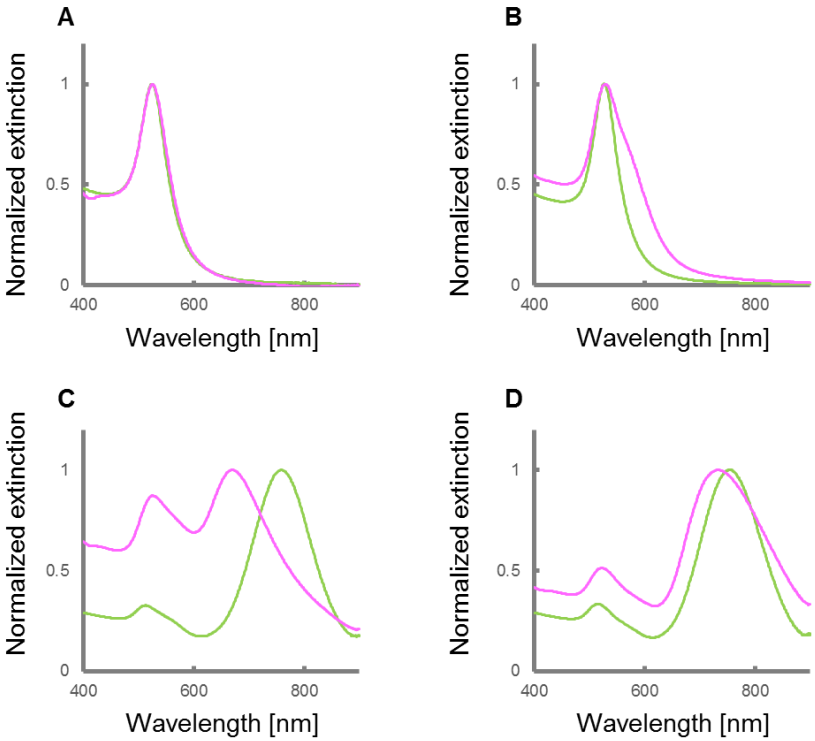

Figure 2-12 Extinction spectra of AuNP-PICs in MilliQ water (green) and in culture medium (pink). Maximum extinction was normalized as 1. (A) Sphere20-PICs, (B) Sphere40-PICs, (C) Rod30-PICs and (D) Rod40-PICs.

2-3-2 Evaluation of conjugates adjuvanticity

The AuNP–PICs were administrated subcutaneously or intranasally to mice twice at a 3-week interval with an inactivated split influenza vaccine containing partially purified influenza HA antigens obtained by disruption of influenza virus virions by treatment with ether solvent. Two weeks after the second vaccination, mice were challenged with influenza A virus (A/NRT). The nasal wash and serum samples were then collected at 3 days post-infection to evaluate virus titers, and systemic and mucosal antibody responses in mice. For vaccination, AuNP conjugations with a total of 10 or 1.0 μg (corresponding to ca. 40 and 4 pmol, respectively) of uPIC(40:400)/head were administrated as the adjuvant. The AuNP–PIC solutions were finally administrated soon after mixing with an aqueous solution containing 100 or 10 ng of HA antigens.

First, IgG antibody responses was evaluated in mice immunized with 100 ng of HA subcutaneously, as this is commonly used to assess vaccine-induced immune response. Commercially available poly(I:C) was used as a positive control. No significant difference was observed between the AuNP–PIC groups and uPIC(40:400). On the other hand, in comparison with the negative control (top bar in Figure 2-13A Left), all AuNP‑PIC groups showed significant responses, whereas uPIC(40:400) and poly(I:C) did not (Figure 2-13A Left). Although uPIC(40:400), the AuNP–PICs and poly(I:C) seemed to show similar IgG responses, a trend toward higher IgG responses in the AuNP–PIC groups were observed.

The adjuvanticity of the AuNP-PICs for the intranasal vaccine was then evaluated. Before intranasal immunization, Sphere40-PIC and Rod40-PIC uptake in the nasal epithelium was observed. Figure 2-14 showed TEM images of tissue sections of the nasal epithelium after intranasal immunization. Both Sphere40-PICs and Rod40-PICs were found among the cilia and in the cellular vesicles in the nasal epithelium, indicating that, regardless of the shape of the AuNPs, AuNP-PICs can reach the cells located in the nasal epithelium via intranasal immunization, although their efficiencies remain unclear. Then, intranasal immunization

was conducted using the same dose as the subcutaneous immunization to evaluate systemic IgG and mucosal IgA responses. Unlike the subcutaneous immunization, uPIC(40:400) itself showed a significant adjuvant effect on IgG antibody response. Significant IgG antibody responses were also confirmed for all AuNP-PIC groups (Figure 13A center). With regard to the IgA response to the intranasal immunization, all uPIC(40:400), poly(I:C) and AuNP-PIC groups showed significant responses, except for Sphere40-PIC, in comparison to the response induced by HA alone (Figure 13A right). Thus, for the intranasal immunization using 100 ng HA antigens, we concluded that all AuNP-PIC groups except for Sphere40-PIC showed the same level of adjuvanticity as uPIC(40:400) and poly(I:C). Interestingly, Sphere40-PICs demonstrated a negative effect when used for intranasal immunization, despite the positive effect observed for subcutaneous vaccination. This indicates that the shape and size of the adjuvant scaffold should be optimized according to the vaccine administration route.

To protect from influenza virus infection, mucosal IgA antibody against the virus is particularly crucial. In one set of experiments (n = 5-6) on intranasal immunization, I also checked the virus titers as well as antibody responses, which correspond to the virus levels remaining in the nasal wash after challenge infection. The groups showing higher mucosal IgA antibody responses tended to show lower virus titers (Figure 13B). This good correlation between mucosal IgA antibody responses and virus titers indicates that the induced IgA antibodies play a principal role in protecting against viral infection.

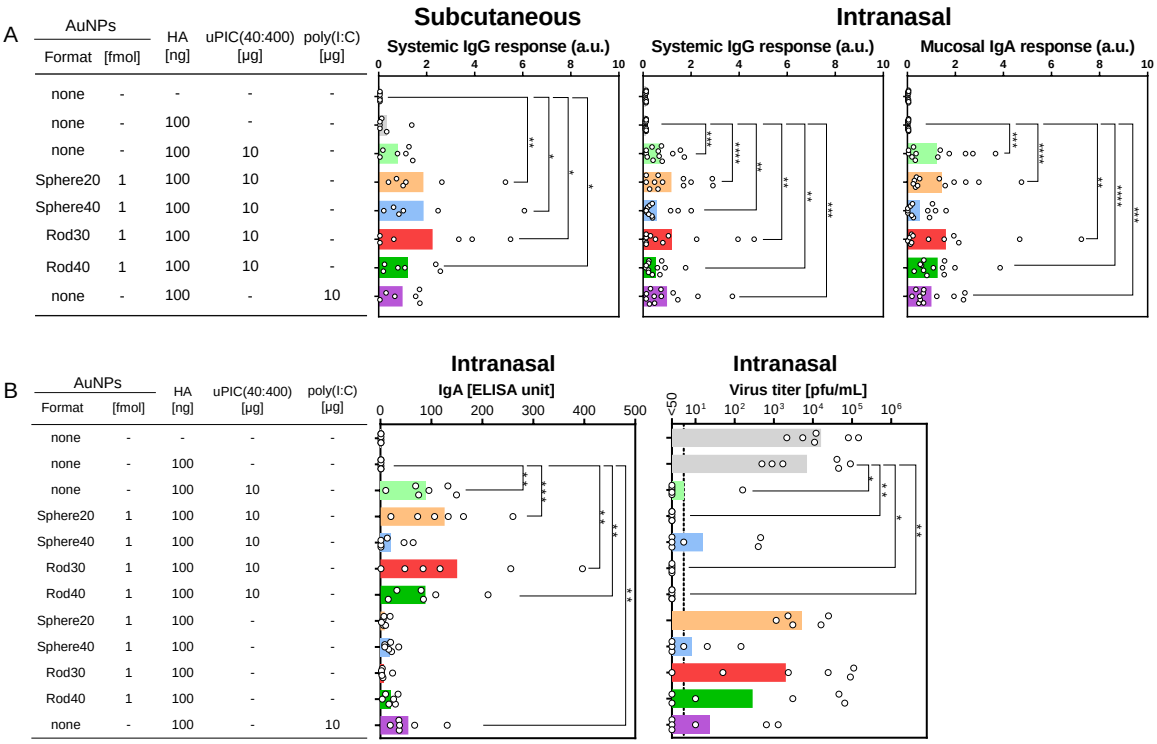

Figure 2-13 (A) Antibody production in mice immunized with 100 ng of antigen HA (X-179A ether-split vaccine) combined with adjuvants subcutaneously (SC; left) or intranasally (IN; Center, right). For the IN immunization, two independent experiments were carried out (n = 5-6 in each experiment). Data were normalized against the poly(I:C) group. These normalized values were shown as arbitrary units (a.u.). Regarding the intranasal immunization shown Figure 2-13A, two independent experiments were carried out. Average values of antibody responses were obtained from normalized data against the poly(I:C) group in each experiment. (B) Negative correlations between HA-specific IgA antibodies and viral loads in nasal wash samples. Each circle represents an individual titer, and each bar represents the mean of IgA ELISA units and the GMT of the virus titers. The dotted line indicates 50 pfu/mL of virus titer, which was the detection limit. Statistical analysis was performed using Kruskal-Wallis tests with Dann's multiple comparison tests. The asterisks *, **, *** and **** indicate $p < 0.05$, $p < 0.01$, $p < 0.001$ and $p < 0.0001$, respectively.

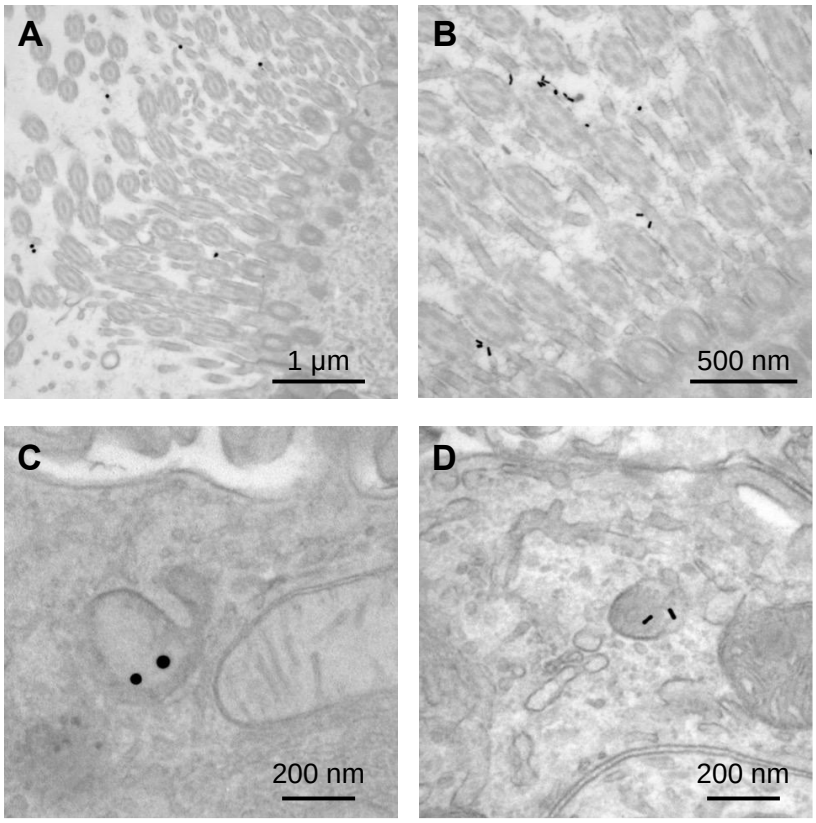

Figure 2-14 TEM images of nasal epithelial tissue from mice administrated Sphere40-PICs (A, C) or Rod40-PICs (B, D) intranasally.

For intranasal vaccination, the administration of a high dose (100 ng HA) suppressed the virus titer too efficiently as shown in Figure 12B to evaluate differences in adjuvanticity among the AuNP-PICs. Thus, the administration level of HA was reduced to 10 ng to allow better evaluation of adjuvanticity using virus titers. When Rod30-PICs and Rod40-PICs with 10 ng of HA antigen were used, significantly higher adjuvanticity was observed in comparison to uPIC(40:400), while Sphere40-PICs did not show significant adjuvanticity (Figure 2-15 left). As a control, Rod30 and Rod40 without uPIC(40:400) did not induce any reduction in the viral titer (Figure 2-15 left), indicating that the gold nanorods themselves did not demonstrate any adjuvanticity under these conditions. Figure 2-15 shows that the lower doses (12 ng AuNPs) of Rod30-PIC and Rod40-PIC are more effective in reducing the viral titer than the higher doses (120 ng AuNPs). Although the reason for this is unclear, we assume that there might be an optimal amount of adjuvant for the induction of effective immune responses. The protection from viral infection with a lower adjuvant dose is preferable as it minimizes the risk of adverse reactions. On the other hand, no significant differences between Sphere20-PICs or Sphere40-PICs and uPIC(40:400) alone were observed when 10 ng of HA antigen was used (Figure 2-15 right). These results clearly show that uPIC(40:400) adjuvanticity was enhanced by conjugation with Rod30s and Rod40s rather than with Sphere20s or Sphere40s at a lower range of HA doses, thereby demonstrating a shape-related effect on intranasal vaccination.

These in vivo studies newly demonstrate two points: (1) the shape-related effect of the adjuvant scaffold is dependent on the administration route, and (2) rod-shaped nanoparticles are effective as a scaffold for RNA adjuvants for intranasal vaccines at low antigen doses.

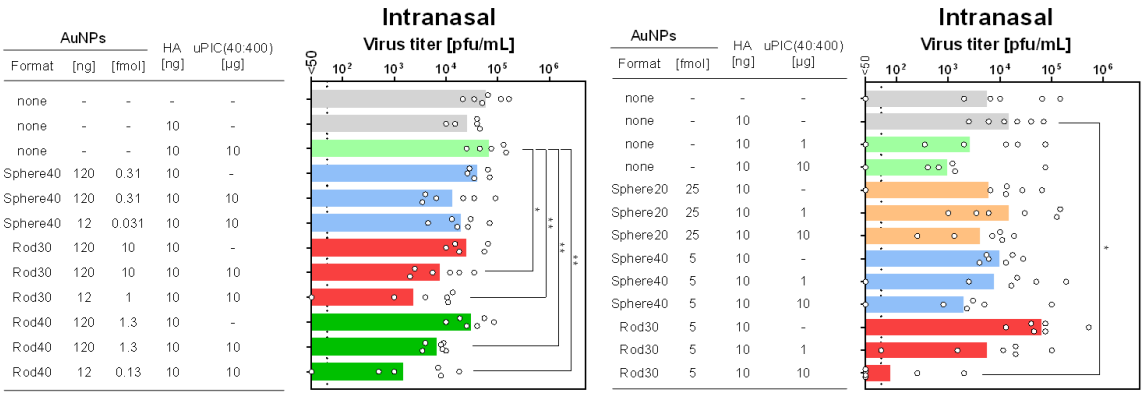

Figure 2-15 The reduction of viral loads in nasal wash samples from mice immunized intranasally with 10 ng of HA. Each circle and bar represent the individual titer and geometric mean titer, respectively. The dotted line indicates 50 pfu/mL of virus titer which is the detection limit. Statistical analysis was performed using Kruskal-Wallis tests with Dann's multiple comparison tests. The asterisks *and ** indicate $p < 0.05$ and $p < 0.01$, respectively.

2-3-3 Evaluation of cytotoxicity and cytokine production

2-3-3-1 Evaluation of AuNP-PIC uptake by macrophage cell line

AuNP-PICs have anionic surface and taken up *via* phagocytosis or scavenger receptor mediated endocytosis.[55–57] The number of AuNP uptake per cell was shown as Figure 2-16. Both spherical and rod-shaped AuNP-PICs with smaller size were take up more amount. This result did not have positive correlation with their adjuvanticity. Because Rod30-PIC tended to aggregate in medium than Rod40-PIC, it was considered that Rod30-PIC was taken up by the influence of gravity.

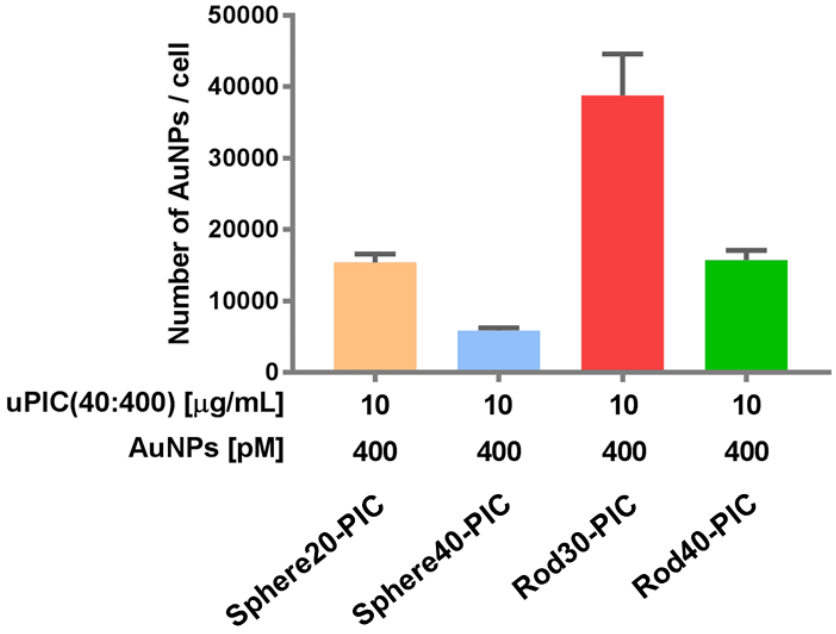

Figure 2-16 Cellular uptake of auNP-PICs by RAW264.7 cell determined by ICP-AES.

2-3-3-2 Preparation of murine bone marrow derived dendritic cell

CD11c antigen is common dendritic cell marked and expressed on cellular membrane surface. Here, the expression of CD11c was examined to determine whether obtained cells were dendritic cells. CD11c was stained with PE-conjugated antibody and analyzed with FACS. The fluorescence intensity derived from stained CD11c was clearly higher than isotype control group, so that it was confirmed that the obtained cells expressed CD11c. (Figure 2-17) The following cell study was conducted using these BMDC.

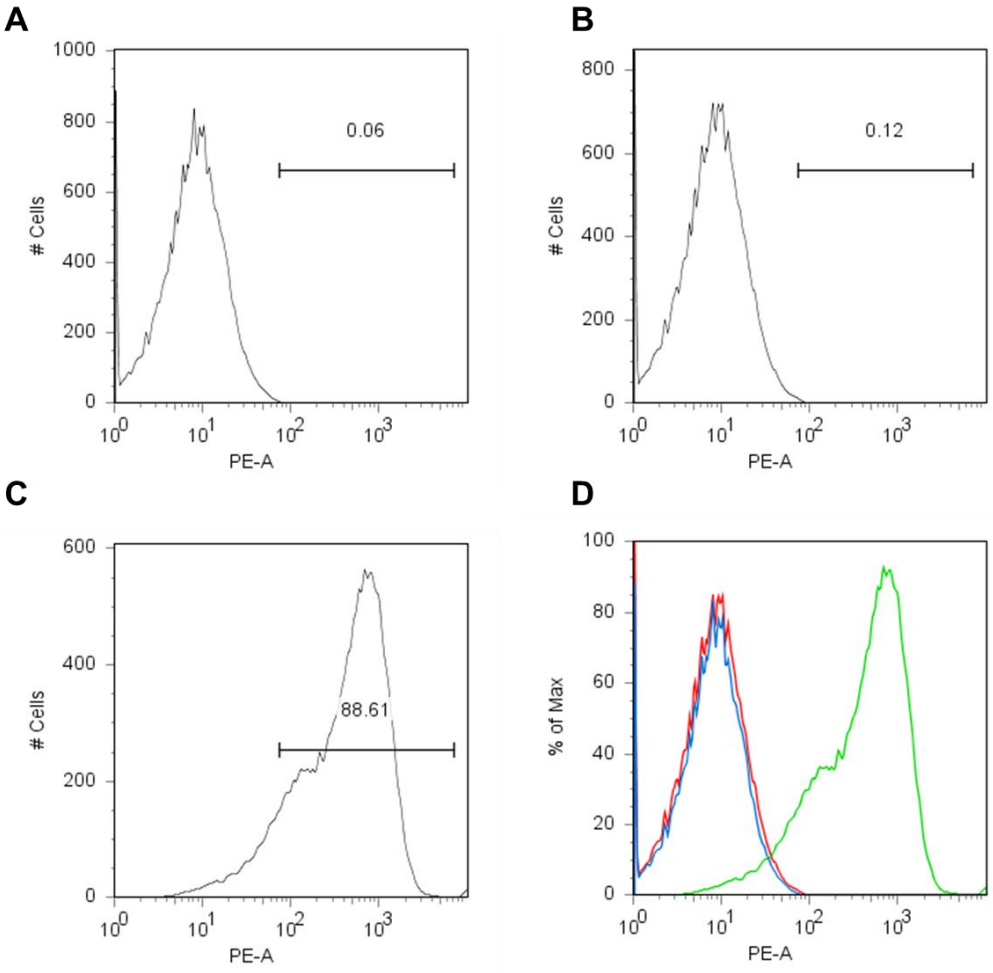

Figure 2-17 FACS histogram for expression of CD11c on BMDC. (A) no stained, (B) isotype control, (C) anti-CD11c and (D) overlay (blue: no stained, red: isotype control and green: anti-CD11c).

2-3-3-3 Evaluation of cytotoxicity and cytokine production

Cytokines are a key mediator in the induction of immune responses. However, excess cytokine production can cause various adverse effects.[58–60] When attempting to enhance the adjuvanticity of uPIC(40:400), it is important to avoid excess cytokine production which can lead to toxicity.[61] Further, it was expected that the information obtained on cytokine production could provide some sights into mechanisms associated with in vivo adjuvanticity. Thus, cellular viability and the production of three cytokines; IL-1β, IFN-β and TNF-α were evaluated. Commercially available poly(I:C) and Alum, a TLR3 agonist and an inflammasome activator, respectively, were used as positive controls.

First, I checked cellular viability using a Cell Counting Kit-8 (CCK-8) after incubation with AuNP-PICs for 24 h. When BMDCs were stimulated with 10 μg/mL of poly(I:C), a significant reduction in viability, which was comparable to that induced by 200 μg/mL of Alum, was observed. On stimulation by the AuNP-PIC groups, BMDC viabilities were maintained compared to the uPIC(40:400) group (Figure 2-18), supporting the notion that the AuNP-PICs did not cause cellular damage *in vitro*.

IL-1β is a major mediator of the innate immune system and inflammation.[62] Various particles are known to induce IL-1β production, such as amino-functionalized nanoparticles[15], rod-shaped particles with a high aspect ratio[63,64] and larger-sized particles.[65] In our experiment, increased IL-1β production was induced by Sphere40-PICs, but not by Sphere20-PICs, Rod30-PICs or Rod40-PICs (Figure 2-18B). This result indicates the Rod30-PICs and Rod40-PICs did not cause lysosomal rupture. We assumed that Sphere40-PICs induced the highest level of IL-1β production as Sphere40-PICs have the largest volume among the tested particles, thereby causing some damage to the lysosome.

IFNs and pro-inflammatory cytokines are secreted upon stimulation by dsRNAs.[4] The level of IFN-β production was somewhat increased by the conjugation of uPIC(40:400)

with Sphere40s, and slightly increased by that with Rod30s (Figure 2-18C). Rod30-PICs at the highest AuNP concentration tended to aggregate in the medium (Figure 2-12). This aggregation may affect IFN-β production through particle size enlargement. Interestingly, when compared to poly(I:C), uPIC(40:400) and AuNP-PICs induced little IFN-β production. This suggests that the AuNP-PICs may elicit the immune responses through a pathway that is not dependent on TLR3, in other words, the conjugation of uPIC to AuNPs may affect the immune routes. Further, Sphere40-PICs with 200 and 400 pM of AuNPs induced higher levels of IFN-β production than did uPIC(40:400). As Sphere40-PICs showed higher IL-1β induction, which can be caused by lysosomal rupture, Sphere40-PICs may induce IFN-β production through activation of RIG-I-like receptors[4] in the cytoplasm. We next checked the production of TNF-α, a representative pro-inflammatory cytokine that plays a role in host defense against infection. Treatment with uPIC(40:400) alone, Rod30-PICs and Rod40-PICs induced almost no enhancement of TNF-α production, whereas slight levels of TNF-α were induced by incubation with Sphere20-PICs and Sphere40-PICs (Figure 2-18D). Additionally, as antigen immunogenicity has been reported to be enhanced by conjugation with nanoparticles,[36] we tested whether the HA antigen affects cytokine production when stimulated with AuNP-PICs. No changes in IFN-β or TNF-α production were observed for the AuNP-PIC groups in the presence of HA antigen, indicating that the induction of cytokine production by the AuNP-PICs was not influenced by the presence of HA antigens (Figure 2-19).

In the *in vitro* experiments, Rod30-PICs and Rod40-PICs induced low levels of cytokine production while Sphere40-PICs tended to induce inflammatory cytokine production. Since this tendency does not correlate with adjuvanticity observed for in vivo vaccination, we cannot identify the detailed mechanism based only on the cytokine production. Importantly, however, the low levels of inflammatory cytokine induction by Rod30-PICs and Rod40-PICs are helpful in avoiding the adverse reactions originating from excess cytokine

production. Therefore, the rod-shaped gold nanoparticle/uPIC(40:400) complexes appear to be good potential adjuvants for the development of intranasal inactivated influenza vaccines with fewer side effects.

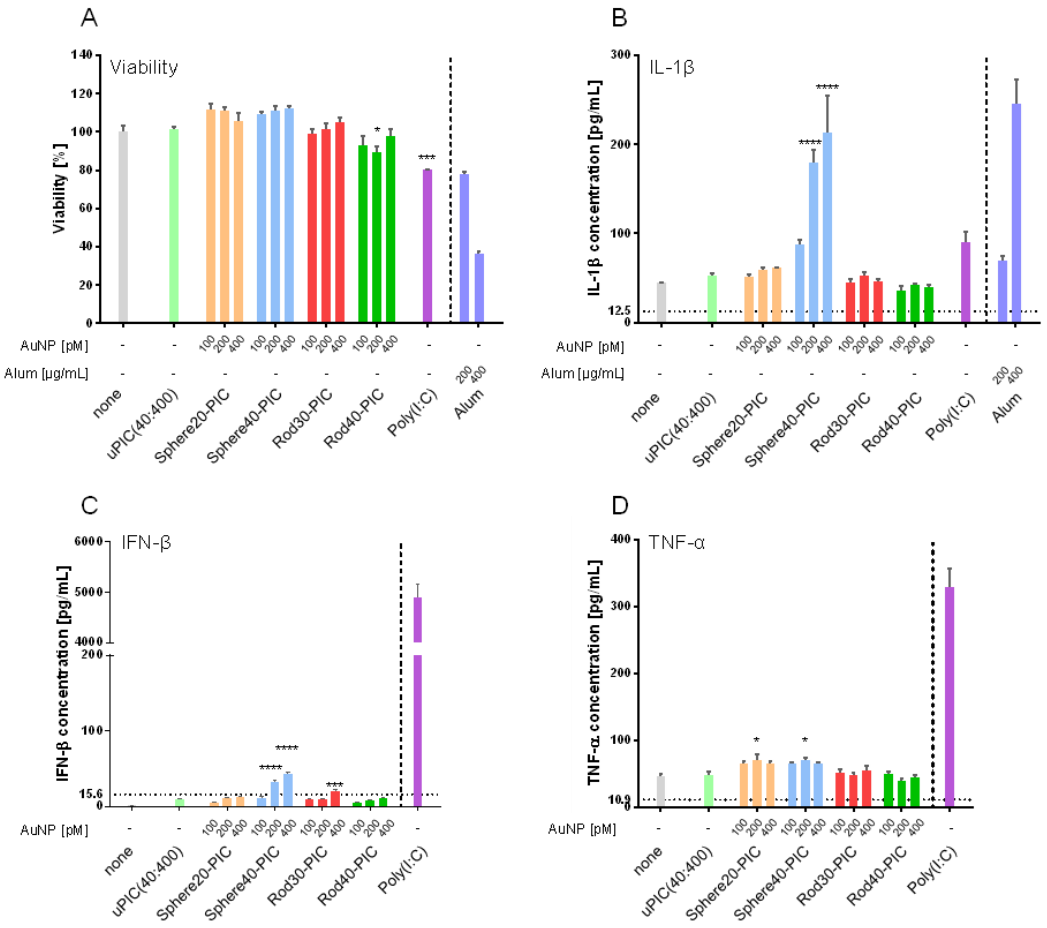

Figure 2-18 (A) Cellular viability of BMDCs treated with AuNP-PICs containing 10 μg/mL of uPIC(40:400) final concentration for 24 h at 37°C (means ± SEM, n = 3). (B) IL-1β, (C) IFN-β and (D) TNF-α production from BMDCs treated with AuNP-PICs for 24 h at 37°C. For the evaluation of IL-1β production, BMDCs were primed with 50 ng/mL of LPS for 3 h. Alum and poly(I:C) were used as positive controls. The detection limit is indicated by the horizontal dotted line. Statistical analysis was performed against uPIC(40:400)-treated BMDC groups using one-way ANOVA tests with Dunnett's multiple comparison tests. Positive controls (right side of the vertical dotted line) were excluded from the statistical analysis. The asterisks *, **, *** and **** indicate $p < 0.05$, $p < 0.01$, $p < 0.001$ and $p \leq 0.0001$, respectively.

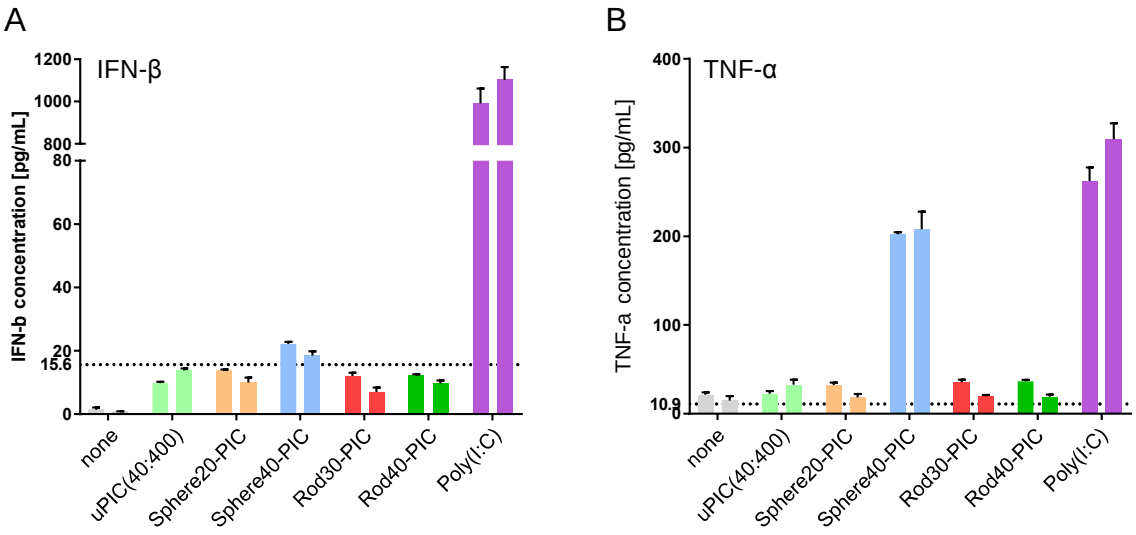

Figure 2-19 The effects of antigens on (A) IFN-β and (B) TNF-α production. BMDCs were stimulated by AuNP-PICs with (Right bar) or without (Left bar) HA. Final concentrations of uPIC(40:400), AuNPs and HA were 100 μg/mL, 100 pM and 1.0 μg/mL, respectively. The detection limit is indicated by the horizontal dotted line.

2-4 Conclusion

In summary, we investigated the influence on adjuvanticity of the shape and size of AuNPs as scaffolds for the immobilization of uPIC(40:400) through a comparison of intranasal and subcutaneous administration. For the subcutaneous vaccination, IgG antibody responses were slightly enhanced by conjugation with AuNPs, and the effect of the AuNP shape on the systemic IgG responses was limited for all tested AuNP-PICs. On the other hand, for the intranasal vaccination at a lower HA dose, Rod30-PICs and Rod40-PICs clearly suppressed viral infection while Sphere20-PICs and Sphere40-PICs did not. In in vitro experiments, Rod30-PICs and Rod40-PICs did not increase inflammatory cytokine production, which is known to be a potential cause of adverse reactions. From these results, we concluded that the shape-related effect of AuNPs is dependent on the immunization route, and gold nanorods afford an effective adjuvant scaffold for uPIC(40:400) as an intranasal influenza vaccine. These findings indicate that utilizing shape- controlled nanoparticles as scaffolds for adjuvant molecules is a good approach to enhance weak adjuvanticity without resulting in excessive inflammatory responses. In other words, the appropriate choice of nanomaterial shape could be crucial to the design of safe and effective intranasal inactivated vaccines. More comprehensive studies of nanoparticles are expected to reveal further applications.

2-5 References

(1) Asanuma, H.; Ohori, J.; McGhee, J.; Fujihashi, K. Past Efforts and Future Prospects for a Nasal Influenza Vaccine. *Clin. Immunol. Endocr. Metab. Drugs* **2015**, *2* (1), 13–26.

(2) Sano, K.; Ainai, A.; Suzuki, T.; Hasegawa, H. The Road to a More Effective Influenza Vaccine: Up to Date Studies and Future Prospects. *Vaccine* **2017**, *35* (40), 5388–5395.

(3) Ichinohe, T.; Watanabe, I.; Ito, S.; Fujii, H.; Moriyama, M.; Tamura, S.; Takahashi, H.; Sawa, H.; Chiba, J.; Kurata, T.; et al. Synthetic Double-Stranded RNA Poly (I : C) Combined with Mucosal Vaccine Protects against Influenza Virus Infection. *J. Virol.* **2005**, *79* (5), 2910–2919.

(4) Desmet, C. J.; Ishii, K. J. Nucleic Acid Sensing at the Interface between Innate and Adaptive Immunity in Vaccination. *Nat. Rev. Immunol.* **2012**, *12* (7), 479–491.

(5) Liu, L.; Botos, I.; Wang, Y.; Leonard, J. N.; Shiloach, J.; Segal, D. M.; Davies, D. R. Structural Basis of Toll-Like Receptor 3 Signaling with Double-Stranded RNA. *Science (80-.).* **2008**, *320* (5874), 379–381.

(6) Leonard, J. N.; Ghirlando, R.; Askins, J.; Bell, J. K.; Margulies, D. H.; Davies, D. R.; Segal, D. M. The TLR3 Signaling Complex Forms by Cooperative Receptor Dimerization. *Proc. Natl. Acad. Sci. U. S. A.* **2008**, *105* (1), 258–263.

(7) Machida, H.; Kuninaka, A.; Yoshino, H. Relationship between the Molecular Size of Poly I·Poly C and Its Biological Activity1. *Jpn. J. Microbiol.* **1976**, *20* (2), 71–76.

(8) Kanaya, K.; Kondo, K.; Suzukawa, K.; Sakamoto, T.; Kikuta, S.; Okada, K.; Yamasoba, T. Innate Immune Responses and Neuroepithelial Degeneration and Regeneration in the Mouse Olfactory Mucosa Induced by Intranasal Administration of Poly(I:C). *Cell Tissue Res.* **2014**, *357* (1), 279–299.

(9) Nakano, T.; Yamamura, E.-T.; Fujita, H.; Sone, T.; Asano, K. Novel Methods for Nucleotide Length Control in Double-Stranded Polyinosinic-Polycytidylic Acid Production Using Uneven Length Components. *Biosci. Biotechnol. Biochem.* **2018**, *82* (11), 1889–1901.

(10) Giljohann, D. A.; Seferos, D. S.; Prigodich, A. E.; Patel, P. C.; Mirkin, C. A. Gene Regulation with Polyvalent SiRNA-Nanoparticle Conjugates. *Journal of the American Chemical Society*. 2009, pp 2072–2073.

(11) Choi, C. H. J.; Hao, L.; Narayan, S. P.; Auyeung, E.; Mirkin, C. A. Mechanism for the Endocytosis of Spherical Nucleic Acid Nanoparticle Conjugates. *Proc. Natl. Acad. Sci.* **2013**, *110* (19), 7625–7630.

(12) Niikura, K.; Kobayashi, K.; Takeuchi, C.; Fujitani, N.; Takahara, S.; Ninomiya, T.; Hagiwara, K.; Mitomo, H.; Ito, Y.; Osada, Y.; et al. Amphiphilic Gold Nanoparticles Displaying Flexible Bifurcated Ligands as a Carrier for SiRNA Delivery into the Cell Cytosol. *ACS Appl. Mater. Interfaces* **2014**, *6* (24), 22146–22154.

(13) Shiosaka, S.; Kiyama, H.; Wanaka, A.; Masaya, T. A New Method for Producing a Specific and High Titre Antibody against Glutamate Using Colloidal Gold as a Carrier. *Brain Res.* **1986**, *382* (2), 399–403.

(14) Chen, Y. S.; Hung, Y. C.; Liau, I.; Huang, G. S. Assessment of the in Vivo Toxicity of Gold Nanoparticles. *Nanoscale Res. Lett.* **2009**, *4* (8), 858–864.

(15) Lunov, O.; Syrovets, T.; Loos, C.; Nienhaus, G. U.; Mailänder, V.; Landfester, K.; Rouis, M.; Simmet, T. Amino-Functionalized Polystyrene Nanoparticles Activate the NLRP3 Inflammasome in Human Macrophages. *ACS Nano* **2011**, *5* (12), 9648–9657.

(16) Zhao, L.; Seth, A.; Wibowo, N.; Zhao, C. X.; Mitter, N.; Yu, C.; Middelberg, A. P. J. Nanoparticle Vaccines. *Vaccine* **2014**, *32* (3), 327–337.

(17) Irvine, D. J.; Hanson, M. C.; Rakhra, K.; Tokatlian, T. Synthetic Nanoparticles for Vaccines and Immunotherapy. *Chem. Rev.* **2015**, *115* (19), 11109–11146.

(18) Liu, Y.; Balachandran, Y. L.; Li, D.; Shao, Y.; Jiang, X. Polyvinylpyrrolidone–Poly(Ethylene Glycol) Modified Silver Nanorods Can Be a Safe, Noncarrier Adjuvant for HIV Vaccine. *ACS Nano* **2016**, *10* (3), 3589–3596.

(19) Gause, K. T.; Wheatley, A. K.; Cui, J.; Yan, Y.; Kent, S. J.; Caruso, F. Immunological Principles Guiding the Rational Design of Particles for Vaccine Delivery. *ACS Nano*. 2017, pp 54–68.

(20) Dykman, L. A.; Khlebtsov, N. G. Immunological Properties of Gold Nanoparticles. *Chem. Sci.* **2017**, *8* (3), 1719–1735.

(21) Nochi, T.; Yuki, Y.; Takahashi, H.; Sawada, S.; Mejima, M.; Kohda, T.; Harada, N.; Kong, I. G.; Sato, A.; Kataoka, N.; et al. Nanogel Antigenic Protein-Delivery System for Adjuvant-Free Intranasal Vaccines. *Nat. Mater.* **2010**, *9* (7), 572–578.

(22) Matsuo, K.; Koizumi, H.; Akashi, M.; Nakagawa, S.; Fujita, T.; Yamamoto, A.; Okada, N. Intranasal Immunization with Poly (γ -Glutamic Acid) Nanoparticles Entrapping Antigenic Proteins Can Induce Potent Tumor Immunity. *J. Control. Release* **2011**, *152* (2), 310–316.

(23) Chithrani, B. D.; Chan, W. C. W. Elucidating the Mechanism of Cellular Uptake and Removal of Protein-Coated Gold Nanoparticles of Different Sizes and Shapes. *Nano Lett.* **2007**, *7* (6), 1542–1550.

(24) Vácha, R.; Martinez-Veracoechea, F. J.; Frenkel, D. Receptor-Mediated Endocytosis of Nanoparticles of Various Shapes. *Nano Lett.* **2011**, *11* (12), 5391–5395.

(25) Perry, J. L.; Herlihy, K. P.; Napier, M. E.; DeSimone, J. M. PRINT: A Novel Platfoem Toward Shape and Size Specific Nanoparticle Theranostics. *Acc. Chem. Res.* **2011**, *44* (10), 990–998.

(26) Albanese, A.; Tang, P. S.; Chan, W. C. W. The Effect of Nanoparticle Size, Shape, and Surface Chemistry on Biological Systems. *Annu. Rev. Biomed. Eng.* **2012**, *14*, 1–16.

(27) Nangia, S.; Sureshkumar, R. Efects of Nanoparticle Charge and Shape Anisotropy on Traslocation through Cell Membranes. *Langmuir* **2012**, *28* (51), 1766.

(28) Ying Li, Martin Kröger, W. K. L. Shape Effect in Cellular Uptake of PEGylated Nanoparticles: Comparison between Sphere, Rod, Cube and Disk. *Nanoscale* **2015**, *7*, 16631.

(29) Jiang, Y.; Huo, S.; Mizuhara, T.; Das, R.; Lee, Y.; Hou, S.; Moyano, D. F.; Duncan, B.; Liang, X.; Rotello, V. M. The Interplay of Size and Surface Functionality on the Cellular Uptake. *ACS Nano* **2015**, *9* (10), 9986–9993.

(30) Liu, Y.; Workalemahu, B.; Jiang, X. The Effects of Physicochemical Properties of Nanomaterials on Their Cellular Uptake In Vitro and In Vivo. *Small* **2017**, *13* (43), 1701815.

(31) Kinnear, C.; Moore, T. L.; Rodriguez-Lorenzo, L.; Rothen-Rutishauser, B.; Petri-Fink, A. Form Follows Function: Nanoparticle Shape and Its Implications for Nanomedicine. *Chem. Rev.* **2017**, *117* (17), 11476–11521.

(32) Uhl, C. G.; Gao, Y.; Zhou, S.; Liu, Y. The Shape Effect on Polymer Nanoparticle Transport in a Blood Vessel. *RSC Adv.* **2018**, *8* (15), 8089–8100.

(33) Mottram, P. L.; Leong, D.; Crimeen-Irwin, B.; Gloster, S.; Xiang, S. D.; Meanger, J.; Ghildyal, R.; Vardaxis, N.; Plebanski, M. Type 1 and 2 Immunity Following Vaccination Is Influenced by Nanoparticle Size: Formulation of a Model Vaccine for Respiratory Syncytial Virus. *Mol. Pharm.* **2007**, *4* (1), 73–84.

(34) Hutter, E.; Boridy, S.; Labrecque, S.; Lalancette-Hébert, M.; Kriz, J.; Winnik, F. M.; Maysinger, D. Microglial Response to Gold Nanoparticles. *ACS Nano* **2010**, *4* (5), 2595–2606.

(35) Bachmann, M. F.; Jennings, G. T. Vaccine Delivery: A Matter of Size, Geometry, Kinetics and Molecular Patterns. *Nat. Rev. Immunol.* **2010**, *10* (11), 787–796.

(36) Niikura, K.; Matsunaga, T.; Suzuki, T.; Kobayashi, S.; Yamaguchi, H.; Orba, Y.; Kawaguchi, A.; Hasegawa, H.; Kajino, K.; Ninomiya, T.; et al. Gold Nanoparticles as a Vaccine Platform: Influence of Size and Shape on Immunological Responses in Vitro and in Vivo. *ACS Nano* **2013**, *7* (5), 3926–3938.

(37) Kumar, S.; Anselmo, A. C.; Banerjee, A.; Zakrewsky, M.; Mitragotri, S. Shape and Size-Dependent Immune Response to Antigen-Carrying Nanoparticles. *J. Control. Release* **2015**, *220*, 141–148.

(38) Zhou, Q.; Zhang, Y.; Du, J.; Li, Y.; Zhou, Y.; Fu, Q.; Zhang, J.; Wang, X.; Zhan, L. Different-Sized Gold Nanoparticle Activator/Antigen Increases Dendritic Cells Accumulation in Liver-Draining Lymph Nodes and CD8+ T Cell Responses. *ACS Nano* **2016**, *10* (2), 2678–2692.

(39) Chen, X.; Yan, Y.; Müllner, M.; Ping, Y.; Cui, J.; Kempe, K.; Cortez-Jugo, C.; Caruso, F. Shape-Dependent Activation of Cytokine Secretion by Polymer Capsules in Human Monocyte-Derived Macrophages. *Biomacromolecules* **2016**, *17* (3), 1205–1212.

(40) Radovic-Moreno, A. F.; Chernyak, N.; Mader, C. C.; Nallagatla, S.; Kang, R. S.; Hao, L.; Walker, D. A.; Halo, T. L.; Merkel, T. J.; Rische, C. H.; et al. Immunomodulatory Spherical Nucleic Acids. *Proc. Natl. Acad. Sci. U. S. A.* **2015**, *112* (13), 3892–3897.

(41) Zhang, P.; Chiu, Y.-C.; Tostanoski, L. H.; Jewell, C. M. Polyelectrolyte Multilayers Assembled Entirely from Immune Signals on Gold Nanoparticle Templates Promote Antigen-Specific T Cell Response. *ACS Nano* **2015**, *9* (6), 6465–6477.

(42) Ainai, A.; Hasegawa, H.; Obuchi, M.; Odagiri, T.; Ujike, M.; Shirakura, M.;

Nobusawa, E.; Tashiro, M.; Asanuma, H. Host Adaptation and the Alteration of Viral Properties of the First Influenza A/H1N1pdm09 Virus Isolated in Japan. *PLoS One* **2015**, *10* (6), e0130208.

(43) Vigderman, L.; Manna, P.; Zubarev, E. R. Quantitative Replacement of Cetyl Trimethylammonium Bromide by Cationic Thiol Ligands on the Surface of Gold Nanorods and Their Extremely Large Uptake by Cancer Cells. *Angew. Chemie - Int. Ed.* **2012**, *51* (3), 636–641.

(44) Sau, T. K.; Murphy, C. J. Room Temperature, High-Yield Synthesis of Multiple Shapes of Gold Nanoparticles in Aqueous Solution. *J. Am. Chem. Soc.* **2004**, *126* (28), 8648–8649.

(45) Gole, A.; Murphy, C. J. Seed-Mediated Synthesis of Gold Nanorods : Role of the Size and Nature of the Seed Seed-Mediated Synthesis of Gold Nanorods : Role of the Size and Nature of the Seed. *Chem. Mater.* **2004**, *16* (21), 3633–3640.

(46) Liu, X.; Atwater, M.; Wang, J.; Huo, Q. Extinction Coefficient of Gold Nanoparticles with Different Sizes and Different Capping Ligands. *Colloids Surfaces B Biointerfaces* **2007**, *58* (1), 3–7.

(47) Orendorff, C. J.; Murphy, C. J. Quantitation of Metal Content in the Silver-Assisted Growth of Gold Nanorods. *J. Phys. Chem. B* **2006**, *110* (9), 3990–3994.

(48) Hirabayashi, Y.; Kurata, H.; Funato, H.; Nagamine, T.; Aizawa, C.; Tamura, S. ichi; Shimada, K.; Kurata, T. Comparison of Intranasal Inoculation of Influenza HA Vaccine Combined with Cholera Toxin B Subunit with Oral or Parenteral Vaccination. *Vaccine* **1990**, *8* (3), 243–248.

(49) Ikeda, K.; Ainai, A.; Hasegawa, H. Protective Antibody Responses against A(H1N1)Pdm09 Primed by Infection and Recalled by Intranasal Vaccination. *Vaccine* **2015**, *33* (45), 6066–6069.

(50) Asahi, Y.; Yoshikawa, T.; Watanabe, I.; Iwasaki, T.; Hasegawa, H.; Sato, Y.;

Shimada, S.; Nanno, M.; Matsuoka, Y.; Ohwaki, M.; et al. Protection Against Influenza Virus Infection in Polymeric Ig Receptor Knockout Mice Immunized Intranasally with Adjuvant-Combined Vaccines. *J. Immunol.* **2002**, *168* (6), 2930–2938.

(51) Stevens, J.; Corper, A. L.; Basler, C. F.; Taubenberger, J. K.; Palese, P.; Wilson, I. A. Structure of the Uncleaved Human H1 Hemagglutinin from the Extinct 1918 Influenza Virus. *Science* **2004**, *303* (5665), 1866–1870.

(52) Tobita, K.; Sugiura, A.; Enomote, C.; Furuyama, M. Plaque Assay and Primary Isolation of Influenza A Viruses in an Established Line of Canine Kidney Cells (MDCK) in the Presence of Trypsin. *Med. Microbiol. Immunol.* **1975**, *162* (1), 9–14.

(53) Lutz, M. B.; Kukutsch, N.; Ogilvie, A. L. .; Rößner, S.; Koch, F.; Romani, N.; Schuler, G. An Advanced Culture Method for Generating Large Quantities of Highly Pure Dendritic Cells from Mouse Bone Marrow. *J. Immunol. Methods* **1999**, *223* (1), 77–92.

(54) Sau, T. K.; Murphy, C. J. Seeded High Yield Synthesis of Short Au Nanorods in Aqueous Solution. *Langmuir* **2004**, *20* (15), 6414–6420.

(55) Limmon, G. V; Arredouani, M.; McCann, K. L.; Corn Minor, R. a; Kobzik, L.; Imani, F. Scavenger Receptor Class-A Is a Novel Cell Surface Receptor for Double-Stranded RNA. *FASEB J.* **2008**, *22* (1), 159–167.

(56) Watanabe, A.; Tatematsu, M.; Saeki, K.; Shibata, S.; Shime, H.; Yoshimura, A.; Obuse, C.; Seya, T.; Matsumoto, M. Raftlin Is Involved in the Nucleocapture Complex to Induce Poly(I:C)-Mediated TLR3 Activation. *J. Biol. Chem.* **2011**, *286* (12), 10702–10711.

(57) Nellimarla, S.; Baid, K.; Loo, Y.-M.; Gale, M.; Bowdish, D. M. E.; Mossman, K. L. Class A Scavenger Receptor-Mediated Double-Stranded RNA Internalization Is

Independent of Innate Antiviral Signaling and Does Not Require Phosphatidylinositol 3-Kinase Activity. *J. Immunol.* **2015**, *195* (8), 3858–3865.

(58) Aggarwal, B. B. Signalling Pathways of the TNF Superfamily: A Double-Edged Sword. *Nat. Rev. Immunol.* **2003**, *3* (9), 745–756.

(59) Bradley, J. TNF-Mediated Inflammatory Disease. *J. Pathol.* **2008**, *214* (2), 149–160.

(60) Satie, A.; Mazaud-Guittot, S.; Seif, I.; Mahé, D.; He, Z.; Jouve, G.; Jégou, B.; Dejucq-Rainsford, N. Excess Type I Interferon Signaling in the Mouse Seminiferous Tubules Leads to Germ Cell Loss and Sterility. *J. Biol. Chem.* **2011**, *286* (26), 23280–23295.

(61) Matsumoto, M.; Tatematsu, M.; Nishikawa, F.; Azuma, M.; Ishii, N.; Morii-Sakai, A.; Shime, H.; Seya, T. Defined TLR3-Specific Adjuvant That Induces NK and CTL Activation without Significant Cytokine Production in Vivo. *Nat. Commun.* **2015**, *6*, 6280.

(62) Sims, J. E.; Smith, D. E. The IL-1 Family: Regulators of Immunity. *Nat. Rev. Immunol.* **2010**, *10* (2), 89–102.

(63) Ji, Z.; Wang, X.; Zhang, H.; Lin, S.; Meng, H.; Sun, B.; George, S.; Xia, T.; Nel, A. E.; Zink, J. I. Designed Synthesis of CeO2 Nanorods and Nanowires for Studying Toxicological Effects of High Aspect Ratio Nanomaterials. *ACS Nano* **2012**, *6* (6), 5366–5380.

(64) Sun, B.; Ji, Z.; Liao, Y. P.; Wang, M.; Wang, X.; Dong, J.; Chang, C. H.; Li, R.; Zhang, H.; Nel, A. E.; et al. Engineering an Effective Immune Adjuvant by Designed Control of Shape and Crystallinity of Aluminum Oxyhydroxide Nanoparticles. *ACS Nano* **2013**, *7* (12), 10834–10849.

(65) Kusaka, T.; Nakayama, M.; Nakamura, K.; Ishimiya, M.; Furusawa, E.; Ogasawara, K. Effect of Silica Particle Size on Macrophage Inflammatory

Responses. *PLoS One* **2014**, *9* (3), e92634.

Chapter 3

Immobilization of influenza hemagglutinin onto gold nanoparticles with controlled orientation

3-1 Introduction

Inorganic nanoparticles are good candidate as scaffold of biomolecules such as peptides, protein and nucleic acids for drug delivery and biosensors.[1–6] Proteins have not only chemical composition-derived physicochemical properties, but also unique biological functions originated from three-dimensional structure. These biological functions are easily lost by denaturation due to interaction with nanoparticles depending their physicochemical properties when proteins are immobilized onto nanoparticles.[7–10] Therefore, it is necessary to control the size, shape and chemical properties of the nanoparticles to prevent protein denaturation and utilize the specific function of proteins.[11] For example, nanoparticle size influences the mode of protein adsorption (Figure 3-1A).[12] Globular protein such as bovine serum albumin tends to be denatured when adsorbed on larger size particles which have lower surface curvature. In contrast, bovine fibrinogen, rod-like protein, is denatured on small nanoparticles which have higher surface curvatures by wrapping around surface. These effects are also influenced by nanoparticle surface chemical properties and hydrophobic surface induces more denaturation of each protein. V. M. Rotello et al. reported binding of α-chymotrypsin (ChT) onto anionic functionalized nanoparticles through electrostatic interaction between anionic surface and cationic site around the ChT active site. The active site was concealed by immobilization onto the AuNPs, and the enzymatic activity of ChT was blocked. At this time, oligoethylene glycol (OEG) domain of self-assembled monolayer on AuNPs surface suppressed denaturation of ChT (Figure 3-1B).[13] As shown in these researches, when proteins are immobilized onto nanoparticles, it is necessary to control interaction between the proteins and nanoparticles to retain and hide specific protein functions.

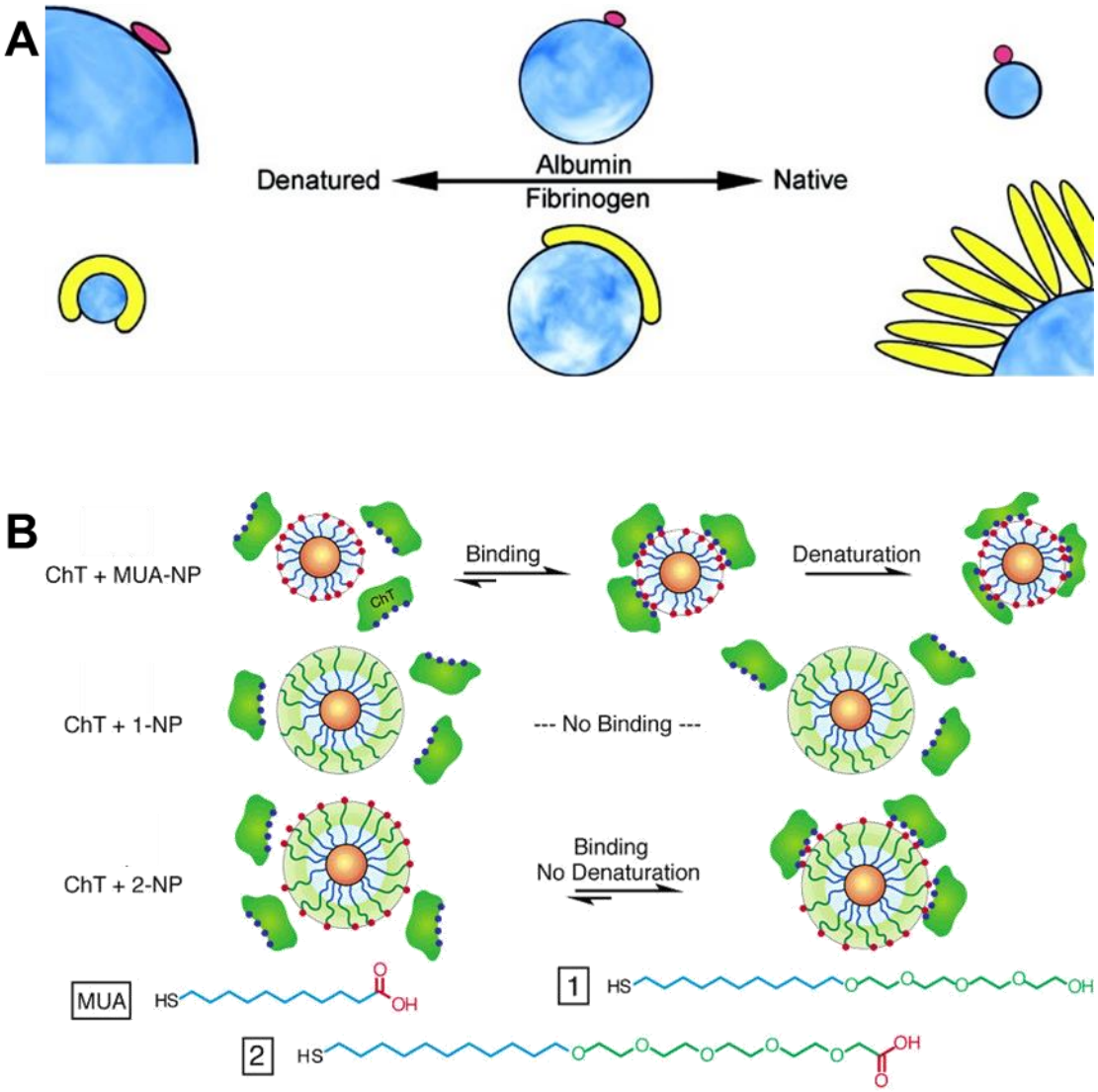

Figure 3-1 The effect of nanoparticle (A) size and (B) surface chemistry on the denaturation of immobilized protein on nanoparticles.[12,13]

The extraction of specific property of protein is important in the development of rational vaccine design, especially against viruses such as influenza viruses, which is subjected frequently mutation. Influenza hemagglutinins (HAs) are composed by head domain and stalk domain and most HA-specific antibodies are target the head domain, which locates outer of whole virus. Influenza virus avoid host immunity by subjecting frequent point mutations in head domain,[14,15] which cause antigenic drift and thereby annual update of influenza vaccines has been required. On the contrast, stalk domain is relatively conserved among heterosubtypic influenza viruses.[16,17]

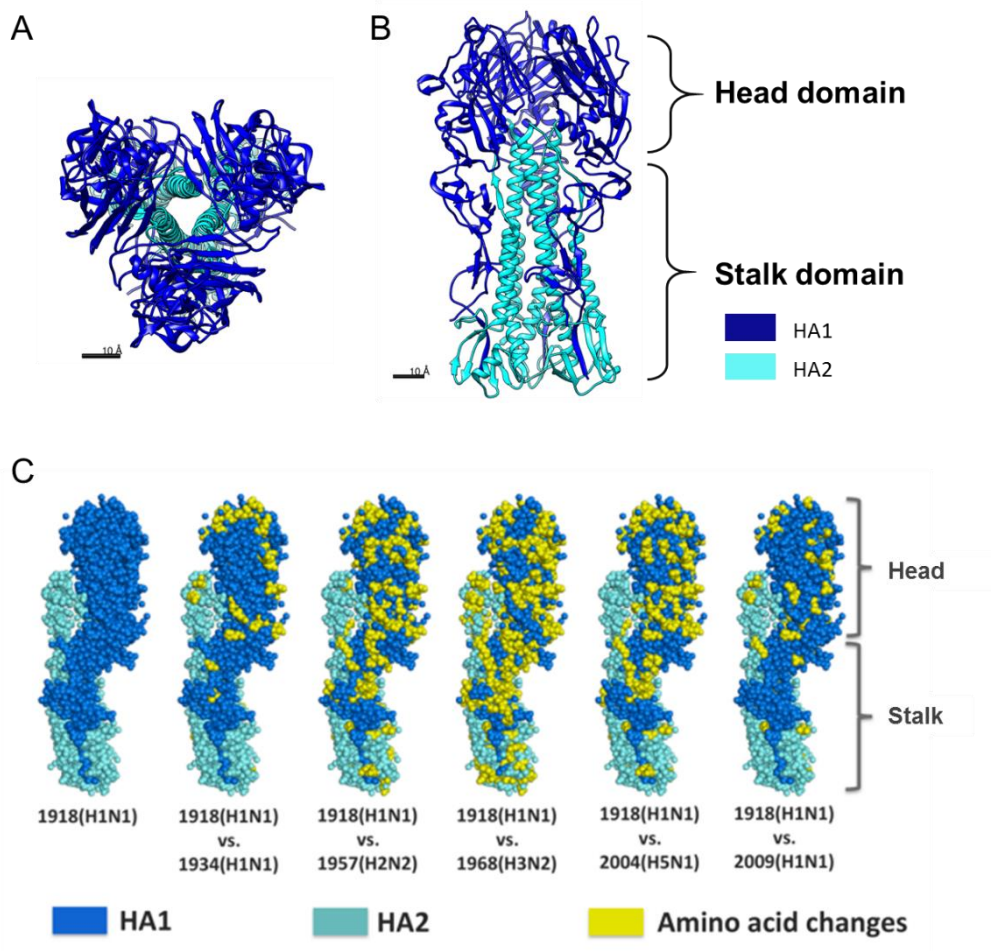

Figure 3-2 Structure of influenza hemagglutinin trimer. (A) Top view and (B) side view. (C) structure of hemagglutinin monomer with amino acid changes between HA shown yellow.[29]

Hence, it has been considered that antibodies against conserved epitope in stalk domain can broadly neutralize multiple influenza virus strains. Indeed, C179 antibody, which recognizes HA stalk domain neutralizes the H1, H2, H5, H6 and H9 subtypes.[18,19] To date, various broadly neutralizing antibodies have been discovered. These broadly neutralize stalk antibody protect against influenza virus by blocking the cleavage of HA to HA1 and HA2 in acidic condition or preventing the emerging of new virions from the infected cells.[20–24] To induce broadly neutralizing anti influenza-antibody by vaccination, various immunogen design has been conducted (Figure 3-2). The currently reported design of antigen to elicit antibodies against the HA stalk region are head-stalk chimeric HA[25–28], headless HA[29–32] and hyperglycosylated HA[33] and rational design of antigen is still under way.

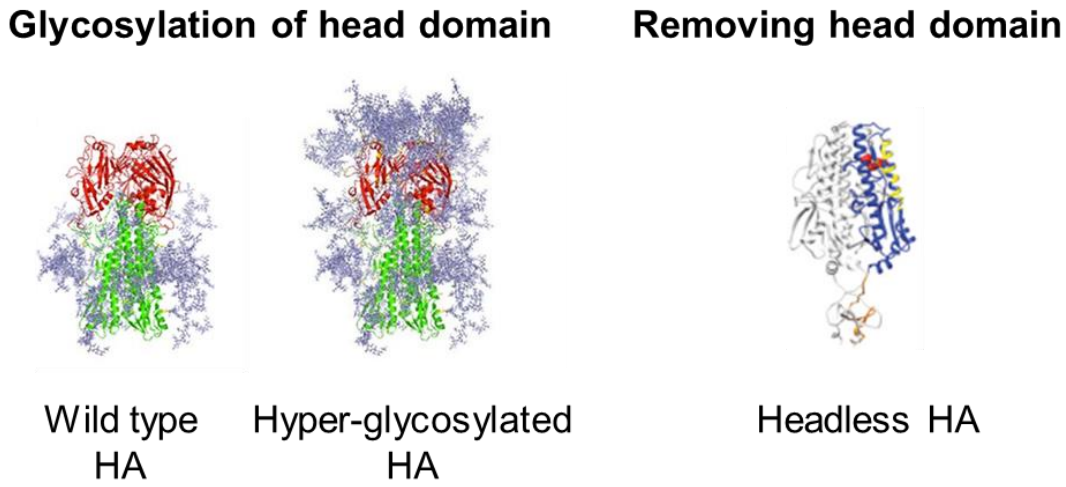

Figure 3-2 Immunogen design for the development of universal influenza vaccine. Hyperglycosylated HA (left)[33] and headless HA (right)[31].

To achieve the development of broadly neutralizing influenza vaccine, nanoparticles can be utilized because nanoparticle-based vaccine can improve immunogenicity[34353637383940] and the receptor signaling by antigen clustering[41] resulting to induce desired immune responses. Here, I utilize molecular recognition of HA, receptor binding site on head domain and histidine tag in stalk domain, to induce specific immune response.

In this chapter, I proposed hemagglutinin immobilized AuNPs that presented the stalk domain toward outside and aimed selectively induction of anti-stalk domain antibody production. Nitrilotriacetic acid (NTA) thiol ligand and sialic acid-mimic (S2) peptide were prepared to functionalize AuNPs. S2 peptide binds receptor binding site of HA head domain[42], so that HA can be immobilized with stem or head domain facing outside. AuNPs were functionalized with NTA-terminated thiol ligands or S2 peptides using the self-assembled monolayer (SAM) technique.[43,44] Cysteine-terminated proline linker forms peptide SAM on AuNPs with well-ordered structure and high surface density. Zwitterionic sequences such as EKEKEKE spacer have a non-fouling nature like OEG (Figure 3-3).[43,44] Therefore, I used SAM forming S2 peptide sequence ARLPRGGGEKEKEKEPPPPC. I prepared S2 peptide-functionalized gold nanoparticles (AuNPs) as scaffolds of HA for the immobilization of HA with controlled orientation. Peptide functionalized AuNPs were incubated with HA (A/Puerto Rico/8/1934 H1N1), then immobilized HA was quantified by dot blot assay and compared to reference sequence and specific immobilization of HA onto the S2 peptide-functionalized AuNPs was evaluated (Figure 3-4).

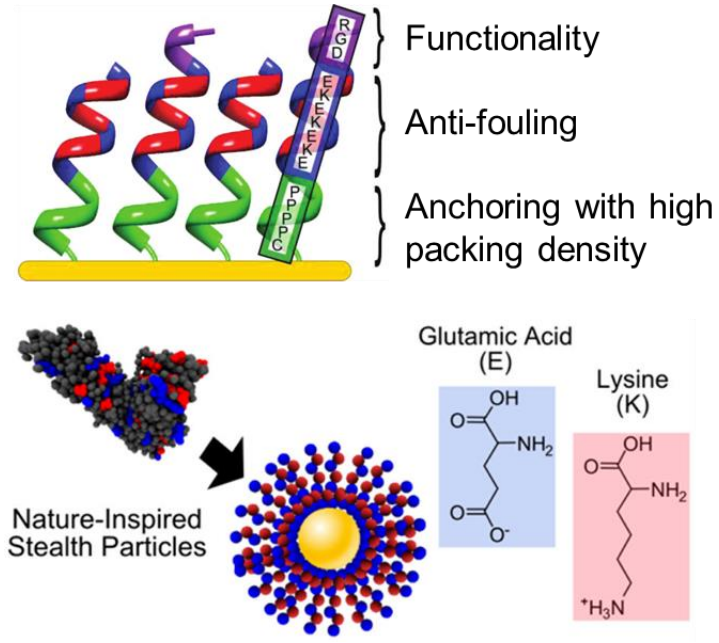

Figure 3-3 Schematic illustration of anti-fouling functional peptides (Top)[43] and application to nanoparticle surface functionalization (bottom)[44].

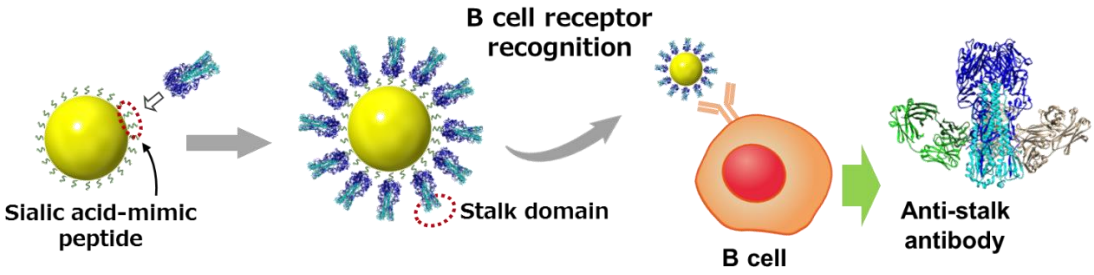

Figure 3-4 Schematic illustration of this research. (left) preparation of HA immobilized AuNPs with controlled orientation. (right) final goal of this research: induction of anti-stalk domain antibody.

3-2 Experimental section

3-2-1 General Information

All commercially available reagents were used without further purification. Peptides were purchased from GenScript Japan. Hydrophilic PVDF membrane was purchased from MERCK (Germany). Phosphate buffered saline tablet was purchased from Takara Bio, Inc. (Japan). Clarity western ECL substrate was purchased from Bio-Rad Laboratories, Inc (USA). Tween20 was purchased from MP Biomedicals, Inc. (Germany). Anti-His-tag mAb-HRP-DirecT antibody was purchased from Medical & Biological Laboratories, Co., Ltd. (Japan). Purified His-tagged HA (A/Puerto Rico/8/34 (H1N1)) were kindly given from Prof. Hasegawa's group at National Institute of Infectious Diseases (NIID). All reaction solvents were purchased from FUJIFILM Wako Pure Chemical Corporation (Japan) and used without further purification. Thin-layer chromatography (TLC) was performed on glass-backed pre-coated silica gel plates (60F254, Merck & Co., Inc., USA). Silica-gel (60N, 40-50 μm) and solvents for column chromatography were purchased from Kanto Chemical (Japan). NMR spectra were recorded on a 400 MHz JEOL spectrometer.

3-2-2 Synthesis of thiol ligands

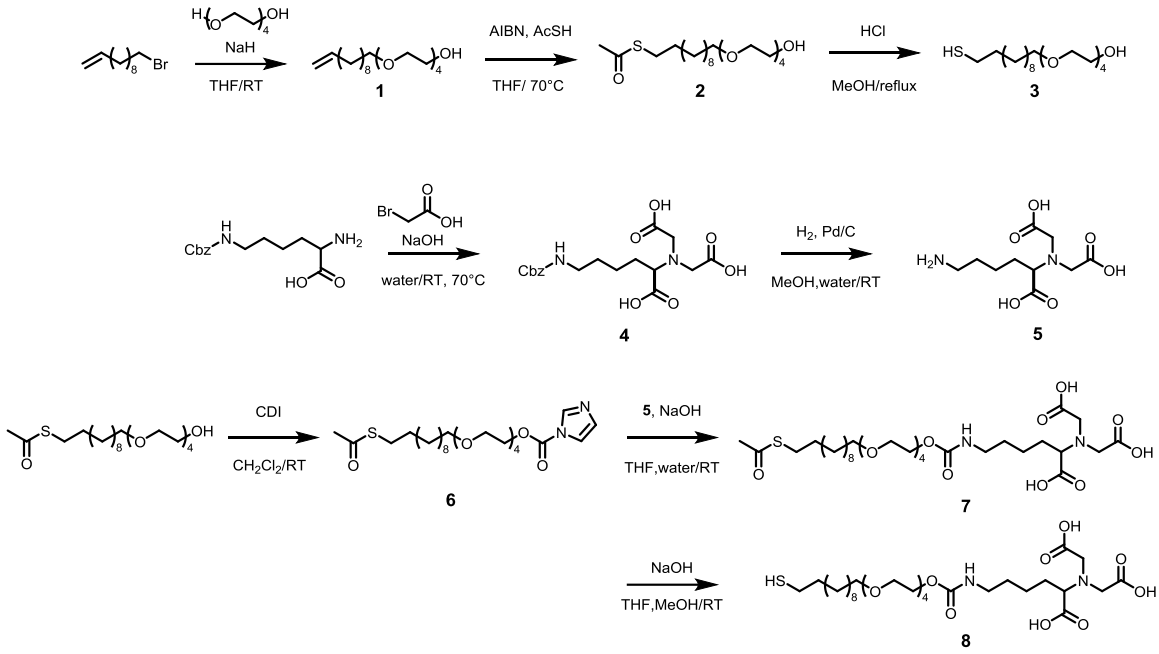

Figure 3-5 Synthetic scheme of 23-mercapto-3,6,9,12-tetraoxatricosan-1-ol (**3**) and 4-carboxy-3-(carboxymethyl)-34-mercapto-10-oxo-11,14,17,20,23-pentaoxa-3,9-diazatetratriacontanoic acid (**8**)

Synthesis of 23-mercapto-3,6,9,12-tetraoxatricosan-1-ol, 3[45]

3,6,9,12-tetraoxatricos-22-en-1-ol, **1**

Tetra(ethylene)glycol (13.3 g, 68 mmol) was dissolved in THF (20 mL). The solution was cooled on ice and added 60% NaH in oil (1.22 g, 30.6 mmol) and 11-bromo-1-undecene (4.0 g, 17 mmol). The solution was allowed warm to room temperature and stirred overnight. The solvent was removed in reduced pressure. The residue was dissolved in brine/ethyl acetate and then the objective was extracted to ethyl acetate 5 times to remove excess substrate.33 The combined organic layer was dried over anhydrous Na_2SO_4. The crude product was concentrated under reduced pressure and purified by flash chromatography on silica gel (EA /Hexane = 2:1 (v/v) to EA/MeOH = 9.5:0.5 (v/v)) to yield compound 9a (2.26 g, 6.5 mmol, 38 %) as a clear oil.

^{1}H NMR (400 MHz, $CDCl_3$): δ/ppm 1.24-1.37 (m, 14H), 1.54-1.59 (m, 2H), 2.01-2.09 (m, 2H), 2.66 (bs, 1H), 3.45 (t, 2H, J=6.8 Hz), 3.57-3.75 (m, 16H), 4.90-5.01 (m, 2H), 5.76-5.86 ppm (m, 1H)

S-(1-hydroxy-3,6,9,12-tetraoxatricosan-23-yl) ethanethioat,e **2**

Compound **1** (2.2 g, 6.35 mmol) was dissolved in THF (10 mL). Then, thioacetic acid (2.2 mL, 32 mmol) and 2,2'-azobisisobutyronitrile (AIBN) (1.04 g, 6.35 mmol) were added to the solution. The mixture was refluxed for 3 h. The solvent was removed under reduced pressure. The residue was purified by flash chromatography on silica gel (EA /Hexane = 3:2 (v/v) to EA/MeOH = 9.5:0.5 (v/v)) to yield 1.96 g (4.63 mmol, 73%) as a light yellow oil.

^{1}H NMR (400 MHz, $CDCl_3$): δ/ppm 1.26 (bs, 14H), 1.52-1.59 (m, 4H), 2.32 (s, 3H), 2.66 (t, 1H, J=6.0 Hz), 2.86 (t, 2H, J=7.3 Hz), 3.45 (t, 2H, 6.8 Hz), 3.57-3.72 (m, 16H)

23-mercapto-3,6,9,12-tetraoxatricosan-1-ol, **3**

Compound **2** (0.69 g, 1.6 mmol) was dissolved in MeOH (2 mL). To this solution, 1 M HCl (3.3 mL) was added. The mixture was refluxed overnight. After solvent was removed under reduced pressure, the residue was dissolved in CH_2Cl_2 and washed with brine. The organic layer was concentrated in reduced pressure. The residue was diluted with ethyl acetate and washed through silica plug (~ 5 mm) to give 500 mg of compound **3** (1.3 mmol, 81%) as a light yellow oil.

^{1}H NMR (400 MHz, $CDCl_3$): δ/ppm 1.23-1.39 (m, 14H), 1.54-1.64 (m, 4H), 2.52 (q, 2H, J=7.3 Hz), 2.65 (bs, 1H), 3.41-3.73 (m, 16H)

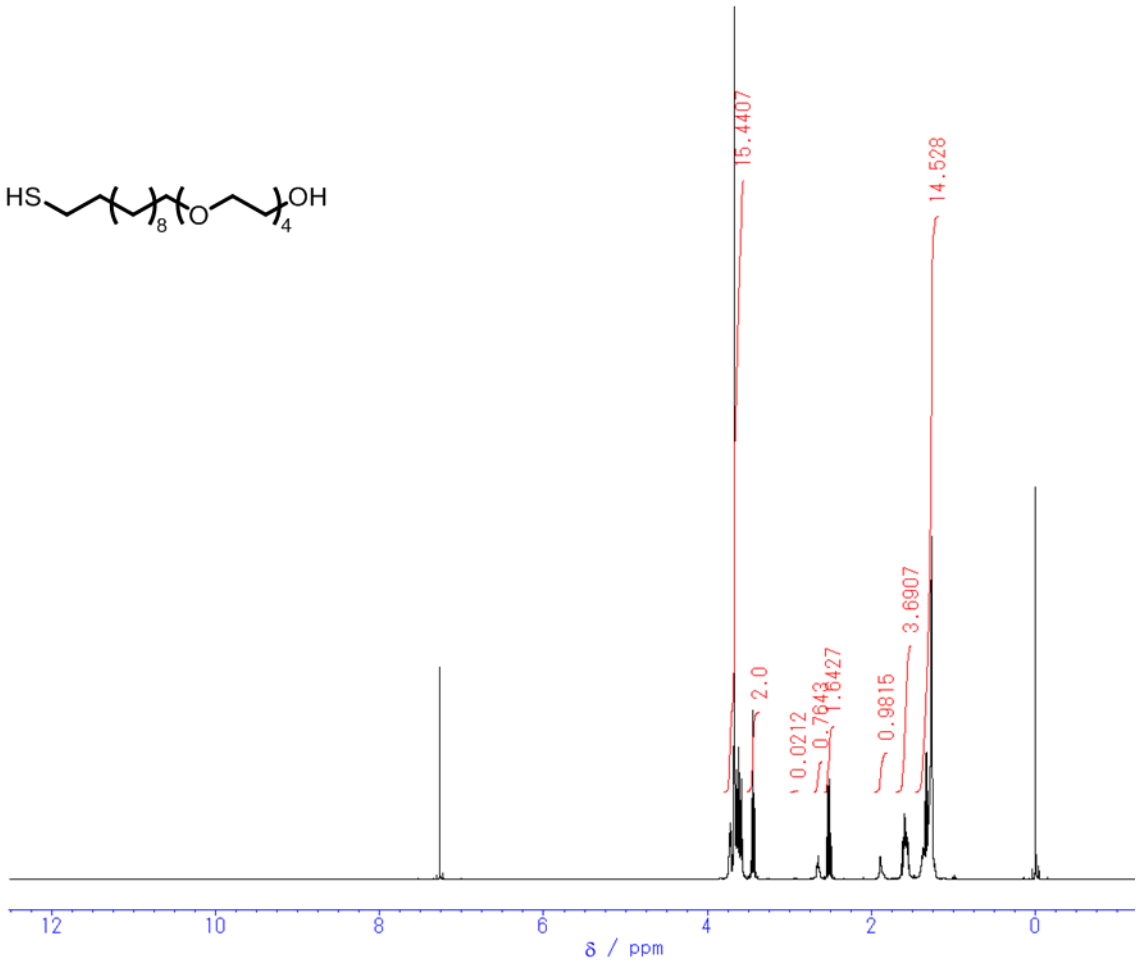

Figure 3-6 ^{1}H NMR spectrum of 23-mercapto-3,6,9,12-tetraoxatricosan-1-ol (**3**).

4-carboxy-3-(carboxymethyl)-34-mercapto-10-oxo-11,14,17,20,23-pentaoxa-3,9-diazatetratriacontanoic acid, **8**[46–48]

(S)-2,2'-((5-(((benzyloxy)carbonyl)amino)-1-carboxypentyl)azanediyl)diacetic acid, **4**

N_6-((benzyloxy)carbonyl)-L-lysine (8.57 g, 30.6 mmol) was dissolved in 45 mL of 2 M NaOH, and the solution was added dropwise with stirring to an ice-cooled solution of 8.50 g (61.2 mmol) of bromoacetic acid in 30 mL of 2 N NaOH. The solution was stirred overnight at room temperature, and then heated for 2 h at 70°C. After cooling the solution to room temperature, 90 mL of 1 M HCl was added. The precipitated was collected by filtration under reduced pressure. The crude product was dissolved in 100 mL of 1 M NaOH and precipitated by addition of 100 mL of 1 M HCl. The precipitate was collected to yield 9.46 g of compound 4 (23.9 mmol, 78%) as white powder.

^{1}H NMR (400 MHz, DMSO-d_6): δ/ppm 1.26-1.69 (m, 6H), 2.94-2.99 (m, 2H), 3.31-3.55 (m, 5H), 5.00 (s, 2H), 7.21-7.38 (m, 5H)

(S)-2,2'-((5-amino-1-carboxypentyl)azanediyl)diacetic acid, **5**

The compound **4** (3.4 g, 8.6 mmol) was dissolved in MeOH/water (95 mL/5 mL). Pd/C (0.17 g) was added to the solution and then the solution was stirred under H_2 for 5 h at room temperature. The Pd/C was filtered off by reduced pressure and rinsed with water sufficiently. The solvent was removed under reduced pressure. The residue was triturated by pentane. The product was dissolved in water, and then recrystallized with ethanol in freezer. The crystal was collected by filtration under reduced pressure and washed by ice-cold water/ethanol (1:1) solution and dried to yield 2.07 g of compound **5** (7.89 mmol, 92%) as white powder.

^{1}H NMR (400 MHz, D_2O): δ/ppm 1.42-1.58 (m, 4H), 1.73-1.81 (m, 2H), 2.85 (t, 2H, J=7 Hz), 3.74-3.83 (m, 5H)

25-oxo-3,6,9,12-tetraoxa-24-thiahexacosyl 1H-imidazole-1-carboxylate, **6**

The compound **2** (0.90 g, 2.1 mmol) was dissolved in 8 mL of CH_2Cl_2. To the solution, 1,1'-carbonyl diimidazole was added and the solution was stirred for 2 h at room temperature. After the solvent was removed under reduced pressure, the residue was purified by flash chromatography on silica gel (ethyl acetate) to yield 1.01 g of compound **6** (1.95 mmol, 93%) as clear oil.

^{1}H NMR (400 MHz, CD_3OD): δ/ppm 1.27 (bs, 14H), 1.50-1.58 (m, 4H), 2.29 (s, 3H), 2.85 (t, 2H, J=7 Hz), 3.44 (t, 2H, J=7 Hz), 3.53-3.71 (m, 10H), 3.84-3.86 (m, 2H), 4.56-4.59 (m, 2H), 4.84-4.88 (m, 2H), 7.05-7.07 (m, 1H), 7.60-7.6 (m, 1H), 8.31 (s, 1H)

4-carboxy-3-(carboxymethyl)-10,36-dioxo-11,14,17,20,23-pentaoxa-35-thia-3,9diazaheptatriacontanoic acid, **7**

The compound **5** (0.88 g, 3.3 mmol) was dissolved in 10 mL of water, and the pH was adjusted to 10 by the addition of 3 M NaOH (~ 300 μL). The compound **6** (0.57 g, 1.1 mmol) dissolved in 10 mL of THF was added to the solution and the mixture was stirred overnight at room temperature. The reaction was quenched by the addition of 40 mL of water. The aqueous phase was washed with ethyl acetate twice. After the pH was adjusted to 1, the aqueous phase was extracted with ethyl acetate 4 times. The combined organic phases were washed with brine and dried over Na_2SO_4, and the solvent was removed under reduced pressure to yield 0.35 g of compound **7** (0.49 mmol, 45%) as powder.

^{1}H NMR (400MHz, CD_3OD): δ/ppm 1.26-1.80 (m, 24H), 2.30 (s, 3H), 2.86 (t, 2H, J= 7 Hz), 3.10 (m, 2H), 3.43-3.48 (m, 3H), 3.54-3.72 (m, 18H), 4.13-4.19 (m, 2H)

4-carboxy-3-(carboxymethyl)-34-mercapto-10-oxo-11,14,17,20,23-pentaoxa-3,9-diazatetratriacontanoic acid, **8**

The compound **7** (0.34 g, 0.47 mmol) was dissolved THF/MeOH (1:1). To this solution, 0.39 mL of 12 M NaOH was added and then stirred 4 h at room temperature. The pH of solution was adjusted to 1~2 by the addition of 6 N HCl (~ 2 mL). CH_2Cl_2 and brine was added and then objective was extracted to organic layer and dried over Na_2SO_4. The solvent was removed in reduced pressure to yield 297 mg of compound **8** (0.44 mmol, 94%) as white powder.

^{1}H NMR (400 MHz, DMSO-d_6): δ/ppm 1.23 (m, 18H), 1.44-1.61 (m, 4H), 2.19-2.23 (m, 1H), 2.42 (q, 2H, J = 7 Hz), 2.91 (q, 2H, J = 6.5 Hz), 3.30 (m, 4H), 3.35 (m, 18H) 4.1 (t, 2H, J = 5 Hz), 7.17 (t, 1H, J = 5.6 Hz), 12.41 (bs, 3H)

ESI-MS: $C_{30}H_{55}N_2O_{12}S$ $[M-H]^-$ calced for 667.348, found 667.34903.

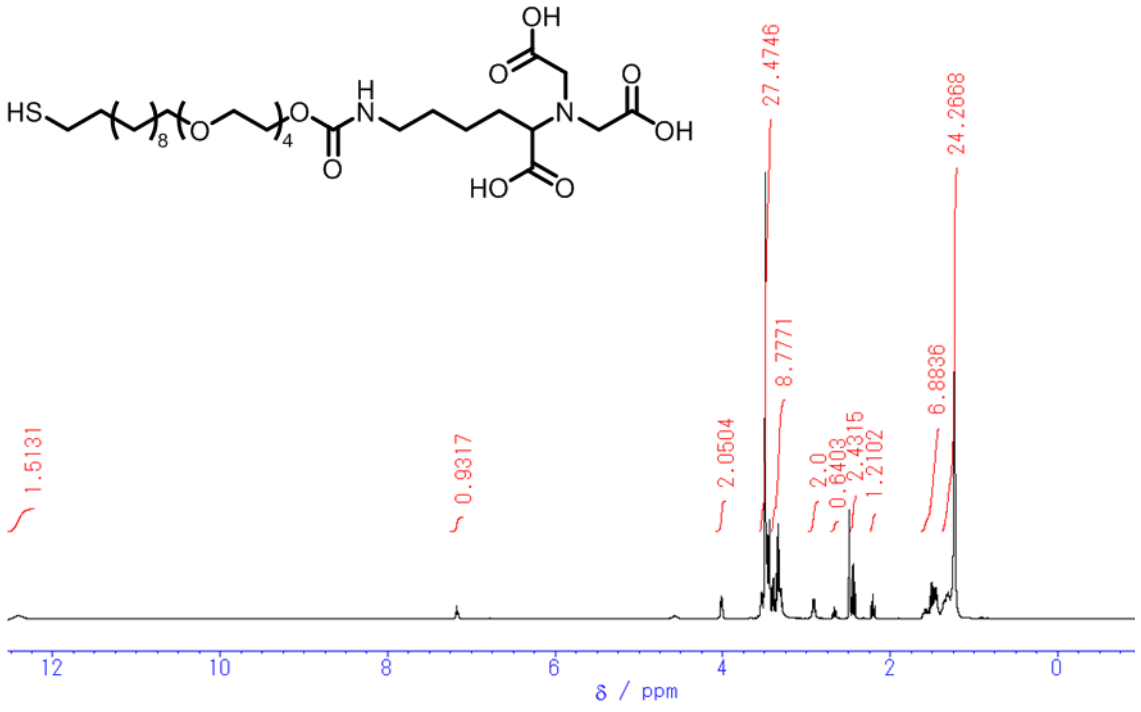

Figure 3-7 ^{1}H NMR spectrum of 4-carboxy-3-(carboxymethyl)-34-mercapto-10-oxo -11,14,17,20,23-pentaoxa-3,9-diazatetratriacontanoic acid (**8**).

3-2-3 Synthesis and surface functionalization of gold nanoparticles

3-2-3-1 synthesis of various sized citrate-capped gold nanoparticles

Citrate-capped gold nanoparticles (AuNPs) were synthesized *via* seeding growth method according to a literature.[49] Brief synthetic scheme was shown in Figure 3-8

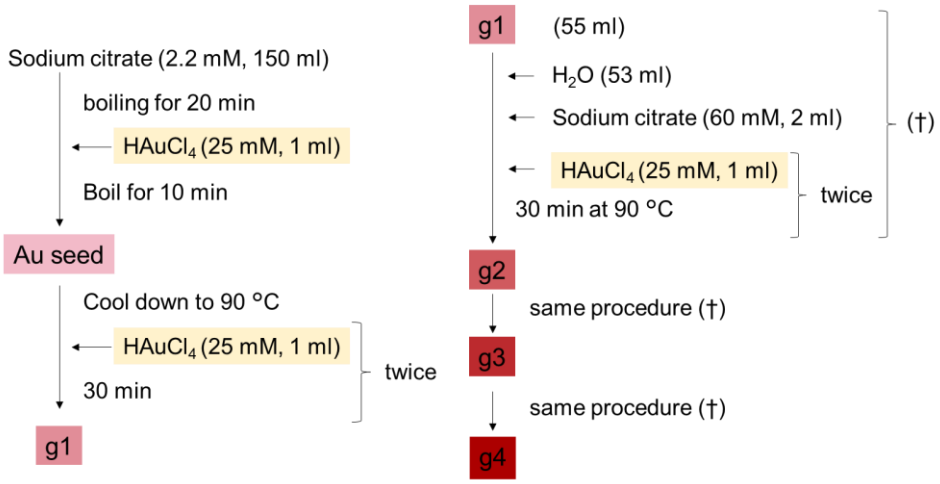

Figure 3-8 Experimental scheme of citrate-capped AuNPs.

For the preparation of Au seed, a solution of 2.2 mM tri-sodium citrate in water (150 mL) was heated with a heating mantle in a 200 mL three-necked flask for 15 min. After boiling, 25 mM $HAuCl_4$ $3H_2O$ (1 mL) was injected. The resulting solution was stirred for 10 min, until the color of solution changed to red.

Immediately after the synthesis of the Au seeds, in the same reaction vessel, the reaction was cooled until the temperature of the solution reached 90°C. Then, 25 mM $HAuCl_4$ solution (1 mL) was injected. After 30 min, the reaction was finished. This process was repeated once again. Obtained gold nanoparticles by this process was defined as g1. The solution g1 (55 mL) was diluted by water (53 mL) and 60 mM tri-sodium citrate (2 mL). The diluted g1 solution was grown by similar method of twice injection of 25 mM $HAuCl_4$ solution at 90°C. Different sized AuNPs: g2, g3 and g4 were prepared sequentially by same growth procedure.

Extinction coefficient of AuNPs was calculated according to a literature[50] and the

concentration of AuNPs was calculated.

3-2-3-2 Surface functionalization of gold nanoparticles

The stock solution of g1 was centrifugated (2,600 g, 10 min) twice and concentrated to 10-fold. To the solution, peptide solutions (1 mM at final concentration) were added and incubated at 40°C for 24 hours. The solution was diluted 10 times with MilliQ water and centrifugated (2,600 g, 10min). The precipitation was re-dispersed in 10 mM HEPES-KOH (pH: 7.4). Excess peptides were removed by centrifugation two more times and AuNPs were concentrated. Peptides sequences were shown in Table 3-2.

Table 3-1 The sequence of peptides used in this research.

	peptides
Spacer sequence (EK)	EKEKEKEPPPPC
Sialic acid mimic sequence (S2EK)	ARLPRGGGEKEKEKEPPPPC
Reference sequence (R5GEK)	ARLPGGGGEKEKEKEPPPPC

3-2-4 Evaluation of hemagglutinin immobilization onto AuNPs

Peptides functionalized AuNPs (2 or 4 nM) were incubated with 20 μg/mL of hemagglutinin in 10 mM HEPES-KOH at room temperature for 30min. Then, the AuNPs were precipitated by centrifugation and supernatants were collected. The concentration of hemagglutinin in supernatant was determined by dot blot assay.

Dilution series of hemagglutinin as standards and obtained supernatants (2 μL) were dropped to hydrophilic PVDF membrane and dried. Membrane were shaken in 5% skim milk in PBS-T (0.1 % Tween20 in PBS(-)) for 60 min at room temperature and then washed with PBS-T for 5 min twice. Anti-His-tag mAb-HRP-DirecT stock solution was diluted 5,000 times with 1% skim milk in PBS-T. Then the membrane was incubated with antibody solution in shield plastic bag for 60 min at room temperature. After incubation, membrane was washed with PBS-T for 5 min twice. The membrane was soaked with substrate solution (Clarity Western ECL substrate; Bio-Rad, mixture of peroxide and luminol) and then chemical luminescence was analyzed using ChemiDoc MP system (Bio-Rad). The number of immobilized hemagglutinin onto the AuNPs was calculated from the HA concentration of supernatant.

3-3 Results and Discussion

3-3-1 Characterization of AuNPs

3-3-1-2 citrate-capped AuNPs

Synthesized g1, g2, g3 and g4 were characterized by transmission electron microscopy (TEM) and UV-vis spectroscopy. TEM images and extinction spectra were shown as Figure 3-9. Average diameters were obtained from TEM images by counting at least 100 particles (Table 3-1). The sizes of g1, g2, g3 and g4 were 25.4, 33.0, 44.0 and 56.9, respectively. Increase of gold nanoparticle size and extinction spectrum peak shift were observed by increase of seeded growth processes.

Here, to evaluate the effect of orientation of immobilized HA, it is desirable to use 10-30 nm in diameter, which are immunologically inert and easy to handle.[35,40] Further, nanoparticles which have 20-40 nm in diameter penetrates tissue barrier and traffic to draining lymph nodes rapidly than larger nanoparticles.[51] Therefore, g1 AuNPs was used for following immobilization of HA, which facilitate to suppress undesired immune response for the evaluation of the effect of HA orientation on antibody responses.

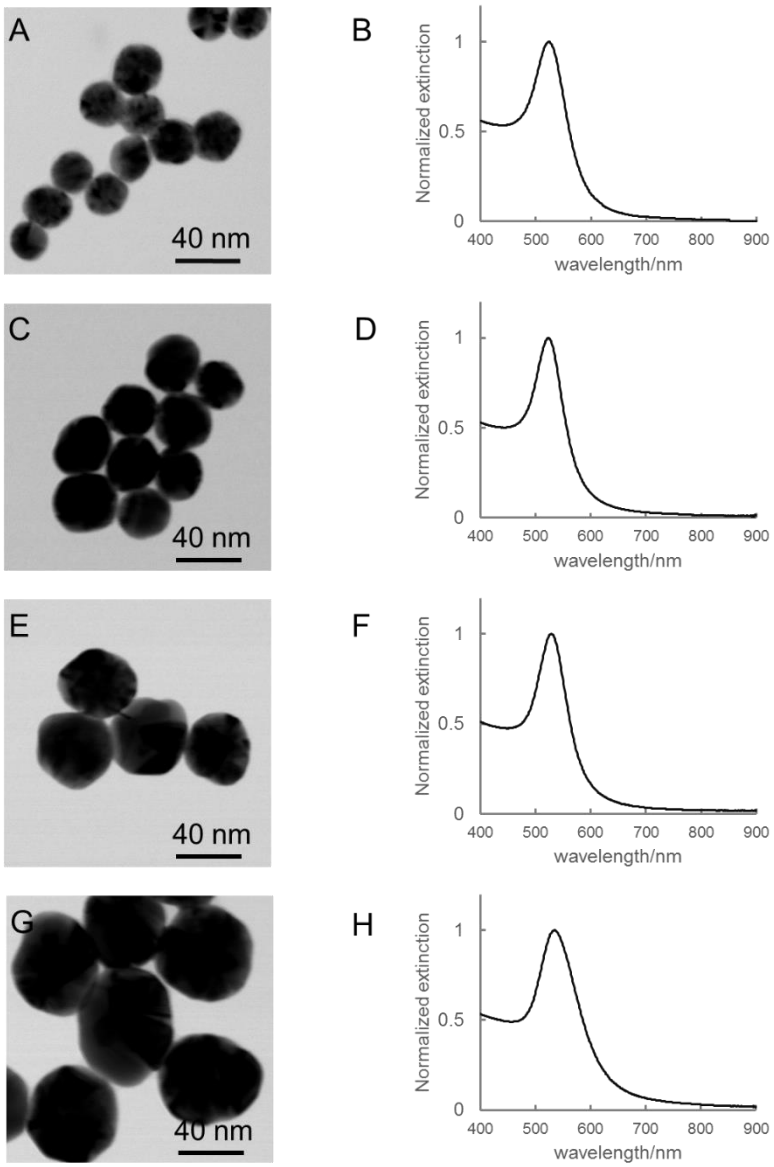

Figure 3-9 TEM images and extinction spectra of citrate-protected AuNP synthesized *via* seeded growth method. (A, B) g1, (C, D) g2, (E, F) g3 and (G, H) g4.

Table 3-2 Size of AuNPs obtained from TEM images

sample	Diameter [nm]
g1	25.4 (±2.3)
g2	33.0 (±3.6)
g3	44.0 (±3.8)
g4	56.9 (±6.2)

3-3-2-1 Peptide-functionalized AuNPs

The AuNPs were functionalized with mixed peptides (100% EK, 10% S2EK + 90% EK and 10% R5GEK + 90% EK). Each sample was named EK-AuNP S2EK-AuNP and R5GEK-AuNP, respectively. The peptide functionalized AuNPs were colloidally stabilized at higher pH (8.0-10.0) and destabilized at lower pH (6.0) in the purification process. The zeta potential of EK peptide functionalized g1 AuNPs were decreased from -30.8 mV to -47.4 mV as pH was increased from 7.4 to 10.0 (data not shown). It was implied that the increase of electric charge caused by deprotonation of the acid in EK moiety contributed the increased colloidal dispersibility.

The TEM images and extinction spectra of peptide-functionalized AuNPs were shown in Figure 3-10A, B. The average diameter of S2EK- and R5GEK-functionalized AuNPs was 25.2 nm and 26.2 nm, respectively. From these result, the core diameter of peptide functionalized AuNPs were not significantly changed through peptide functionalization and purification. The peaks of extinction spectra of peptide-functionalized AuNPs were shifted to longer wavelength (Figure 3-10C). It may be caused by the change of the dielectric constant due to peptide modification.

The hydrodynamic diameter of S2EK-AuNP and R5GEK-AuNP was 40.2 nm and 40.0 nm, respectively. These hydrodynamic diameter of peptide functionalized AuNPs was larger than citrate-capped AuNPs (31.1 nm). The zeta potential of S2EK- and R5GEK-AuNP was increased from -40.8 mV (citrate-capped g1) to -24.0 and -24.8 mV, respectively. These zeta potential values are reflected by the chemical properties of the EK peptide. These changes of hydrodynamic diameter and zeta potential indicated the successive peptide functionalization of AuNPs. As shown in above results, S2EK-AuNPs and R5GEK-AuNPs as a reference were prepared with similar chemical composition, size, colloidal dispersibility and zeta potential.

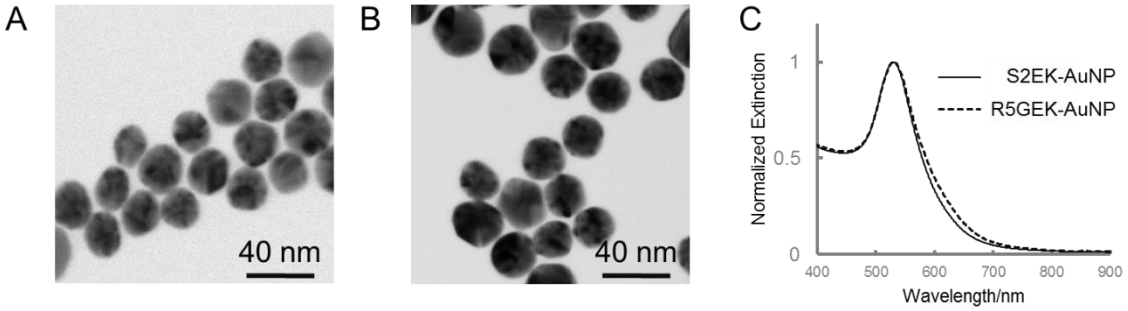

Figure 3-10 TEM images of (A) S2EK-AuNP and (B) R5GEK-AuNP and (C) Extinction spectra.

Table 3-3 the core size of peptide-functionalized AuNPs determined form TEM images.

sample	Diameter [nm]
S2EK-AuNP	25.2 (±3.3)
R5GEK-AuNP	26.2 (±3.0)

Table 3-4 The hydrodynamic diameter and zeta potential of peptide-functionalized AuNPs.

sample	Hydrodynamic diameter [nm]	Zeta potential [mV]
Citrate-AuNP	31.1 (±0.1)	-40.8 (±1.8)
EK-AuNP	36.5 (±0.2)	-30.8 (±1.6)
S2EK-AuNP	40.2 (±0.2)	-24.0 (±1.1)
R5GEK-AuNP	40.0 (±0.1)	-24.8 (±0.7)

3-3-2 Immobilization of hemagglutinin onto AuNPs

The representative dot blot image was shown in Figure 3-11A. The chemical luminescence derived from HA in the supernatant was reduced with increasing AuNP concentration and depending peptide sequence. The concentration of HA in supernatant was determined from these dot intensities and the number of immobilized HA on AuNPs was calculated. The number of immobilized HA was shown in Figure 3-11B. The number of hemagglutinin immobilized onto S2EK-AuNP was 11 molecules per particle. On the contrary, the number of immobilized HA was 4 to 7 molecules per R5GEK-AuNP. From these results, peptide sequence depending immobilization of HA onto AuNPs. This implied the immobilization of HA with controlled orientation by specific binding between sialic acid-binding site and S2 peptide.

The structural images of HA were shown as Figure 3-12. Here, regarding that the top view of HA head domain as an equilateral triangle with a side of 7.2 nm (Figure 3-12A, the distance between 144 Lys), the radius of this circumscribing circle is assumed to be 4.2 nm and the area is calculated to be around 54 nm^2. The height of HA is almost 12 nm. Here, I regarded HA as a cylinder of 12 nm in length and 8.4 nm in diameter. When HA bound perpendicularly to the S2EK-AuNPs, the occupied surface area of the AuNP by HA is estimated to 590 nm^2.(54 $nm^2 \times 11$) The core diameter of S2EK-AuNP is 25 nm and the peptide length was calculated to be 2 nm.[43] So that the diameter of AuNP containing the peptide length was 29 nm. The surface area of sphere with 29 nm in diameter is 2600 nm^2. Accordingly, the occupied surface area by HA was almost 23%. Centrally, when HA is horizontally bound to AuNP surface, the occupied area by HA molecules are estimated to 1100 nm^2 (42% of AuNP surface). The density of surface protein of native influenza virus was reported to around 15%,[52] so that the value of occupied surface area by HA (23%) are reasonable.

Next, I estimated the binding strength between the S2 peptide-presenting AuNP and HA.

The number of immobilized HA was not changed (11 molecules) when the concentration of S2EK-AuNPs (2 and 4 nM) and the resulting concentration of unbound HA was changed from 80.6 to 58.2 nM (Table 3-5). Here, I assumed that the immobilization of HA onto S2EK-AuNP was saturated because the immobilized density was close to the surface protein density of native influenza virus and the number of immobilized HA was not changed by decrease of unbound HA in the system. In this case, the binding of HA with AuNP reached equilibrium. Therefore, dissociation constant between HA and S2EK-AuNP was assumed to less than 60 nM. The dissociation constant between S2 peptide (ARLPR) and HA (A/NewCaledonia/20/99 (H1N1)) was 74 μM.[53] This means HA was strongly immobilized onto S2 peptide-functionalized AuNPs than simple binding between S2 peptide and HA. This result showed multivalent effect in HA-binding ability by displaying S2 peptides onto AuNPs.

From these results, the immobilization of HA onto peptide-functionalized AuNPs depending peptide sequence was demonstrated. This implied HA was immobilized *via* interaction between S2 peptide and receptor binding domain of HA.

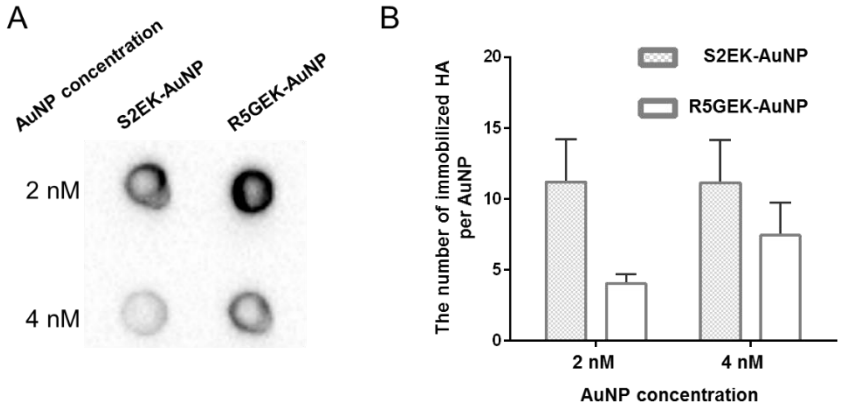

Figure 3-11 (A) The representative dot blot image.
(B) The number immobilized HA on the peptide-functionalized AuNPs (2 and 4 nM).

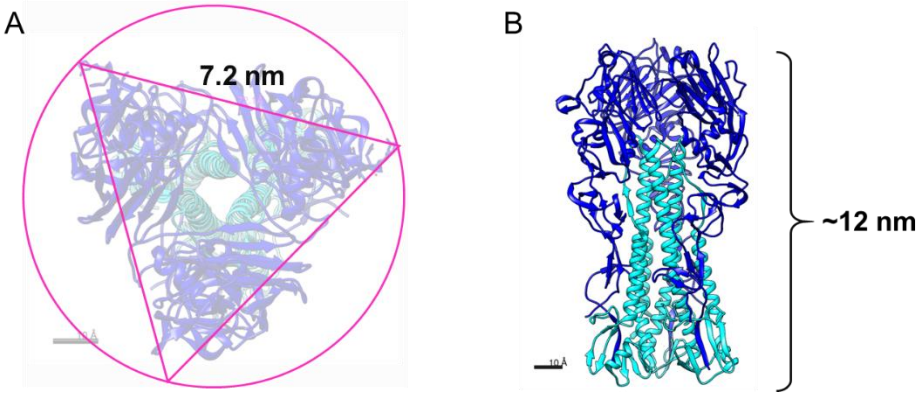

Figure 3-12 The size of influenza HA. (A) Top view and (B) side view of HA. HA1 and HA2 domain was colored with blue and cyan, respectively.

Table 3-5 The number of immobilized HA and the concentration of unbound HA.

S2EK-AuNP [nM]	The number of immobilized HA per AuNP	The concentration of unbound HA [nM]
2	11.3 (±2.9)	80.6 (±5.8)
4	11.2 (±2.9)	58.2 (±11.7)

3-4 Conclusion

In this chapter, I designed surface functionalization with peptides to immobilize HA onto AuNPs with controlled orientation and peptide functionalized AuNPs were used as scaffold of HA. The sialic acid mimic peptide functionalized and reference sequence peptide functionalized AuNPs showed similar physical properties. On the other hand, the number of immobilized HA onto sialic acid mimic peptide functionalized AuNPs was higher than that of reference sequence. This result implied that HA was immobilized with controlled orientation to present stalk domain toward outside by interaction between receptor binding site of HA and sialic acid-mimic peptide. In the future, I will optimize the mixing ration of peptides and improve the immobilization efficiency of HA, then apply for vaccination.

3-5 References

(1) Haes, A. J.; Van Duyne, R. P. A Nanoscale Optical Biosensor: Sensitivity and Selectivity of an Approach Based on the Localized Surface Plasmon Resonance Spectroscopy of Triangular Silver Nanoparticles. *J. Am. Chem. Soc.* **2002**, *124* (35), 10596–10604.

(2) Maxwell, D. J.; Taylor, J. R.; Nie, S. Self-Assembled Nanoparticle Probes for Recognition and Detection of Biomolecules. *J. Am. Chem. Soc.* **2002**, *124* (32), 9606–9612.

(3) Riboh, J. C.; Haes, A. J.; McFarland, A. D.; Yonzon, C. R.; Van Duyne, R. P. A Nanoscale Optical Biosensor: Real-Time Immunoassay in Physiological Buffer Enabled by Improved Nanoparticle Adhesion. *J. Phys. Chem. B* **2003**, *107* (8), 1772–1780.

(4) Liu, J.; Lu, Y. A Colorimetric Lead Biosensor Using DNAzyme-Directed Assembly of Gold Nanoparticles. *J. Am. Chem. Soc.* **2003**, *125* (22), 6642–6643.

(5) El-Sayed, I. H.; Huang, X.; El-Sayed, M. A. Surface Plasmon Resonance Scattering and Absorption of Anti-EGFR Antibody Conjugated Gold Nanoparticles in Cancer Diagnostics: Applications in Oral Cancer. *Nano Lett.* **2005**, *5* (5), 829–834.

(6) Li, D.; Song, S.; Fan, C. Target-Responsive Structural Switching for Nucleic Acid-Based Sensors. *Acc. Chem. Res.* **2010**, *43* (5), 631–641.

(7) You, C. C.; De, M.; Rotello, V. M. Monolayer-Protected Nanoparticle-Protein Interactions. *Curr. Opin. Chem. Biol.* **2005**, *9* (6), 639–646.

(8) Shang, L.; Wang, Y.; Jiang, J.; Dong, S. PH-Dependent Protein Conformational Changes in Albumin:Gold Nanoparticle Bioconjugates: A Spectroscopic Study. *Langmuir* **2007**, *23* (5), 2714–2721.

(9) Mahmoudi, M.; Lynch, I.; Ejtehadi, M. R.; Monopoli, M. P.; Bombelli, F. B.;

Laurent, S. Protein-Nanoparticle Interactions: Opportunities and Challenges. *Chem. Rev.* **2011**, *111* (9), 5610–5637.

(10) Treuel, L.; Nienhaus, G. U. Toward a Molecular Understanding of Nanoparticle-Protein Interactions. *Biophys. Rev.* **2012**, *4* (2), 137–147.

(11) Leidner, A.; Bauer, J.; Ebrahimi-khonachah, M.; Takamiya, M.; Strähle, U.; Dickmeis, T.; Rabe, K. S.; Niemeyer, C. M. Oriented Immobilization of a Delicate Glucose-Sensing Protein on Silica Nanoparticles. *Biomaterials* **2019**, *190–191* (October 2018), 76–85.

(12) Roach, P.; Farrar, D.; Perry, C. C. Surface Tailoring for Controlled Protein Adsorption: Effect of Topography at the Nanometer Scale and Chemistry. *J. Am. Chem. Soc.* **2006**, *128* (12), 3939–3945.

(13) Hong, R.; Fischer, N. O.; Verma, A.; Goodman, C. M.; Emrick, T.; Rotello, V. M. Control of Protein Structure and Function through Surface Recognition by Tailored Nanoparticle Scaffolds. *J. Am. Chem. Soc.* **2004**, *126* (3), 739–743.

(14) Corti, D.; Suguitan, A. L.; Pinna, D.; Silacci, C.; Fernandez-Rodriguez, B. M.; Vanzetta, F.; Santos, C.; Luke, C. J.; Torres-Velez, F. J.; Temperton, N. J.; et al. Heterosubtypic Neutralizing Antibodies Are Produced by Individuals Immunized with a Seasonal Influenza Vaccine. *J. Clin. Invest.* **2010**, *120* (5), 1663–1673.

(15) Sui, J.; Sheehan, J.; Hwang, W. C.; Bankston, L. A.; Burchett, S. K.; Huang, C. Y.; Liddington, R. C.; Beigel, J. H.; Marasco, W. A. Wide Prevalence of Heterosubtypic Broadly Neutralizing Human Anti-Influenza a Antibodies. *Clin. Infect. Dis.* **2011**, *52* (8), 1003–1009.

(16) Krystal, M.; Elliott, R. M.; Benz, E. W.; Young, J. F.; Palese, P. Evolution of Influenza A and B Viruses: Conservation of Structural Features in the Hemagglutinin Genes. *Proc. Natl. Acad. Sci.* **1982**, *79* (15), 4800–4804.

(17) Scientific, C.; Unit, C. B.; Wales, N. S.; Both, G. W.; Sleigh, M. J.; Cox, N. J.;

Kendal, a P. Antigenic Drift in Influenza Virus H3 Hemagglutinin from 1968 to 1980: Multiple Evolutionary Pathways and Sequential Amino Acid Changes at Key Antigenic Sites. *J. Virol.* **1983**, *48* (1), 52–60.

(18) Okuno, Y. Y.; Isegawa, Y. Y.; Sasao, F. F.; Ueda, S. S. A Common Neutralizing Epitope Conserved between the Hemagglutinins of Influenza A Virus H1 and H2 Strains. *J Virol* **1993**, *67* (5), 2552–2558.

(19) Dreyfus, C.; Ekiert, D. C.; Wilson, I. A. Structure of a Classical Broadly Neutralizing Stem Antibody in Complex with a Pandemic H2 Influenza Virus Hemagglutinin. *J. Virol.* **2013**, *87* (12), 7149–7154.

(20) Ekiert, D. C.; Bhabha, G.; Elsliger, M.; Friesen, R. H. E.; Jongeneelen, M.; Throsby, M.; Goudsmit, J.; Wilson, I. A. Conserved Influenza Virus Epitope. *Science (80-.).* **2009**, *1857* (April), 246–252.

(21) Sui, J.; Hwang, W. C.; Perez, S.; Wei, G.; Aird, D.; Chen, L. M.; Santelli, E.; Stec, B.; Cadwell, G.; Ali, M.; et al. Structural and Functional Bases for Broad-Spectrum Neutralization of Avian and Human Influenza A Viruses. *Nat. Struct. Mol. Biol.* **2009**, *16* (3), 265–273.

(22) Ekiert, D. C.; Friesen, R. H. E.; Bhabha, G.; Kwaks, T.; Jongeneelen, M.; Yu, W.; Ophorst, C.; Cox, F.; Korse, H. J. W. M.; Brandenburg, B.; et al. A Highly Conserved Neutralizing Epitope on Group 2 Influenza A Viruses. *Science (80-.).* **2011**, *333* (6044), 843–850.

(23) Dreyfus, C.; Laursen, N. S.; Kwaks, T.; Zuijdgeest, D.; Khayat, R.; Ekiert, D. C.; Lee, J. H.; Metlagel, Z.; Bujny, M. V; Jongeneelen, M.; et al. Highly Conserved Protective Epitopes on Influenza B Viruses. *Science (80-.).* **2012**, *337* (6100), 1343–1348.

(24) Chai, N.; Swem, L. R.; Park, S.; Nakamura, G.; Chiang, N.; Estevez, A.; Fong, R.; Kamen, L.; Kho, E.; Reichelt, M.; et al. A Broadly Protective Therapeutic

Antibody against Influenza B Virus with Two Mechanisms of Action. *Nat. Commun.* **2017**, *8*, 1–16.

(25) Margine, I.; Krammer, F.; Hai, R.; Heaton, N. S.; Tan, G. S.; Andrews, S. A.; Runstadler, J. A.; Wilson, P. C.; Albrecht, R. A.; Garcia-Sastre, A.; et al. Hemagglutinin Stalk-Based Universal Vaccine Constructs Protect against Group 2 Influenza A Viruses. *J. Virol.* **2013**, *87* (19), 10435–10446.

(26) Krammer, F.; Pica, N.; Hai, R.; Margine, I.; Palese, P. Chimeric Hemagglutinin Influenza Virus Vaccine Constructs Elicit Broadly Protective Stalk-Specific Antibodies. *J. Virol.* **2013**, *87* (12), 6542–6550.

(27) Krammer, F.; Hai, R.; Yondola, M.; Tan, G. S.; Leyva-Grado, V. H.; Ryder, A. B.; Miller, M. S.; Rose, J. K.; Palese, P.; Garcia-Sastre, A.; et al. Assessment of Influenza Virus Hemagglutinin Stalk-Based Immunity in Ferrets. *J. Virol.* **2014**, *88* (6), 3432–3442.

(28) Krammer, F.; Margine, I.; Hai, R.; Flood, A.; Hirsh, A.; Tsvetnitsky, V.; Chen, D.; Palese, P. H3 Stalk-Based Chimeric Hemagglutinin Influenza Virus Constructs Protect Mice from H7N9 Challenge. *J. Virol.* **2014**, *88* (4), 2340–2343.

(29) Lu, Y.; Welsh, J. P.; Swartz, J. R. Production and Stabilization of the Trimeric Influenza Hemagglutinin Stem Domain for Potentially Broadly Protective Influenza Vaccines. *Proc. Natl. Acad. Sci.* **2014**, *111* (1), 125–130.

(30) Impagliazzo, A.; Milder, F.; Kuipers, H.; Wagner, M. V.; Zhu, X.; Hoffman, R. M. B.; Van Meersbergen, R.; Huizingh, J.; Wanningen, P.; Verspuij, J.; et al. A Stable Trimeric Influenza Hemagglutinin Stem as a Broadly Protective Immunogen. *Science (80-.).* **2015**, *349* (6254), 1301–1306.

(31) Yassine, H. M.; Boyington, J. C.; McTamney, P. M.; Wei, C. J.; Kanekiyo, M.; Kong, W. P.; Gallagher, J. R.; Wang, L.; Zhang, Y.; Joyce, M. G.; et al. Hemagglutinin-Stem Nanoparticles Generate Heterosubtypic Influenza Protection.

Nat. Med. **2015**, *21* (9), 1065–1070.

(32) Krammer, F. The Quest for a Universal Flu Vaccine: Headless HA 2.0. *Cell Host Microbe* **2015**, *18* (4), 395–397.

(33) Eggink, D.; Goff, P. H.; Palese, P. Guiding the Immune Response against Influenza Virus Hemagglutinin toward the Conserved Stalk Domain by Hyperglycosylation of the Globular Head Domain. *J. Virol.* **2014**, *88* (1), 699–704.

(34) Shiosaka, S.; Kiyama, H.; Wanaka, A.; Masaya, T. A New Method for Producing a Specific and High Titre Antibody against Glutamate Using Colloidal Gold as a Carrier. *Brain Res.* **1986**, *382* (2), 399–403.

(35) Mottram, P. L.; Leong, D.; Crimeen-Irwin, B.; Gloster, S.; Xiang, S. D.; Meanger, J.; Ghildyal, R.; Vardaxis, N.; Plebanski, M. Type 1 and 2 Immunity Following Vaccination Is Influenced by Nanoparticle Size: Formulation of a Model Vaccine for Respiratory Syncytial Virus. *Mol. Pharm.* **2007**, *4* (1), 73–84.

(36) Chen, Y.-S.; Hung, Y.-C.; Liau, I.; Huang, G. S. Assessment of the In Vivo Toxicity of Gold Nanoparticles. *Nanoscale Res. Lett.* **2009**, *4* (8), 858–864.

(37) Hutter, E.; Boridy, S.; Labrecque, S.; Lalancette-Hébert, M.; Kriz, J.; Winnik, F. M.; Maysinger, D. Microglial Response to Gold Nanoparticles. *ACS Nano* **2010**, *4* (5), 2595–2606.

(38) Niikura, K.; Matsunaga, T.; Suzuki, T.; Kobayashi, S.; Yamaguchi, H. Gold Nanoparticles as a Vaccine Platform : In Fl Uence of Size and Shape on Immunological Responses in Vitro and in Vivo. *ACS Nano* **2013**, *7* (5), 3926–3938.

(39) Zhang, P.; Chiu, Y.-C.; Tostanoski, L. H.; Jewell, C. M. Polyelectrolyte Multilayers Assembled Entirely from Immune Signals on Gold Nanoparticle Templates Promote Antigen-Specific T Cell Response. *ACS Nano* **2015**, *9* (6), 6465–6477.

(40) Zhou, Q.; Zhang, Y.; Du, J.; Li, Y.; Zhou, Y.; Fu, Q.; Zhang, J.; Wang, X.; Zhan, L. Different-Sized Gold Nanoparticle Activator/Antigen Increases Dendritic Cells Accumulation in Liver-Draining Lymph Nodes and CD8+ T Cell Responses. *ACS Nano* **2016**, *10* (2), 2678–2692.

(41) Thyagarajan, R.; Arunkumar, N.; Song, W. Polyvalent Antigens Stabilize B Cell Antigen Receptor Surface Signaling Microdomains. *J. Immunol.* **2003**, *170* (12), 6099–6106.

(42) Matsubara, T.; Onishi, A.; Saito, T.; Shimada, A.; Inoue, H.; Taki, T.; Nagata, K.; Okahata, Y.; Sato, T. Sialic Acid-Mimic Peptides as Hemagglutinin Inhibitors for Anti-Influenza Therapy. *J. Med. Chem.* **2010**, *53* (11), 4441–4449.

(43) Nowinski, A. K.; Sun, F.; White, A. D.; Keefe, A. J.; Jiang, S. Sequence, Structure, and Function of Peptide Self-Assembled Monolayers. *J. Am. Chem. Soc.* **2012**, *134* (13), 6000–6005.

(44) Nowinski, A. K.; White, A. D.; Keefe, A. J.; Jiang, S. Biologically Inspired Stealth Peptide-Capped Gold Nanoparticles. *Langmuir* **2014**, *30* (7), 1864–1870.

(45) Choi, S. R.; Seo, J. S.; Bohaty, R. F. H.; Poulter, C. D. Regio- and Chemoselective Immobilization of Proteins on Gold Surfaces. *Bioconjug. Chem.* **2014**, *25* (2), 269–275.

(46) Sigal, G. B.; Bamdad, C.; Barberis, A.; Strominger, J.; Whitesides, G. M. A Self-Assembled Monolayer for the Binding and Study of Histidine-Tagged Proteins by Surface Plasmon Resonance. *Anal. Chem.* **1996**, *68* (3), 490–497.

(47) Schmitt, L.; Ludwig, M.; Gaub, H. E.; Tampé, R. A Metal-Chelating Microscopy Tip as a New Toolbox for Single-Molecule Experiments by Atomic Force Microscopy. *Biophys. J.* **2000**, *78* (6), 3275–3285.

(48) Du Roure, O.; Debiemme-Chouvy, C.; Malthête, J.; Silberzan, P. Functionalizing Surfaces with Nickel Ions for the Grafting of Proteins. *Langmuir* **2003**, *19* (10),

4138–4143.

(49) Bastús, N. G.; Comenge, J.; Puntes, V. Kinetically Controlled Seeded Growth Synthesis of Citrate-Stabilized Gold Nanoparticles of up to 200 Nm: Size Focusing versus Ostwald Ripening. *Langmuir* **2011**, *27* (17), 11098–11105.

(50) Liu, X.; Atwater, M.; Wang, J.; Huo, Q. Extinction Coefficient of Gold Nanoparticles with Different Sizes and Different Capping Ligands. *Colloids Surfaces B Biointerfaces* **2007**, *58* (1), 3–7.

(51) Smith, D. M.; Simon, J. K.; Baker, J. R. Applications of Nanotechnology for Immunology. *Nat. Rev. Immunol.* **2013**, *13* (8), 592–605.

(52) Wasilewski, S.; Calder, L. J.; Grant, T.; Rosenthal, P. B. Distribution of Surface Glycoproteins on Influenza A Virus Determined by Electron Cryotomography. *Vaccine* **2012**, *30* (51), 7368–7373.

(53) MATSUBARA, T.; ONISHI, A.; SAITO, T.; YAMAGUCHI, D.; SATO, T. Multivalent Effect in Influenza Hemagglutinin-Binding Activity of Sugar-Mimic Peptide. *KOBUNSHI RONBUNSHU* **2016**, *73* (1), 62–68.

Chapter 4

Conclusion

In this thesis, I focused on nanoparticle geometry and conjugation method toward the development of effective influenza vaccines. I investigated the effect of nanoparticle geometry on the enhancement of adjuvanticity and nanoparticle surface modification on immobilization of antigenic protein. In this chapter, I summarize the thesis and afforded the significance and prospects.

In chapter 2, I prepared uPIC(40:400)-AuNP conjugates (AuNP-PICs) by electrostatic interaction and evaluated their adjuvanticity *in vivo* and inflammatory cytokine response *in vitro*. I found that the adjuvanticity of AuNP-PICs was depended on their geometry and immunization route. When vaccines were administrated subcutaneously, there is no significant differences between AuNP-PIC groups. On the other hand, when vaccines administrated intranasally, adjuvanticity was depended AuNP-PIC geometry, especially, rod-shaped AuNPs enhanced adjuvanticity of uPIC(40:400) than spherical AuNPs. Notably, the cytokine responses were depending AuNP-PIC geometry and rod-shaped AuNPs did not increased inflammatory cytokine responses, which cause side reactions. These results showed that the election of nanoparticle shape as scaffold of nanoparticle-based adjuvant is essential to fabricate effective and safe adjuvants.

In chapter 3, I focused on antigen design to develop the universal influenza vaccine. I designed hemagglutinin (HA) stalk domain-presenting AuNPs utilizing interaction between receptor binding site of HA and sialic acid-mimic (S2) peptide-functionalized AuNPs. The number of immobilized HA onto S2peptide functionalized AuNPs was higher than that of reference sequence peptide-functionalized AuNPs. This result implied that HA was immobilized with controlled orientation to present stalk domain toward outside by interaction between receptor binding site of HA and sialic acid-mimic peptide. In the future, I believe that the nanoparticle based universal influenza vaccine will be developed through optimization of the mixing ration of peptides and improvement the immobilization efficiency of HA.

In this thesis, I designed nanoparticle-based influenza vaccines to develop universal influenza vaccines. Influenza viruses constantly threated host health and life by acquiring diverse mutation. To combat such evolution of viruses, I proposed nanoscale physicochemical design of vaccines and partially demonstrated. I believe that the findings in this thesis will contribute to the development of universal influenza vaccine that can be protect against various virus subtypes without annual updates and realization of a society where everybody can spend more healthy life.

Acknowledgement

The studies presented in this thesis have been conducted under the guide of Prof. Kuniharu Ijiro through the period of Graduate School of Chemical Sciences and Engineering, Hokkaido University, during April 2013 - March 2019. I would like to express my sincerest gratitude for his kind guidance and continuous encouragement throughout these studies.

I gratefully appreciate to Prof Kenichi Niikura (Nippon Institute of Technology), Associate Prof. Hideyuki Mitomo and Assistant Prof. Yusuke Yonamine (Research Institute for Electronic Science, Hokkaido University) for their kind and valuable guidance.

I owe a very important debt to Dr. Tadaki Suzuki, Dr. Akira Ainai, Dr. Hideki Hasegawa, Mr. Koshiro Tabata, Mr. Yuki Ohara, Ms Kaori Sano and Ms Hanako Sekimukai (National Institute of Infectious Diseases) for the vaccination experiment and the earnest discussion, Mr. Tetsuo Nakano (KYOWA HAKKO BIO CO., LTD.) for kindly giving uPIC(40:400) and earnest discussion and Dr. Shintaro Kobayashi, Associate Prof. Yasuko Orba and Prof. Hirofumi Sawa (Hokkaido University Research Center for Zoonosis Control) for the bone marrow-derived dendritic cells preparation and kind guidance, and Associate Professor Takafumi Ninomiya (Department of Anatomy 1, Sapporo Medical University School of Medicine) for the TEM measurement of tissue slice.

I am deeply grateful to Prof. Koichiro Ishimori (Faculty of Science, Hokkaido University), Prof. Kazuyasu Sakaguchi (Faculty of Science, Hokkaido University) and Prof. Manabu Tokeshi (Faculty of Science, Hokkaido University) for valuable guidance and suggestion to summarize this thesis.

I am grateful to Dr. Kenya Kobayashi, Dr. Gouqing Wang, Ms. Chie Takeuchi, Dr. Ryo Iida and Mrs. Naomi Hirai for kind experiment guidance.

I wish to thank Mrs. Aki Okuhara, Dr. Katsuyuki Nambara, Dr. Ryo Iida, Mr. Yu Trii, Mr. Satoru Hamajima, Ms. Mizuki Nihei, Dr. Noriko Ohtake, Mr. Tatsuya Matsunaga and members of Molecular Device Laboratory for their assistance during my school life.

Finally, I express deep appreciation to my friends, family for their hearty encouragement and assistance.

Taiyu Tazaki

March 2019